EPFL

Master thesis

Development of a numerical model to assess the influence of fluid-structure interactions on the dynamic behavior of geomembrane systems in pressure waterways

---

Candidate

Simon Randin

Thesis director

Giovanni De Cesare

Thesis supervisor

Samuel Vorlet

Ecublens, 2023

LCH

Acknowledgements

Many thoughts and emotions catch up with me as I write these lines. I feel I must begin by thanking the PL-LCH for accepting me and providing me with all the material conditions necessary for the success of this project. A special thanks goes to Dr. Giovanni De Cesare, who has placed his trust in me and given this project a valorizing importance. I would also like to thank all the laboratory collaborators who listened to me complain about the difficulties of the project during the often very instructive coffee breaks, and wish them success for the future projects.

A special mention must go to Samuel Vorlet, who helped make my Master's cycle a wonderful experience. From helping me find an internship for the last summer to supervising this project, he played a major role in my final year at EPFL, which I'll treasure for a long time to come. His advice and understanding have been invaluable to me and have largely contributed to bringing this project to a successful conclusion, even when the technical difficulties encountered seemed to darken its horizon.

Finally, my thoughts go out to my family, who had to put up with my mood sometimes following the irregular convergence curves of the modeling software, and to my friends, who brilliantly knew how to take my mind off things when necessary. I hope from the bottom of my heart that this final project at EPFL will be worthy of the attention that all these people have given me.

Ecublens, June 18, 2023

Beaucoup de pensées et d'émotions me rattrapent au moment d'écrire ces quelques lignes. Je crois devoir commencer par remercier le PL-LCH de m'avoir accueilli et d'avoir mis à ma disposition toutes les conditions matérielles nécessaires à la réussite de ce projet. Un merci particulier va ainsi de fait au Dr. Giovanni De Cesare qui a bien voulu me faire confiance et accorder une importance valorisante à ce projet. Je me dois aussi de remercier tous les collaborateurs du laboratoire qui ont bien voulu m'écouter me plaindre des difficultés du projet lors de pauses café souvent très instructives et leur souhaite plein de réussite pour les projets à venir.

Une mention particulière doit être faite à Samuel Vorlet, qui a contribué à faire de mon cycle de master une formidable expérience. De sa contribution à l'obtention d'un stage à l'été dernier jusqu'à l'encadrement de ce projet, il est pour beaucoup dans cette dernière année à l'EPFL que je garderai longtemps dans ma mémoire. Ses conseils et sa compréhension ont été très précieux pour moi et ont largement contribué à mener ce projet à bon port, alors même que les difficultés techniques rencontrées semblaient assombrir son horizon.

Mes pensées vont finalement à ma famille, qui a dû supporter mon humeur suivant parfois les courbes de convergence irrégulières du logiciel de modélisation, ainsi qu'à mes amis, qui ont sû avec brio me changer les idées lorsque c'était nécessaire. J'espère du fond du cœur que cet ultime projet à l'EPFL saura être à la hauteur de l'attention que toutes ces personnes m'ont portée.

Ecublens, le 18 juin 2023

Abstract

The need to maintain and expand hydraulic structures is a major challenge for the coming energy transition, especially in Western countries. One technique already widespread allowing to meet these issues consists in the use of geomembranes to overcome problems of permeability or deterioration of traditional linings. A recent development is the use of these geomembranes in pressure tunnels and penstocks in hydroelectric schemes in the form of geomembrane systems to increase their productivity and durability. However, although a few application cases have already been identified, little is known about the behavior of these geomembrane systems when faced with the high pressure and velocity flow that takes place in these pressure waterways and therefore very few technical recommendations are available for the installation of these systems. An in-depth study of the dynamic behavior of geomembrane systems when subjected to pressurized flow is therefore necessary to better understand how these systems interact with the flow, and in particular under what conditions membrane vibrations, potentially dangerous to the integrity of the structure, are likely to occur.

The aim of this work is to contribute to this broad study of the dynamic behavior of geomembranes in pressurized flows by building a numerical model to simulate this problem, and to present the various issues and difficulties involved in its construction. The report details particularly how to take into account the hyperelastic behavior of the geomembrane material, how to define a mesh and load configuration that enable the membrane to withstand the high sollicitations imposed, and how to model the influence of the flow on the geomembrane and vice versa using the system coupling. Some preliminary results from the tests carried out show the consequences of the choices made, and give an idea of the capabilities and limits of the model. Indeed, the model still has its limitations, since, as explained in detail in this report, its development has proved far more difficult than anticipated, and numerous problems have arisen which have had to be resolved.

Résumé

La nécessité de maintenir et de développer les structures hydrauliques est un défi majeur pour la transition énergétique à venir, en particulier dans les pays occidentaux. Une technique déjà largement répandue permettant de répondre à ces enjeux consiste en l'utilisation de géomembranes pour surmonter les problèmes de perméabilité ou de détérioration des revêtements traditionnels. Un développement récent est l'utilisation de ces géomembranes, sous la forme de systèmes de géomembranes, dans les galeries d'amenée et les conduites forcées des aménagements hydroélectriques afin d'augmenter leur productivité et leur durabilité. Cependant, bien que quelques cas d'application aient déjà été identifiés, le comportement de ces systèmes de géomembranes confrontés à des écoulements à haute pression et à grande vitesse est encore fort méconnu et, par conséquent, très peu de recommandations techniques sont disponibles pour l'installation de ces systèmes. Une étude approfondie du comportement dynamique des systèmes de géomembrane lorsqu'ils sont soumis à un écoulement sous pression est donc nécessaire pour mieux comprendre comment ces systèmes interagissent avec l'écoulement, et en particulier dans quelles conditions les vibrations de la membrane, potentiellement dangereuses pour l'intégrité de la structure, sont susceptibles de se produire.

Le but de ce travail est de contribuer à cette large étude du comportement dynamique des géomembranes dans les écoulements sous pression en construisant un modèle numérique pour simuler ce problème ainsi que de présenter les différents enjeux et difficultés liés à sa construction. Ce rapport détaille notamment comment prendre en compte le comportement hyperélastique du matériau constituant la géomembrane, comment définir un maillage et une configuration de charge permettant à la membrane de résister aux fortes sollicitations imposées, et comment modéliser l'influence de l'écoulement sur la géomembrane et vice-versa en utilisant le couplage système. Quelques résultats préliminaires des tests réalisés montrent les conséquences des choix effectués et donnent une idée des capacités et des limites du modèle. En effet, le modèle a encore ses limites car, comme expliqué en détail dans ce rapport, son développement s'est avéré beaucoup plus difficile que prévu, et de nombreux problèmes ont surgi qui ont dû être résolus.

Contents

List of Figures

List of Tables

List of Symbols

Symbol	Definition	Unit	Reference
t	Time	s	-
g	Gravity	m·s^{-2}	-
s	Span length	m	-
c	Chord length	m	-
σ	Stress	Pa	-
W	Strain energy density function	Pa	(Beatty, 1987)
ε	Strain	-	-
F	Deformation gradient	-	(Wex et al., 2015)
J	Jacobean determinant	-	(Beatty, 1987)
x	Spatial position	m	(Wex et al., 2015)
X	Materail coordinate	m	(Wex et al., 2015)
U	Right positive symmetric stretch tensor	-	(Wex et al., 2015)
V	Left positive symmetric stretch tensor	-	(Wex et al., 2015)
R	Orthogonal rotation tensor	-	(Wex et al., 2015)
N_i	Eigenvectors of U	-	(Wex et al., 2015)
n_i	Eigenvectors of V	-	(Wex et al., 2015)
$\lambda_1, \lambda_2, \lambda_3$	Principal stretches, eigenvalues of the stretch tensor	-	(Wex et al., 2015)
B	Left Cauchy-Green deformation tensor	-	(Khaniki et al., 2022)
I_1, I_2, I_3	Invariants of the Cauchy-Green deformation tensor	-	(Ali et al., 2010)
C_{ijk}	Material constant related to shear behavior	Pa	(Ali et al., 2010)
$\overline{U}$	Invariants related strain energy density function	Pa	(Ali et al., 2010)
$\widetilde{U}$	Principal stretches related strain energy density function	Pa	(Ali et al., 2010)
k	Stiffness	Nm^{-1}	(Lestuzzi and Smith, 2019)
c	Damping constant	kg·s^{-1}	(Lestuzzi and Smith, 2019)
m	Mass of a SDOF system	kg	(Lestuzzi and Smith, 2019)
ω_n	Circular frequency	rad·s^{-1}	(Lestuzzi and Smith, 2019)
f_n	Natural frequency	s^{-1}	(Lestuzzi and Smith, 2019)
ξ	Damping factor	-	(Lestuzzi and Smith, 2019)
ω_D	Pseudo-pulsation	rad·s^{-1}	(Lestuzzi and Smith, 2019)
Ω	Membrane	-	(Greiner, 2010)
$\partial\Omega$	Membrane boundary	-	(Greiner, 2010)
φ_m	Membrane density	kg·m^{-3}	(Greiner, 2010)
Ψ	Membrane vertical displacement	m	(Greiner, 2010)
T	Tension induced in the membrane		(Greiner, 2010)
v	Wave velocity	m·s^{-1}	(Greiner, 2010)
ω	Pulsation of the harmonic force	rad·s^{-1}	(Lestuzzi and Smith, 2019)
F_0	Amplitude of the harmonic force	N	(Lestuzzi and Smith, 2019)

R_d	Dynamic amplification factor	-	(Lestuzzi and Smith, 2019)
h	Membrane thickness	m	(Tiomkin and Raveh, 2021)
φ	Fluid density	kg·m⁻³	(Tiomkin and Raveh, 2021)
U	Fluid velocity	m·s⁻¹	(Tiomkin and Raveh, 2021)
α	Angle of approach	rad	(Tiomkin and Raveh, 2021)
Δp	Hydrodynamic load	Pa	(Tiomkin and Raveh, 2021)
μ	Dynamic fluid viscosity	kg·m⁻¹·s⁻¹	-
u	Overall fluid velocity vector	m·s⁻¹	(Ansys, 2021a)
S_m	Source term for added mass	kg·m⁻³·s⁻¹	(Ansys, 2021a)
p	Static pressure	Pa	(Ansys, 2021a)
τ	Deviatoric stress tensor	Pa	(Ansys, 2021a)
k_{eff}	Effective conductivity	W·m-1·K	(Ansys, 2021a)
k_t	Turbulent thermal conductivity	W·m-1·K	(Ansys, 2021a)
S_h	Source term for added heat	W·m⁻¹·s⁻¹	(Ansys, 2021a)
H	Total enthalpy	J	(Ansys, 2021a)
e	Internal energy	J	(Ansys, 2021a)
p_{op}	Operating pressure	Pa	(Ansys, 2021a)
p_g	Gauge pressure	Pa	(Ansys, 2021a)
N_{faces}	Number of faces enclosing the cell	-	(Ansys, 2021a)
E	Young's modulus	Pa	(Ansys, 2023a)
ν	Poisson's ratio	-	(Ansys, 2023a)
$\underline{K}$	Total stiffness matrix	Nm⁻¹	(Ansys, 2023a)
f	Vector of external forces	N	(Ansys, 2023a)
$\underline{M}$	Structural mass matrix	kg	(Ansys, 2023a)
$\underline{C}$	Structural damping matrix	kg·s⁻¹	(Ansys, 2023a)
$\underline{K}^c$	Current stiffness matrix	Nm⁻¹	(Ansys, 2023a)
$\underline{K}^s$	Stress stiffness matrix	Nm⁻¹	(Ansys, 2023a)

Chapter 1   Introduction

Water has always been a precious resource closely linked to human activity and survival. As water supplies are very unevenly distributed around the globe, the capacity to store and transport these supplies in space so that the population can satisfy its primary needs at all times soon proved to be essential for the prosperity of society. The first waterworks were therefore aimed primarily at guaranteeing a sufficient supply of water for consumption and irrigation. However, although water is essential to the survival of the human race, it also brings with it its share of dangers. Protection against the risk of flooding or the reclamation of marshy areas became a major issue, from which the first dams and water channeling infrastructures were created. The use of water bodies for navigation and recreation also led to the need for infrastructure to meet these usages. Finally, the promising energy potential of water has necessitated the development of facilities to harness water power, first for mechanical work and then for electricity generation. The evolution of hydraulic engineering therefore says a lot about the development of society, and it has more than ever played a major social and economic role in it (Moran et al., 2018).

1.1   Ageing of the hydropower plants

The exploitation of water power for energy purposes is not a recent idea, but the need for an energy transition towards renewable and indigenous energies has brought hydroelectric production back to the forefront (Berga, 2016). This awareness of the importance of this source of supply and therefore the importance of the facilities guaranteeing its production coincides with the end of the initial concessions for a large part of them. As most of these facilities were granted an initial concession of fifty or eighty years, the current challenges are related to the renewal of this concession. Several factors come into play when determining the renewal and the new duration of the concession, but probably one of the most decisive is the current degree of deterioration of the structure and its capacity to last over time. Indeed, the majority of facilities are designed to guarantee a lifespan of fifty years or a hundred years for large structures and these structures start to be considerably worn (Perera et al., 2021).
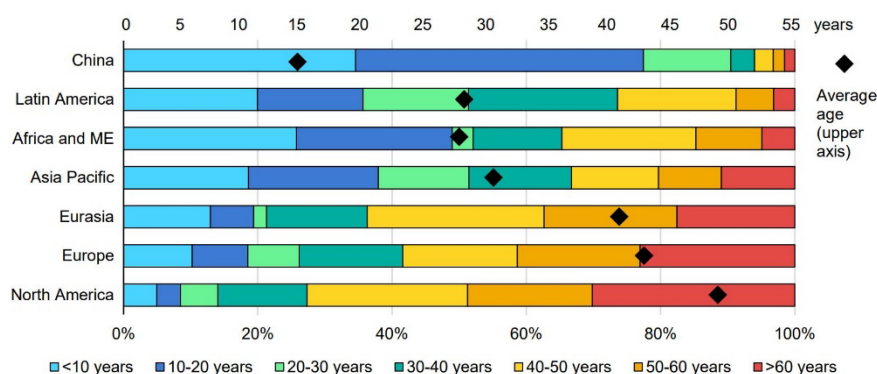
Figure 1: Age profile of installed hydropower capacity in 2020 (reprinted from International Energy Agency, 2021)

Figure 1, taken from the International Energy Agency (IEA) Hydropower Special Market Report dated June 2021, shows the age distribution of the various hydroelectric power plants present worldwide based on installed capacity and grouped here by geographic region.

This representation clearly shows the general ageing of hydroelectric power plants built in countries with a developed economy. Most of these facilities date back to the large wave of construction that took place between the 1960s and 1980s (Perera et al., 2021). Thus, North America and Europe are home to the oldest structures, with 70% and 60% of facilities respectively being at least 40 years old. As a result, more than 40% (476 GW) of the global fleet is at least 40 years old, bringing the average age to 32 years. In contrast, China, which has the largest installed hydropower capacity of all the regions studied (International Hydropower Association, 2022), has experienced extremely rapid development in recent years and therefore has the youngest schemes.

The International Energy Agency considers that power plants that are between 45 and 60 years old require significant investments for their renovation in order to modernize them, improve their performance or increase their flexibility. Thus, simple renewal of the main equipment such as turbines or generators must be accompanied by studies aimed at developing ways to modernize and digitalize the hydropower plant in order to make it safer, more flexible and better able to respond to the various environmental and social issues that govern its operation (Botelho et al., 2017). In particular, these studies must ensure that the plant complies with local legislation regarding drought management and flood protection. The amount invested in the renovation of the structures and the objectives of this campaign must be the subject of a profitability study to ensure that these investments are proportionate and provide a sufficient return on investment to justify the capital expenditure. In addition, it is also necessary to ensure that the possible production and economic costs associated with the work are bearable for the company and in particular for the plant operator. Therefore, in order to limit these losses, it is essential to establish a detailed schedule of any intervention campaign on the hydropower plant that could disrupt its operation so that these works are as efficient and brief as possible.
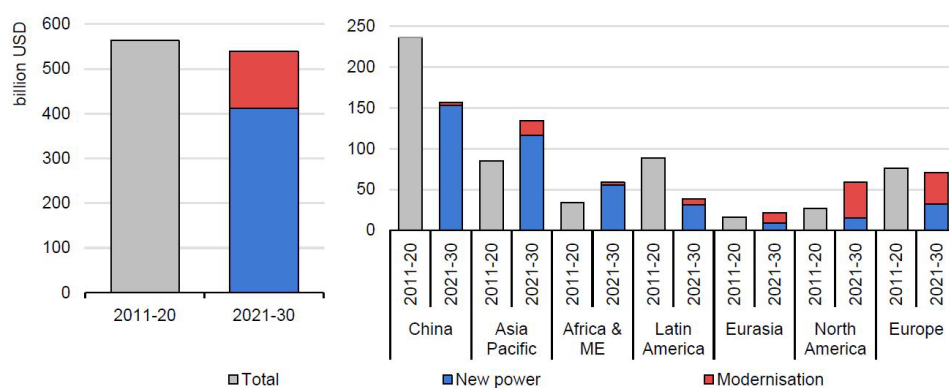
Figure 2: Hydropower capacity investment (reprinted from International Energy Agency, 2021)

It appears from Figure 2, which shows the distribution of investments between construction and maintenance of power plants, and from the various observations made above that the first built hydropower plants, mainly present in North America, Europe and Eurasia, are in a decisive period for their future. Indeed, these schemes have reached the end of their initial operating life and their future use must be redefined. A complete review of the state of the power plants must be carried out to determine the degree of degradation and the agreements governing their exploitation must be rediscussed. In the event that work is required, the cost and extent of the work will be a determining factor in deciding whether or not to continue operating the structure. There is therefore a real need for rehabilitation techniques that allow the scheme to be renovated while limiting the costs of the work and the duration of the plant's shutdown.

1.2   Challenges for the hydropower development

This need for rehabilitation is compounded by an additional challenge. Indeed, as shown in Figure 3 from the Hydropower 2050 report of the International Hydropower Association (IHA), there are regions where the hydropower potential is largely under-exploited, as is the case in Africa, but in other regions, particularly in Europe, the remaining potential to be exploited is relatively small compared to the capacity already installed. This means that the optimal locations from an energy production point of view are already largely equipped with power plants in Europe and that the remaining potential is scattered over large parts of the territory. In order to achieve a transition to renewable sources of electricity generation, it is often more profitable to optimize the operation of existing infrastructures, which have better conditions in terms of water supply or head, than to develop expensive new construction projects, which would be less advantageous than existing facilities. Thus, while certain regions of the world such as Asia or Africa are experiencing the construction of numerous new dams and hydroelectric plants, the trend in Europe is rather to seek an increase in the efficiency or flexibility of existing plants (Quaranta et al., 2021).
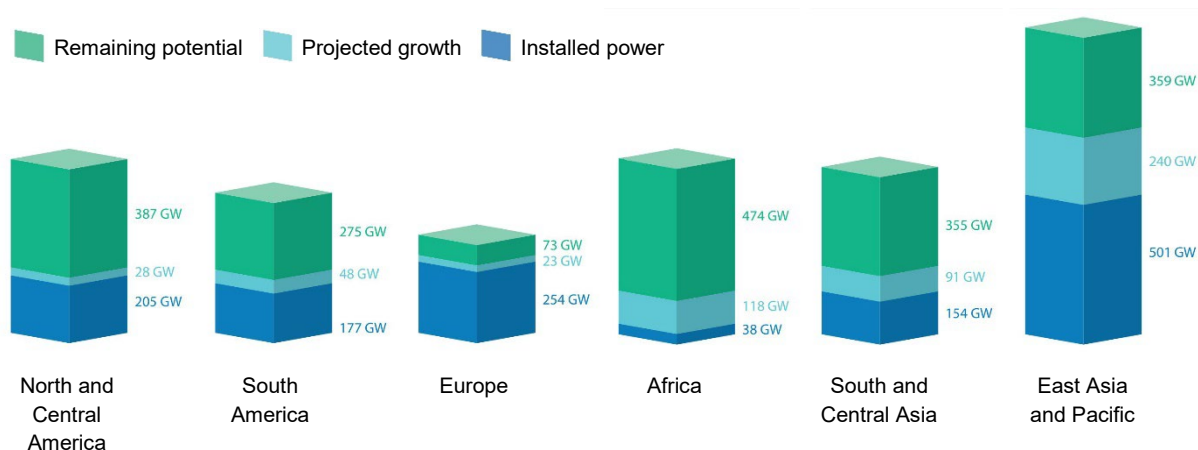
Figure 3: Remaining potential for hydropower development (adapted from International Hydropower Association, 2023)

This pressure to increase hydroelectric power generation, largely through the optimization of existing facilities, is even more important in Switzerland, since these ambitions are enshrined in law. Indeed, after the nuclear disaster in Fukushima in 2011, the Federal Council and Parliament decided to phase out the production of electricity from nuclear power plants (Swiss Federal Office of Energy, 2019). Following this decision, the Federal Council has drawn up an energy strategy that sets targets for the energy supply to be achieved by 2050. Thus, on May 21, 2017, the Swiss people accepted the revision of the Energy Act (LEne), which went into effect on January 1, 2018. This strategy contains a whole series of measures in the fields of energy efficiency, renewable energies, nuclear power and electricity grids. With the Energy Strategy 2050, Switzerland intends to reduce its dependence on imported fossil fuels and to strengthen domestic renewable energies. Hydropower plays an important role in this.

Following the Energy Strategy 2050 (SE 2050), Parliament has set the indicative value for the average annual production of electricity from hydropower for 2035 at 37,400 GWh in the Energy Act (Art. 2, para. 2, LEne). This value was calculated on the basis of an analysis of hydroelectric potential carried out in 2012 by the Swiss Federal Office of Energy (SFOE).

In order to reach this value, a net increase of about 2000 GWh is required between the base year 2011 (35,350 GWh) and 2035. According to the message on the Energy Strategy 2050, the Federal Council expects an average annual hydroelectric production of 38,600 GWh in 2050. In order to achieve this goal, an increase in production of about 3200 GWh is necessary.

In the study on Switzerland's hydropower potential published in 2012 and updated in 2019, the potential is defined as follows: the theoretical potential is the total physical supply of a type of renewable energy in the region under consideration, regardless of the actual restrictions imposed on exploitation. The technical potential is the share of the theoretical potential that can be realized within the technical constraints. The expected potential is the share of the technical potential that meets the criteria of economy, ecology and social acceptability. It is precisely this expected potential that is quantified in the 2012 and 2019 reports and whose main results are summarized in Table 1 below.

Table 1: Comparison of total potential to 2050 in the 2012 and 2019 studies
(adapted from Swiss Federal Office of Energy, 2019)

	Optimized operating conditions (2012)	Optimized operating conditions (2019)
New large power plants	1430	1380
Renovation and expansions of large plants	1530	1530
Small hydropower (constructions, renovations and expansions)	1600	770
Disappearance of small plants	0	-220
Residual flows	-1400	-1900
Total potential	**3160**	**1560**
Increase in hydroelectric production between 01.01.2012 and 01.01.2019	640	
New glacial lakes		700

Unit: [GWh/y]

It should be noted that the numbers contained in Table 1 have been established considering only the potential of the projects that have been unveiled and that the potential of new glacial lakes has not been taken into account in the establishment of the optimized conditions for 2019. The production potential for the year 2019 presented in Table 1 could thus be several hundred GWh higher annually.

Several conclusions can be drawn from the numbers presented in Table 1. First of all, these values clearly show that in order to achieve the production targets set, additional measures are imperatively required. In order to achieve the development target, the electricity industry must assume its responsibility for security of supply and contribute to the transformation of the Swiss energy system by investing in new projects and upgrading existing facilities. The sustainable development of hydropower also requires that additional measures be taken to resolve conflicts of interest between the use of hydropower and water protection. Secondly, these results show that the target value set in Art. 2 of the LEne to be achieved by 2035 is realistic at the present time. However, in order to achieve this value, the identified potential must be almost fully realized by 2035, which means that the current average growth of 87 GWh (Swiss Federal Office of Energy, 2019) must continue in the coming years.

Then, it can be seen that taking into account the increase in production since January 2012, the total potential has decreased by 960 GWh/year. This reduction mainly concerns small hydropower and is the result of the new configuration of the support system put in place since the revised version of the LEne came into force in 2018. In this case, it is up to the cantons, municipalities and the industry to propose solutions and make the necessary investments to realize the potential of small hydropower. Finally, the distribution of the potential in the different categories according to its origin confirms the trend already perceived on a European scale, namely that the optimization of existing facilities often has more to offer in terms of production than the construction of new facilities, while the costs of the works are generally lower. Indeed, Table 1 shows that the expected potential lies mainly in the renovation and expansion of existing large-scale plants. There are therefore important reserves to be exploited in the renovation and optimization of existing structures and real opportunities for any technological innovation made in this area.

1.3   Geomembrane systems

A technique that has recently been gaining ground allows to face the two challenges presented above, namely to preserve the durability of the infrastructure while increasing its performance. This technique consists in the installation of membranes on the damaged parts of existing structures but also preventively on the particularly exposed zones of new structures. These systems are coatings made of a thin membrane with a very low permeability in order to control the flow of fluids in a structure or a system, which can be reinforced by a geotextile (Scuero and Vaschetti, 2017). When these membranes are used in geotechnical applications, they are called geomembranes (Giroud and Perfetti, 1977).

The potential field of use of these geomembranes is very broad and is discussed in detail in Section 2.1.3, but in particular it is possible to use geomembranes in high head hydroelectric schemes. A diagram showing the general configuration of such facilities is shown in Figure 4.
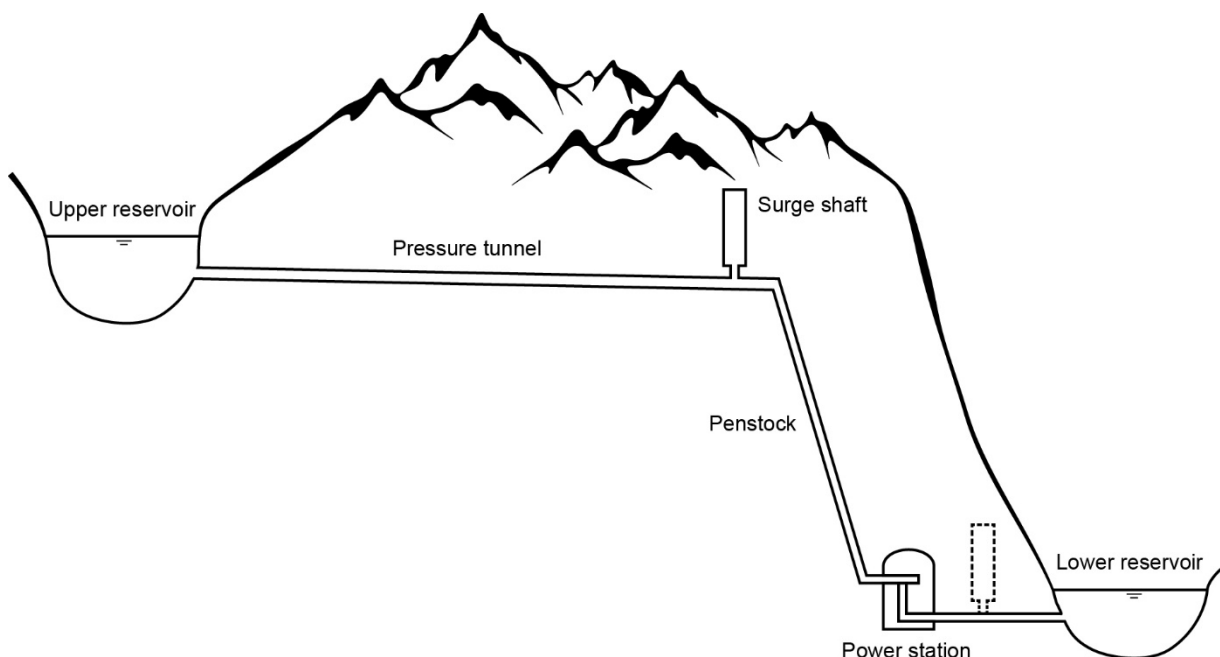
Figure 4: Schematic diagram of a high head hydropower scheme

These high head hydroelectric plants almost always have the same components. Upstream is a reservoir, usually formed by a dam, from which water is drawn by a submerged water intake. The captured water is then transported through a long, almost horizontal tunnel called the pressure tunnel. At the end of this tunnel there is a sudden break in the slope marking the beginning of the penstock, a pipe with a very steep slope responsible for carrying the water to the power station where it is turbined.

At the convergence between the pressure tunnel and the penstock, there is a surge tank which permits to control sudden changes in water discharge but whose role will not be detailed further in this work. Finally, after the power station, the water enters a tailrace tunnel and is returned to the environment, often in a river or lake. It may be important to note that the inclination of the pressure tunnel and the penstock are related to the topography of the land and especially to the technical constraints of excavation dating from the time of construction of the hydropower scheme. Today, it is possible to excavate inclined tunnels that do not divide into two segments as shown in Figure 4, but everything that will be said for the classic configuration is also valid for this possibility.

Within these high head schemes, chemical degradation of the concrete forming the gallery can be limited by placing a geomembrane system against the tunnel wall. This system stops the deterioration of the concrete and avoids the appearance of cracks that could jeopardize the safety of the structure and necessitate its complete shutdown for the rehabilitation of the tunnel. Some other advantages of installing a geomembrane is that it reduces water loss, especially at the joints between the concrete elements that could fail, or reduces the head losses caused by the roughness of the concrete and thus improves the productivity of the plant (Nogueira et al., 2016).
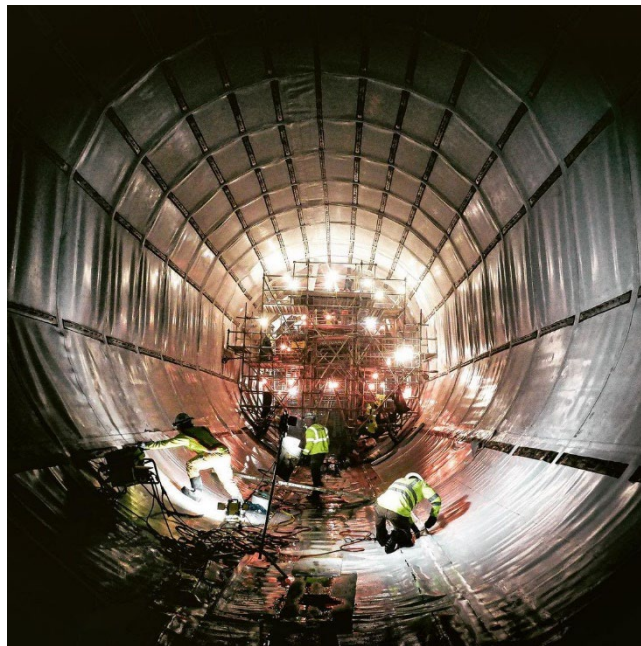
Figure 5: Geomembrane system in a penstock access tunnel. Image: courtesy of © Carpi Tech

Figure 5 shows the implementation of a membrane system within a penstock access tunnel. The relatively flexible membrane is fixed at points on the section by longitudinal anchors. In a circular tunnel, the membrane takes the shape of a polygon inscribed in this circle and whose vertices correspond to the attachment points between the geomembrane and the concrete lining of the tunnel.

1.4 Issues and potential problems

As shown in Figure 5, the membrane is in contact with the flow and these two media interact, the behavior of one influencing the behavior of the other. One could think that the water flow would simply press the membrane sections between the anchors against the tunnel wall but it turns out that these reciprocal influences induce temporal variations of the characteristics of each of these media, whether they are for example variations of the position or the constraints of the membrane, or of the flow lines within the fluid. The flow makes these different sections of geomembrane vibrate and risks to make appear a phenomenon of resonance. Indeed, if the frequency of the vibrations induced by the flow approaches the natural frequencies of the membrane, the amplitude of vibration of the membrane increases enormously. These very important vibrations could then damage the geomembrane, which would require its replacement at great expense. In addition, this phenomenon would create a resistance to the flow, which would increase the head loss and decrease the productivity of the system.

The study of these interactions belongs to the field of dynamics, a part of mechanics that seeks to characterize the temporal evolution of the behavior of one or more bodies. Studies concerning the behavior of membranes subjected to external stress have already been conducted in the fields of aeronautical engineering and even concerning submerged membranes (Gascón-Pérez, 2017; Li et al., 2021). However, these studies deal with membranes subjected to air pressure or to a pressure induced by water but hydrostatic. Indeed, the knowledge about the interactions between an initially planar but deformable system such as the geomembrane and a high pressure water flow is still quite precarious. This gap in the studies of the behaviour of geomembranes in such environments results in a lack of guidelines for the companies and practitioners installing such equipment

1.5 Objective and organization of the report

The aim of this work is to contribute to the broad study of the dynamic behavior of geomembranes in pressurized flows by building a numerical model to simulate this problem, and to present the various issues and difficulties involved in its construction.

In order to gain a better understanding of the problem, a literature review is first carried out in Chapter 2, presenting the various characteristics of geomembranes, typical application cases and the main properties of the hyperelastic material of which geomembranes are made. Chapter 3 then details some of the theoretical foundations needed to understand the dynamic behavior of a membrane, and the equations governing its motion in the free and forced cases. Chapter 4 is the mainstay of this work. It explains how the numerical software used for simulation works, and details the way in which the model is built. In particular, this chapter shows the reflection behind the development of the model and how the choices made are implemented in the model. Some preliminary results are presented and commented on in Chapter 5, before the model's capabilities and limitations are discussed in Chapter 6.

Chapter 2   Literature review

2.1   Overview of geomembrane systems

2.1.1   Geomembrane

First of all, it should be recalled that a membrane is a thin and flexible two-dimensional sheet that can deform or vibrate when excited by an external force and used to separate two domains of a mechanical assembly. Geomembranes are a specific type of membrane as they are synthetic and manufactured sheets used in geotechnical engineering. Indeed, only membranes used in this field should be called geomembranes (Giroud, 1984). One of their main characteristics is their extremely low permeability which justifies their use as a barrier to fluid migration. Geomembranes are thus mainly used as barriers to contain liquids, redirect their flow or prevent their migration (Giroud, 2016). In hydropower, it is possible to find them as an impervious layer in hydraulic canals, reservoirs, on the face of dams or in pressure waterways and surge shafts as detailed in Section 2.1.3. They are a cost-effective and efficient solution to prevent design and construction delays, minimize outage loss and repair and maintenance costs, and other consequences of a failure that could be caused by a minor leak (Cazzuffi et al., 2012b).

The quasi-impermeable property of the geomembrane is due to the use of a polymer or bitumen material in their constitution. These two potential components both belong to the family of geosynthetic materials which are man-made synthetic products used to improve soil conditions and can have either high or low permeability as indicated on Figure 6. Even if it is true that geomembranes can be composed of bitumen material, bituminous geomembranes are mainly used for dams applications but still represent less than 8% of the cases of application (ICOLD, 2010). It can therefore be admitted that the geomembranes used in hydropower are mainly polymeric geomembranes. Several types of polymers divided into different categories according to their properties are used as constituents for geomembranes.
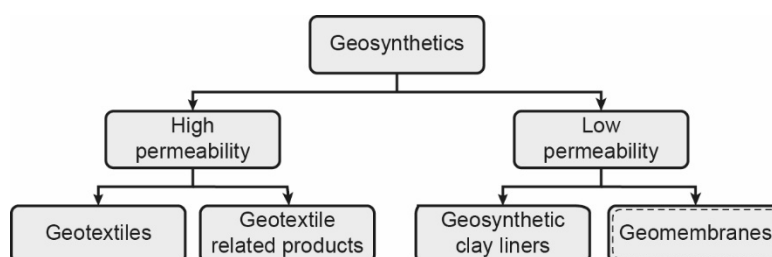
Figure 6: Classification of geosynthetic materials (adapted from Shukla and Yin, 2006)

The most frequently used polymers belong to the family of thermoplastics, materials whose flexibility and softness vary with temperature, increasing when the material is heated and decreasing when it is cooled (Marence et al., 2020). In this category are polymeric geomembranes composed of polyvinyl chloride (PVC) and polyolefin materials (PO). A variety of chemical and mineral additives are incorporated in the polymer geomembranes to improve some of their properties (Giroud, 2016). Polymers are usually compounded with various additives such as fillers, fibers, carbon black, plasticizers, stabilizers, antioxidants, fungicides and other polymers to perform various functions without altering the very low permeability of the base product.

Based on this, a difference is made between non-plasticized and plasticized PVC membranes, in which plasticizers are added to make the membrane softer and more flexible. Polyolefin membranes include two different types of plastic resins. There are polypropylene (PP) and polyethylene (PE) geomembranes, which are divided into high density (HDPE) and low density (LDPE) geomembranes. A summary of the different types of geomembranes is shown on Figure 7.
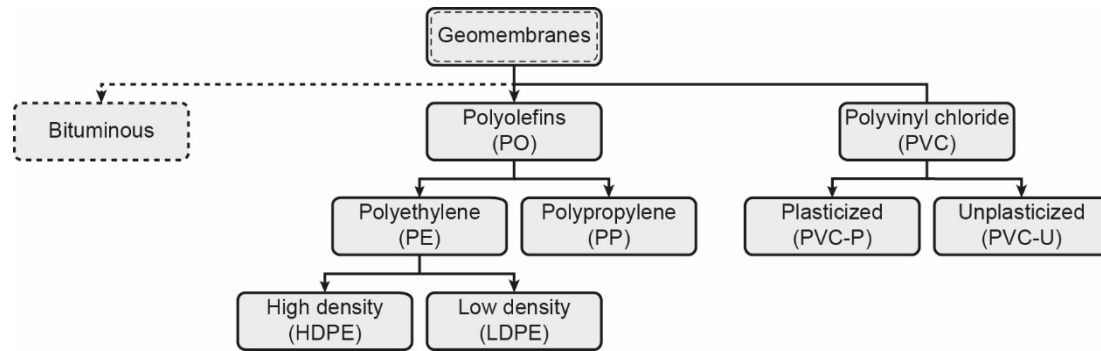
Figure 7: Classification of the most common geomembranes used in hydropower (adapted from Marence et al., 2020)

The type of geomembrane used on a structure depends on the characteristics of the structure and the year it was installed. Indeed, while the types of membranes installed on dams are very diverse (Cazzuffi et al., 2010), the membranes installed in hydraulic tunnels and shafts are almost all PVC geomembranes (Scuero and Vaschetti, 2021). The most widely used geomembranes in hydropower are PVC-P geomembranes (ICOLD, 2010; Marence et al., 2020).

2.1.2 Geomembrane systems

Geomembrane is often used in combination with other geosynthetic materials to form the geomembrane system, also sometimes called the geomembrane sealing system, which is therefore a particular form of geocomposite. In general, geomembrane systems are composed of several layers of different geosynthetic materials, one of which being the geomembrane that gives the system its name. Each layer has its own function and contributes to strengthen the overall system, whether in its construction, its placement or in the preservation of the sealing of the structure (ICOLD, 2010).

The layout of the geomembrane system can result in several configurations. First, it is possible to simply apply the membrane composed of a homogeneous material against the initial surface without any reinforcement. A second possible configuration is to optimize the surface in contact with a particularly harsh environment to address any durability issues that may be encountered by adding one or multiple layers of the same material or different materials. This method is particularly used when the membrane is in the open air and exposed to U.V. When the geomembrane is highly stressed, it is possible to incorporate a scrim made out of polymeric materials such as glass fibers, synthetic threads, fundamentally polyester threads, veils or fabric that improves the mechanical properties of the system.

Figure 8: General configurations of the geomembrane system (adapted from ICOLD, 2010)

Finally, a widely used arrangement is to back the geomembrane with fabrics or other reinforcements. It is very common in the field of hydraulic infrastructures to place a geotextile backing between the membrane and the application surface. The first time geotextiles were used to protect geomembranes was in a series of reservoirs in 1971 (Giroud, 1984) for which the purpose of this association was to prevent direct contact between a geomembrane and sharp stones that could puncture the membrane. But the addition of a geotextile not only reduces the risk of punctures, it also provides stability to the compound during the manufacturing process, increases tensile strength, tear and burst strength, and modulus, and provides or increases dimensional stability to geomembranes that would otherwise shrink or expand as a result of temperature changes. Other advantages of the use of a geotextile are that it acts as a drainage medium, since its in-plane transmissivity characteristic can conduct water or gases away from direct contact with the geomembrane, it increases friction against sliding and especially it improves the stress distribution underneath the geomembrane, protecting it from mechanical damages (ICOLD, 2010).

Similar to what has been said about geomembranes, geotextiles are textiles (fabrics) used in geotechnical engineering. Like geomembranes, they are thin, two-dimensional and flexible geosynthetic materials. But while geomembranes are designed to have the lowest possible permeability, geotextiles are permeable by construction. There are about twenty different types of geotextiles but they can be divided into two main classes: the classical geotextiles and the special geotextiles (Giroud, 1984). The classical geotextiles are the typical products of the textile industry and include woven, knitted and nonwoven fabrics. The latter type of geotextile is particularly relevant to study because it is the one most used in combination with a geomembrane (ICOLD, 2010). A nonwoven geotextile is a planar, permeable, polymeric textile material taking the form of a manufactured sheet, web or batt of directionally or randomly oriented fibers, filaments or other elements. The filaments or the short fibers are first arranged into a loose web and then bonded together using one or a combination of bonding processes.
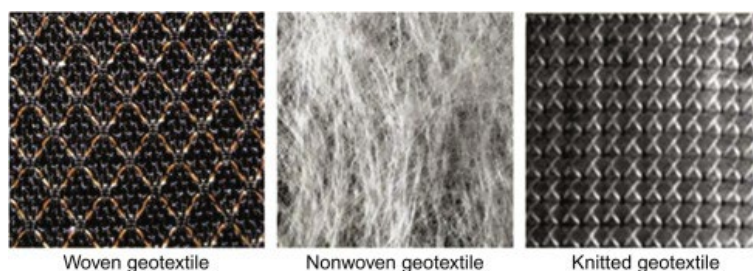
Figure 9: Close-up view of the different variant of geotextile (reprinted from Manik et al., 2023)

There are three main processes used for the production of nonwoven geotextiles (Rawal et al., 2016). Chemical bonding consists of adding a binder such as glue, rubber, casein, latex, cellulose derivative or a synthetic resin in order to bond the filaments or short fibers together and obtain a chemically bonded nonwoven geotextile. A second process called thermal bonding relies on the application of heat causing partial melting of the filaments or short fibers which makes them adhere together at their crossover points. The resulting heatbonded nonwoven geotextile is usually relatively thin. The last process is a mechanical process divided into two sub-categories, i.e. needlepunching and hydroentanglement. The difference in mechanical bonding techniques relies on the utilization of metal needles in needlepunching, whereas high-pressure multiple rows of water jets are used to reorient and entangle a loose array of fibres into self-locking and coherent fabric structures in a hydroentanglement process (Manik et al., 2023).

2.1.3 Hydropower applications of geomembrane systems

In its general use, the main function of the geomembrane system is often to provide a more watertight surface to which it is applied. This improved waterproofing is achieved by two different contributions. Firstly, the permeability of the membrane is very low and very often lower than the permeability of the surface on which it is applied. Thus, the installation of the membrane between the fluid and the initial surface reduces the loss of fluid by infiltration and leakage through the medium containing the fluid (Giroud, 2016).

Then the installation of the membrane makes it possible to compensate for the various punctual structural imperfections induced in particular by the mechanical or chemical action of the fluid. In particular, the geomembrane is capable of filling cracks caused by wear and tear of the material or exceptional events such as an earthquake, and thus of preventing water from seeping into these cavities. This waterproofing property of the geomembrane is exploited in many applications and in particular in reservoirs in order to fight against water leakage as illustrated in Figure 10.

Figure 10: Geomembrane system in an upper reservoir in pumped-storage plant in Portugal. Image: courtesy of © Carpi Tech

In addition to solving the various problems of permeability of the structure, the geomembrane also makes it possible to remedy the complications linked to the chemical interactions mentioned above. As the vast majority of hydraulic installations are built in concrete, they suffer from all the pathologies associated with the use of this material. These can even be accentuated by the various flooding and dewatering cycles to which the structures are exposed. Hydraulic structures are therefore subject to chemical aggression linked to the presence of water. In particular, it can be affected by alkali-aggregate reactions, chloride ions in the case of contact with salt water or suffer from carbonation. The installation of a geomembrane at the interface between the structure and the water thus creates a barrier between the two and protects the material from the various harmful effects of the water. As the concrete is not in direct contact with the water, it is less likely that the various pathologies mentioned above will develop. This protective capacity justifies the use of geomembrane systems in many cases of upstream dam face rehabilitation (Cazzuffi et al., 2010), such as the one shown in Figure 11.

Figure 11: Dam rehabilitation in the USA. Image: courtesy of © Carpi Tech

The installation of a geomembrane can also have another positive impact on the productivity of a hydroelectric scheme. Indeed, the presence of a low roughness membrane between the flow and the initial wall allows to decrease the friction between the water and the surface containing it and thus to increase the energy produced by the plant. However, since the membrane has a certain thickness, its installation generates a reduction of the flow section. This reduction of the section implies, for an equal velocity, a decrease of the flow and thus of the energy production. The potential gain in productivity therefore depends primarily on the configuration of the plant and the geometry of the pipe, but the installation of a geomembrane system would generally be beneficial from a strict productivity standpoint for the vast majority of Swiss facilities. This potential for friction reduction is beginning to be exploited as some cases of application of geomembrane systems in pressure waterways are occurring around the world (Marence et al., 2020).

Figure 12: Installation of a geomembrane system in a pressure tunnel. Image: courtesy of © Carpi Tech

Figure 12 above shows the installation of one of these geomembrane systems in a pressure tunnel. The issues associated with the use of geomembrane systems in this configuration and the details of their installation and behavior are discussed in Section 2.2.

2.2   Exposed geomembrane systems in pressure waterways

2.2.1 Interest of exposed geomembrane systems

As shown in Figure 4, hydraulic tunnels are responsible in hydroelectric schemes for transporting water from the upper reservoir to the power station to enable electricity generation. The flow in them is mostly in the form of pressurized flow, which is why the tunnels are often called pressure waterways. This type of flow contains large amounts of energy and is often characterized by relatively high velocities and very high Reynolds numbers. Indeed, for a design flow, the velocities can reach several meters per second and the Reynolds number can have an order of magnitude of $Re = 10^7$.

These pressure waterways are typically lined for several reasons (Cazzuffi et al., 2012b). First, this lining ensures the structural safety of the excavation by supporting the ground which may be unstable. Secondly, the lining in pressure waterways has an important waterproofing function that prevents operating water from escaping from the tunnel into the surrounding ground or external fluids, which may potentially contain deleterious chemicals, from entering the tunnel and damaging the structure. Finally, the lining is in charge of minimizing energy losses by increasing the hydraulic efficiency of the excavation obtained by reducing the friction at the interface between the water flow and the structure (Nogueira et al., 2016). Pressure waterways linings are traditionally made of steel, cast in situ concrete or sprayed concrete but each of these materials has its drawbacks. Steel has all the qualities of a good lining mentioned above, but the thickness required to achieve them makes it an economically unviable solution since the material is expensive and time consuming to install. On the contrary, concrete is cheap and easy to install but is rarely free of defects such as voids or cracks that usually appear as a consequence of thermal stresses or poor constitution and construction. Furthermore, concrete linings are sensitive to the dynamic action of water and cracks or crazing can result from the deterioration of the concrete by water during operation thus increasing the permeability of the concrete and increasing its roughness, thus inducing poor hydraulic conditions. The loss of water in the surrounding ground is all the more detrimental as it can jeopardize the stability of the ground and of the structure itself (Enzinger and Cerjak, 2006). Furthermore, cracks appearing in the concrete lining allow groundwater to act as a hydraulic jack and affect the durability of the reinforcement (Cazzuffi et al., 2012b).

In view of the shortcomings of traditional linings, the geomembrane systems presented in Section 2.1.2 are a particularly suitable alternative. Indeed, their flexibility and affordability make them a promising mitigation and rehabilitation technology perfectly suited to overcome the problems posed by concrete or steel linings. The geomembrane systems are rapid to install and their modular composition allows them to be installed in stages to best meet operating requirements, thus reducing the plant's downtime and limiting the dewatering duration. When properly sized, these systems are very durable and can last for decades without the need for planned, routine or preventive maintenance. This long service life at low maintenance levels coupled with lower installation costs than other lining systems makes geomembrane systems an economically very attractive solution. In addition, these systems offer more advantageous hydraulic properties than traditional pressure waterways linings. Their very low permeability greatly reduces water loss, thus optimizing hydropower operations and their low roughness reduces frictional losses, thus increasing the productivity of the plant. Finally, geomembrane systems can also act as a protective layer to prevent further degradation of the existing lining.

2.2.2 Historical development

Although little known to the general public, the use of geomembrane systems for the mitigation and rehabilitation of hydraulic structures is a technology that has been in use for more than seventy years and whose satisfactory results have led to its expansion to its use throughout the world today. The first uses of these systems were to ensure the imperviousness of hydraulic channels and reservoirs, thus for free surface flows (Cazzuffi et al., 2012a). However, geomembranes remained exclusively used for open air flows for more than twenty years. In fact, it was not until 1969 that the first appearance of a synthetic geomembrane in a subway station in Vienna, Austria, heralded the beginning of the popularization of the use of geomembrane systems in the underground environment (Cazzuffi et al., 2012b). The first documented use of a geomembrane system for pressure flows was in 1984 in the Gandellino and Gorghiglio tunnels in Italy (Cazzuffi et al., 2012b). The development of this technology allowed its implementation in some high-pressure tunnels at the end of the 1990s, such as the Thisavros tunnel in Greece in 1996 (Scuero and Vaschetti, 2021). The success of these first projects led this technology to spread and to be used in many others, being now also applied in vertical shafts such as pressure shafts and surge shafts as in Colombia in the Tunjita hydropower plant in 2017 or the Gilboa pumped-storage plant in Israel in 2018. Given the context presented in the introduction encouraging the rehabilitation of existing developments, it is likely that geomembrane systems will continue to evolve by developing the technical characteristics of the product to best meet the growing demand.

2.2.3 Layout and design

The layout of the geomembrane system can also take two different forms (Cazzuffi et al., 2012b). Firstly, the geomembrane system can be applied as a covered system. This covered solution is typically adopted in new tunnels but can also be used as a rehabilitation measure in particularly deteriorated cases requiring major works. In a covered system, the geomembrane system is placed between the outer sprayed concrete layer and the inner concrete lining. The geomembrane is thus protected by overlying layers and is not in direct contact with the flow. In this configuration, the membrane is not attached to the geotextile but is placed over an independent anti-puncturing layer of geotextile and has the main objective of increasing the impermeability of the overall system.

It is also possible to place the geomembrane system directly against the tunnel walls. This exposed configuration can be used both in structures requiring rehabilitation and in new construction, although its relative ease of installation makes it a technique more commonly used in restoration work. In this solution, the geomembrane is in direct contact with the flow and is therefore subject to challenging conditions, mainly characterized by the dynamic actions of high flow velocities and by high hydrostatic and hydrodynamic pressures. Although it is possible in some cases to place the geomembrane system specifically on a damaged area, in the vast majority of cases the geomembrane system covers the entire section and thus extends over relatively large distances within the tunnel. The geomembrane system usually consists of a PVC membrane bonded to a non-woven, needlepunched geotextile made of polypropylene (Vaschetti, 2022) to form a geocomposite.
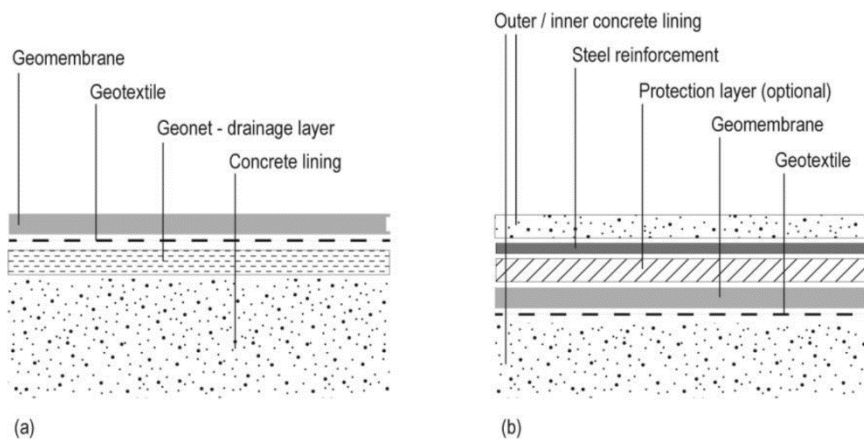
Figure 13: Schematic drawing of the composition of (a): exposed geomembrane systems and (b): covered geomembrane systems (reprinted from Vorlet and De Cesare, 2023 (under review))

The design for geomembrane systems in pressure tunnels and shafts meets the same requirements as for more conventional structures. First of all, structural safety must be guaranteed and therefore the system must be able to withstand the design loads. Secondly, the serviceability must be satisfied and therefore the system must be able to function as intended. Finally, its durability must be checked and the system must not suffer too much damage for a proper use. The design of geomembrane systems varies depending on whether the system is covered or exposed in pressurized waterways but both designs are based primarily on the experience of professionals in the field. Since the exposed systems represent the vast majority of geomembrane systems installed in pressure tunnels, it is chosen to address here only the recommendations made by (Cazzuffi et al., 2012b) for this type of technology.

The design of an exposed geomembrane system considers several components of the system, such as the geomembrane, the support layer, the perimeter joints and fastening lines and the drainage system. Each of these elements has a specific role and their design, presented briefly here, must be able to cope with the various stresses to which they are exposed. The design of the geomembrane consists in the selection of suitable material characteristics for the membrane itself and the geotextile. The role of the support layer lies mainly in the prevention of damage that could be done to the system in the case of a deterioration of the subgrade. The perimeter joints and fastening lines are used to fix the geomembrane system to the tunnel wall, and their design is intended to establish the type and number of profiles needed to properly anchor the system. Finally, the drainage system is responsible for reducing as much as possible the back pressure that could be induced by water behind the membrane in the case of an empty tunnel. In order to properly design these elements, several load cases must be studied. In particular, it is necessary to study the case of a drainage system failure where water would flow behind the geomembrane or the case of a completely waterless tunnel. The stresses induced by transient situations related to the operation of the hydropower plant must also be taken into account and in particular the phenomena of cavitation or hammering induced by the sudden opening or closing of the gates must be considered (Wiggert and Tijsseling, 2001).

2.2.4 Geometry

As described in Section 2.2.3, the geomembrane system is attached to the pressure tunnel wall by means of both longitudinal and sectional anchoring systems called fastening lines and perimeter seals respectively (Cazzuffi et al., 2012b). An application example illustrating the arrangement of these anchoring systems in relation to the membrane is proposed in Figure 14.

Figure 14: Geomembrane lining system in the US. Image: courtesy of © Carpi Tech

Both types of anchors are made from stainless steel profiles. First, the perimeter seals are installed in the section and therefore perpendicular to the flow at the beginning and end of each waterproofing section to avoid water infiltration behind the liner (Scuero and Vaschetti, 2021). In a second step, the fastening line are placed parallel to the flow and are responsible for exerting tension on the membrane in order to create a form of rigidity in the system and to prevent the apparition of wrinkles or slack areas. The tension within the membrane is thus applied mainly in section, in a plane perpendicular to the flow. Due to the arrangement of the anchors and the tension induced by them, the geometry of the membrane in section thus takes on a polygonal shape where the vertices of the polygon are embodied by the anchors that ensure contact between the membrane and the wall. This geometry is shown in Figure 15 below.
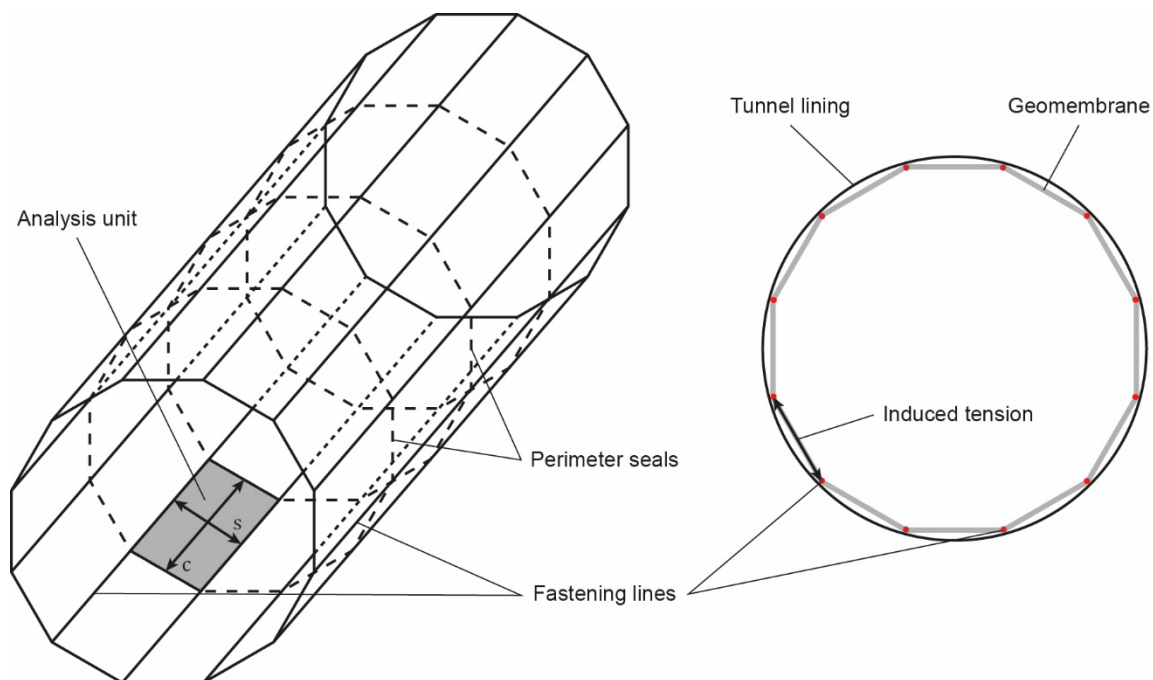
Figure 15: Schematic representation of the geometry and the anchoring system of a geomembrane system

The consequence of this geometry is that the general geomembrane system is composed of several sections of membranes with fixed supports at their ends. This type of support induces an independence of each partial membrane with respect to the others and thus the behavior of one of them is not influenced by that of the others. This is important because it allows the consideration of a single partial membrane to define the overall behavior of the system and thus greatly simplifies the geometry to be studied since it only consists of a simple rectangle as shown in Figure 16. This basic rectangle is thus attached by simple supports on its perimeter but is free to deform on the rest of its surface.
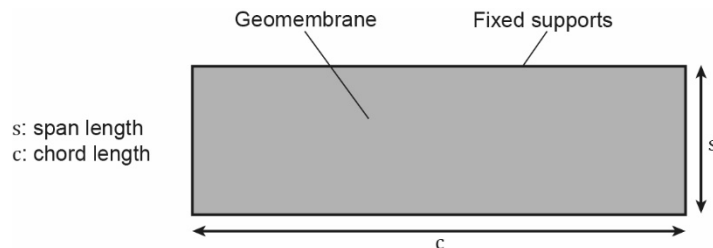
Figure 16: Format of the studied reference membrane

2.2.5 Fluid-membrane interactions

Since the membrane whose geometry is presented in Section 2.2.4 is fixed by simple supports only on its perimeter, it is free to deform within its limits and vibrate following the flow solicitation. These potential vibrations are a problem to be studied since they can cause many failures with respect to the normal operation of the geomembrane system. Indeed, it is possible that some specific flow conditions generate a membrane resonance phenomenon for which the amplitude of the vibrations induced by the flow on the membrane increases enormously. These vibrations can then quickly get out of control and have very negative effects on the operation of the hydropower plant. Excessive vibrations create obstacles to the desired one-dimensional flow of water and greatly increase the head losses, which reduces the power available to the turbines and thus the hydroelectric production. An illustration of this problem is shown in Figure 17.
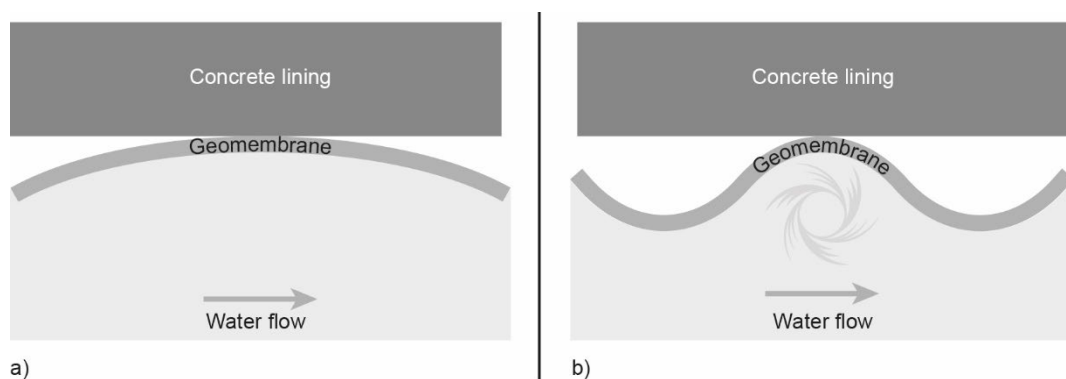
Figure 17: Schematic representation of the different possible vibration modes of the geomembrane with a) initial state and b) severe vibration state

In particularly critical cases, the resonance of the geomembrane could even lead to its rupture. The water could then infiltrate behind the geomembrane in too large a quantity to be evacuated efficiently by the drainage system and thus generate negative pressures, which corresponds to a design load case of the system but which is not a desirable situation for its durability. Pieces could also be torn from the geomembrane and carried by the flow to the turbines, which could seriously damage them.

In order to determine whether these risks are likely to occur, it is necessary to consult the literature to see if such geomembrane vibration phenomena in pressure waterways have already been studied. It quickly becomes apparent that no study directly addresses the vibration behavior of geomembrane systems subjected to pressure, which reveals real gaps in the knowledge of the behavior of geomembranes in such environments. However, the term geomembrane designating more the context of application of a membrane rather than its own characteristics, it is quite possible to make analogies between the behavior of the geomembrane and that of a membrane subjected to the action of a fluid in other fields. Indeed, many studies have been published on fluid-membrane interactions in other disciplines such as aerospace engineering, acoustic sciences or medicine. Here are some examples of publications dealing with these interactions and the main findings.

In the field of acoustics, a journal article by (Gascón-Pérez, 2017) discusses how the interactions between a fluid and a cylindrical membrane placed on a drum affect the characteristic frequency of the coupled system and are likely to change its response to a dynamic loading. In particular, an analysis of the variation of the oscillation frequency as a function of the drum size is proposed and provides an insight into the oscillatory behaviour of a membrane in the presence of fluid and gives clues for the understanding of the interactions of water with a tubular membrane.

In the same vein, another journal article by (Plaut and Cotton, 2005) studies the dynamic behaviour of geomembrane tubes inflated with air. In particular, it is shown that the weight of the tube and the force induced by the inflated air lead to a non-circular cross-sectional shape. However, this paper is not completely applicable to the case studied, since the study is conducted without any fluid outside the tubes, whereas in the pressure tunnel, there is water flowing at low velocity between the membrane and the tunnel lining.

A paper by (Tiomkin and Raveh, 2021) proposes a complete review about progress in aerospace sciences focusing on fluid-membrane interactions. Among others, it indicates that for a pre-tensioned membrane, its dynamic response to steady flow can either be a stable regime in which static membrane deformation is observed or an unstable regime in which membrane oscillations appear with clearly distinguished vibration modes and frequencies. The paper also discusses the parameters that can trigger an unstable regime: angle of attack, pretension, Reynolds number, membrane mass ratio, etc.

These few non-exhaustive examples of studies dealing with the behavior of membranes in contact with a fluid clearly show that the characteristics of the latter influence the behavior of the membrane and that a flow is likely to generate vibrations of it. However, the difficulty to find relevant papers dealing with situations similar to the one exposed in Section 2.2.4 underlines the need for a study specifically focused on the flow-induced vibrations of exposed geomembrane systems in pressure waterways.

2.3   Hyperelastic materials

The stress-strain curve of the geomembrane shows that its behavior cannot be assimilated to that of a linear elastic material and that its description requires more complex models developed for hyperelastic materials. An overview of the basics of hyperelasticity is therefore necessary in order to correctly understand the behavior of the membrane and to propose a model that approximates its real behavior as much as possible.

2.3.1 Fundamentals of hyperelasticity

It is common to try to characterize the response of a material to a load by approximating its behavior by a linear elastic model. However, this simplifying assumption of a linear relationship between stress and strain is not valid for all materials and for all ranges of deformation. Thus, more complex behavioral models had to be developed for materials whose behavior cannot be described by a linear elastic relationship. This is particularly the case for polymeric materials, frequently called rubber materials, whose intensive study (Boyce and Arruda, 2000; Mooney, 1940; Rivlin, 1948) based on a continuum mechanics approach has allowed the development of the theory of hyperelasticity.

Rubber materials usually present long chains of molecules recognized as polymers. These long chains of molecules are initially randomly oriented with weak intermolecular interactions. These properties of the network arrangement lead to a stress-strain relationship that is mainly governed by changes in the structure of the network as it becomes preferentially oriented with stretching (Boyce and Arruda, 2000). Thus, although it is possible to consider a rubber material as a linear elastic material for small deformations (Ali et al., 2010), the analysis of its behavior for large deformation requires the consideration of the large elastic deformation theory.

Linear elasticity and hyperelasticity are both reversible processes therefore for which the internal energy dissipation is zero, meaning that the work done during the loading process is fully recovered when the load is removed. The main difference is that hyperelastic materials can experience extremely large deformations and the relationship between stress and strain is highly nonlinear. Figure 18 shows the difference between the stress-strain curves for a linear elastic material and a hyperelastic material.
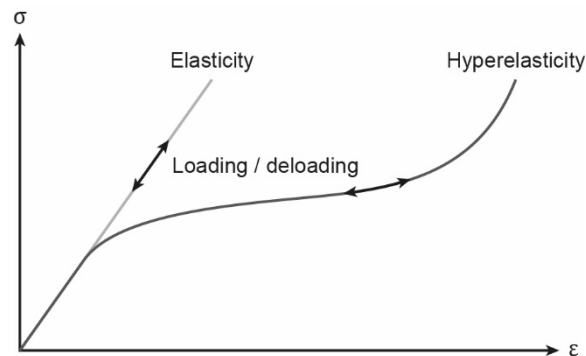
Figure 18: Qualitative difference between an elastic and hyperelastic behavior

This section aims to define the theoretical concepts from the mechanics of continuous media necessary to understand the basis on which the theory of hyperelasticity is based before presenting the most famous behavioral models derived from this theory.

2.3.2 Theoretical development

Any hyperelastic model is based on the same theoretical foundations and is built according to the same general principles. It is thus important to make an overview of the theoretical concepts on which these hyperelastic models are based and which are used to model the behavior of the membrane.

Constitutive law for hyperelastic material

The constitutive law for an isotropic hyperelastic material is expressed as a differential equation relating the stresses exerted on the material for a certain deformation through a function called energy density function. In its general form, this expression, called Cauchy equation, takes the following form:

$$\boldsymbol{\sigma} = \frac{\partial W}{\partial \boldsymbol{\varepsilon}} \qquad (2.1)$$

where W is the energy density function. This function depends on the deformation gradient $\boldsymbol{F}$, or on characteristic quantities derived from it:

$$W(\boldsymbol{F}) = \overline{U}(I_1, I_2, I_3) = \widetilde{U}(\lambda_1, \lambda_2, \lambda_3) \qquad (2.2)$$

When the Cauchy equation is expressed by directly integrating the deformation gradient, it takes the following form (Beatty, 1987):

$$\boldsymbol{\sigma} = \frac{1}{J}\frac{\partial W}{\partial \boldsymbol{F}}\boldsymbol{F}^T \qquad (2.3)$$

where $J \equiv \det(\boldsymbol{F}) > 0$ is the Jacobean determinant.

The derivation of the variables involved in this relation and their invariants is proposed below.

Deformation gradient F and invariants

The general equation describing the motion of a continuum takes the following form:

$$\boldsymbol{x} = \chi(\boldsymbol{X}, t) \qquad (2.4)$$

where $\boldsymbol{x}$ is the spatial position at time t of a material particle with the material coordinate $\boldsymbol{X}$.

The first assumption concerning the characteristics of the material considered is its homogeneity. Since the material is considered as homogeneous, its mechanical properties do not depend on the stressing point and the strain energy density function depends only on the deformation gradient $\boldsymbol{F}$ which is expressed in (Wex et al., 2015):

$$\boldsymbol{F} = \frac{\partial \boldsymbol{x}}{\partial \boldsymbol{X}} = \begin{bmatrix} \dfrac{\partial x}{\partial X} & \dfrac{\partial x}{\partial Y} & \dfrac{\partial x}{\partial Z} \\ \dfrac{\partial y}{\partial X} & \dfrac{\partial y}{\partial Y} & \dfrac{\partial y}{\partial Z} \\ \dfrac{\partial z}{\partial X} & \dfrac{\partial z}{\partial Y} & \dfrac{\partial z}{\partial Z} \end{bmatrix} \qquad (2.5)$$

As $\det(\boldsymbol{F}) > 0$, the polar decomposition theorem states that $\boldsymbol{F}$ can be uniquely decomposed as:

$$\boldsymbol{F} = \boldsymbol{R}\boldsymbol{U} = \boldsymbol{V}\boldsymbol{R} \qquad (2.6)$$

where $\boldsymbol{U}$ and $\boldsymbol{V}$ are respectively the right and left positive definite symmetric stretch tensors.

The proper orthogonal rotation tensor $\boldsymbol{R}$ represents the rotation of the eigenvectors of $\boldsymbol{U}$, $\boldsymbol{N}_i$, to the eigenvectors of $\boldsymbol{V}$, $\boldsymbol{n}_i$:

$$\boldsymbol{n}_i = \boldsymbol{R}\boldsymbol{N}_i \tag{2.7}$$

Let λ_i ($i = 1,2,3$) be eigenvalues of the stretch tensors. Those eigenvalues are the principal stretches of the deformation and often called the principal stretch ratios.

The left Cauchy-Green deformation tensor $\boldsymbol{B}$ is a measure of the strain the body experiences and is defined by (Khaniki et al., 2022):

$$\boldsymbol{B} = \boldsymbol{F}\boldsymbol{F}^T \tag{2.8}$$

where the superscript T denotes the transpose. Then V is the unique positive-definite symmetric tensor satisfying:

$$\boldsymbol{V}^2 = \boldsymbol{B} \tag{2.9}$$

The second assumption made is the isotropy of the modeled material. This means that the material possesses uniform stress-strain responses in all directions. For isotropic materials, the strain energy density function $W = W(\boldsymbol{F})$ is a function of the three invariants of the Cauchy-Green deformation tensor $W = W(I_1, I_2, I_3)$ which are defined as (Ali et al., 2010):

$$
\begin{aligned}
I_1 &= trace(\boldsymbol{B}) = \lambda_1^2 + \lambda_2^2 + \lambda_3^2 \\
I_2 &= \frac{1}{2}\left(I_1^2 - trace(\boldsymbol{B^2})\right) = \lambda_1^2\lambda_2^2 + \lambda_1^2\lambda_3^2 + \lambda_2^2\lambda_3^2 \\
I_3 &= \det(\boldsymbol{B}) = \lambda_1^2\lambda_2^2\lambda_3^2 = J^2
\end{aligned}
\tag{2.10}
$$

In the case of almost incompressible materials, it is possible to consider another set of invariants which are then more convenient to use. Most models of hyperelastic behavior are built using these invariants as shown in Section 2.3.3.

$$
\begin{aligned}
\bar{\lambda}_i &= J^{-1/3} \cdot \lambda_i \\
\overline{I_1} &= J^{-2/3}I_1 \\
\overline{I_2} &= J^{-4/3}I_1
\end{aligned}
\tag{2.11}
$$

These two sets of invariants are thus the same for an incompressible material for which the Jacobean determinant is one.

Energy density function W

Considering the three invariants presented in Equation 2.10, the energy density function then takes the following general form defined in (Ali et al., 2010):

$$W = \sum_{i+j+k=1}^{\infty} C_{ijk}(I_1 - 3)^i (I_2 - 3)^j (I_3 - 1)^k \tag{2.12}$$

In addition, several texts propose various restrictions on the deformation energy density, such as being non-negative, having a zero value in the undeformed state and being invariant under coordinate transformations (Melly et al., 2021).

If the material is considered incompressible, i.e. its volume remains constant during the deformation, then the third invariant takes the constant value $I_3 = 1$ and thus, the strain energy density function is then only a function of the first two invariants:

$$W = \sum_{i+j=1}^{\infty} C_{ij}(I_1 - 3)^i (I_2 - 3)^j \tag{2.13}$$

2.3.3 Hyperelastic models

During the last hundred years, the theory of hyperelasticity has been widely studied and a large number of papers presenting different models describing the behavior of polymeric materials have been published. These models are all based on the general Equation 2.13 presented above. This subchapter aims at presenting some of these hyperelastic models which are particularly widespread and used.

Polynomial model

The first proposed model is the polynomial model. This model is directly derived from Equation 2.13 and is formulated as follows:

$$\overline{U} = \sum_{i+j=1}^{N} C_{ij}(\overline{I}_1 - 3)^i (\overline{I}_2 - 3)^j + \sum_{i=1}^{N} \frac{1}{D_i}(J - 1)^{2i} \tag{2.14}$$

where U is the strain energy density function, which is the strain per unit of reference volume. C_{ij} are material constants that describe the shear behavior of the material. D_i is a material constant that introduces compressibility and is set equal to zero for fully incompressible parameter.

This model of strain energy function is usually used in modeling the stress-strain behavior of filled elastomers, with four to five terms.

Ogden model

This model proposes the strain energy function based on the principal stretches for incompressible materials, so for which $I_3 = 1$. The principal stretches are directly measurable quantities and it is one obvious advantage of using them (Chang et al., 1991).

Because the expression for W is derived using the stretch ratios, and not the invariants of the Cauchy deformation tensor, the Ogden model is often classified as a stretch-based model.

The relation of the Ogden strain energy density function is given by:

$$\tilde{U} = \sum_{i=1}^{N} \frac{2\mu_i}{\alpha_i^2} \left(\bar{\lambda}_1^{\alpha_i} + \bar{\lambda}_2^{\alpha_i} + \bar{\lambda}_3^{\alpha_i} \right) + \sum_{i=1}^{N} \frac{1}{D_i} (J-1)^{2i} \tag{2.15}$$

where the constants μ_i and α_i describe the shear behaviour of the material and D_i the compressibility.

The calculation of the invariant derivatives of the Ogden's energy function is more used and computationally intensive than of the polynomial form. This model can be more accurate in fitting experimental, when data from multiple experimental tests are available (Korochkina et al., 2017).

Mooney-Rivlin model

This model was formulated by Mooney and Rivlin and has a reputation for predicting the response of hyperelastic materials to a high level of accuracy, therefore, it is well known and most commonly preferred model. Such improved accuracy is a result of the inclusion of linear dependence on I_2 in the strain energy function. This means that the deviatoric response is defined by both the first and the second invariant.

$$\bar{U} = \sum_{i=0}^{N} \sum_{j=0}^{N} C_{ij} (\bar{I}_1 - 3)^i (\bar{I}_2 - 3)^j + \sum_{i=1}^{N} \frac{1}{D_i} (J-1)^{2i} \tag{2.16}$$

Neo-Hookean model

$$\bar{U} = C_{10}(\bar{I}_1 - 3) + \frac{1}{D_1} (J-1)^2 \tag{2.17}$$

The selection of which model to use depends on the application domain, the corresponding variables, and the data available to determine the material parameters (Ali et al., 2010). According to (Chagnon et al., 2004), an efficient hyperelastic model has four main qualities. First, it must be able to reproduce the curved shape of the material reaction. Secondly, a change of deformation mode must not be problematic. The model must be valid for both uniaxial tension, equibiaxial extension and pure shear. The number of fitting materials parameters of the model must also be small in order to limit the number of tests necessary to determine them. Finally, the mathematical formulation of the problem must be simple in order to allow a good numerical performance of the model. In all cases, the validity of the model must be studied and verified in order to ensure that it transcribes the real behavior of the material.

2.4 Research gaps and main objectives

It has been shown in the introduction that the use of geomembranes in pressurized flows allows to answer in an efficient way to the various challenges that hydroelectric schemes are facing today and that will only be even more important in the future. However, as the literature review has shown, there are practically no studies directly addressing the vibratory behavior of these membranes in pressurized flows. The design, dimensioning and installation of geomembrane systems are therefore based on the practical experience of a few practitioners that relies on only a few cases of application. This experimental and empirical development of this technology, ignoring its dynamic behavior, may lead to accidents and it is necessary to ensure the safe use of this technology by basing its conception on solid theoretical foundations.

In this context, it is particularly important to conduct an in-depth study of the vibratory behavior of geomembrane systems exposed to pressurized flow in order to ensure the safety and durability of this technology. The aim of this work is to contribute to the broad study of the dynamic behavior of geomembranes in pressurized flows by building a numerical model to simulate this problem, and to present the various issues and difficulties involved in its construction. This work is thus intended to be an extension of what was done by Roberto Seixas during the fall 2022 semester and to be part of the research project conducted by the Platform of Hydraulic Constructions of the EPFL (PL-LCH) on the explained problematic. In particular, this work aims to contribute by answering the following synthetic questions.

Research questions:

Which approach can be used to numerically assess the fluid-structure interactions?

How can the hyperelastic constitutive behavior of geomembrane systems be modeled and what mesh density is suitable to ensure convergence of the solution?

What are the major identified limitations and difficulties?

Chapter 3   Theoretical development

The objective of this chapter is to present the general equations governing the dynamic behavior of a geomembrane, in the case of free oscillations, but also of forced oscillations generated by a fluid flow in contact with the membrane. In order to establish the fundamental bases and to develop the intuition, a progressive approach in terms of complexity of the phenomena and equations is proposed. Also, in order to better understand the behavior of the membrane, a link with the field of structural dynamics, where the equations are simpler and their consequences more intuitive, is proposed.

3.1   Free oscillations

An oscillation is a vibration of a system in which the quantities characterizing it evolve periodically around an equilibrium position. An oscillation is said to be free when the system has been moved away from its initial state and no external energy is brought to it. The system will therefore oscillate by itself, without interaction with the environment.

3.1.1 Free oscillations for damped SDOF systems

The consideration of a single degree of freedom (SDOF) systems is particularly useful to study the basis of dynamic behavior. From a practical point of view, SDOF systems represent a radical modeling that is formally correct only for very particular structures such as some types of bridges, but they are interesting because they constitute the elementary systems for the analysis of dynamic behavior.

Damping includes phenomena that reduce the amplitude of oscillations during movement. Although its essence is much more complex, damping is usually roughly represented by viscous damping. The intensity of the corresponding force is then proportional to the speed. Damped oscillations therefore concern systems in which the vibrations gradually attenuate over time. In other words, they are simple oscillators with damping such as those shown in Figure 19.

$x(t)$:	displacement
k :	stiffness
c :	damping constant
m :	mass
$\omega_n = \sqrt{k/m}$:	circular frequency
$f_n = {\omega_n}/{2\pi}$:	natural frequency
$\xi = {c}/{2m\omega_n}$:	damping factor
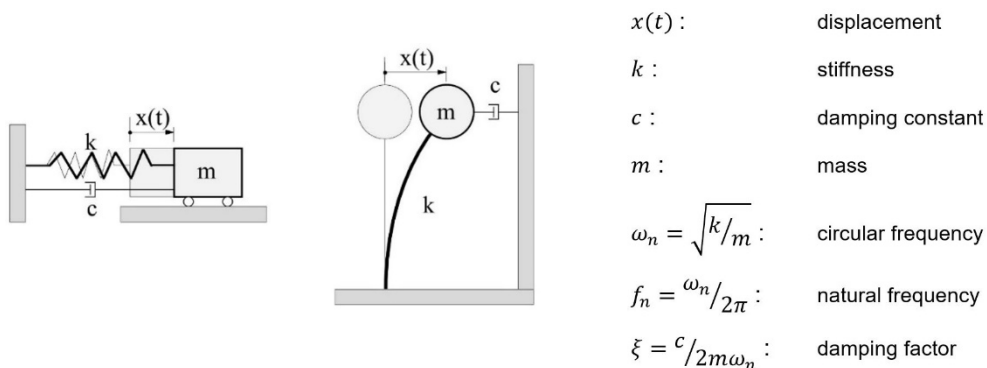
Figure 19: Simple oscillator with damping. Mechanic oriented representation, structure oriented representation and definitions (adapted from Lestuzzi and Smith, 2019)

The projection of Newton's second law along a horizontal axis allows to write:

$$\sum F = -k \cdot x - c \cdot \dot{x} = m \cdot \ddot{x} \quad \leftrightarrow \quad m \cdot \ddot{x} + c \cdot \dot{x} + k \cdot x = 0 \tag{3.1}$$

By dividing par m and considering $\omega_n = \sqrt{k/m}$, the following equation is obtained:

$$\ddot{x} + 2\xi\omega_n + \omega_n^2 \cdot x = 0 \tag{3.2}$$

The general solution of Equation 3.2 takes the following form:

$$x(t) = C_1 \cdot e^{r_1 t} + C_2 \cdot e^{r_2 t} \tag{3.3}$$

where the exponents r_1 and r_2 are equal to:

$$r_1 = -(\xi\omega_n) + \sqrt{(\xi\omega_n)^2 - \omega_n^2} \qquad\qquad r_2 = -(\xi\omega_n) - \sqrt{(\xi\omega_n)^2 - \omega_n^2} \tag{3.4}$$

Depending on the value of the parameter ξ, three different cases of damping, represented on Figure 20, must be distinguished:

- Low damping: $\xi < 1$

- Strong damping: $\xi > 1$

- Critical damping: $\xi = 1$
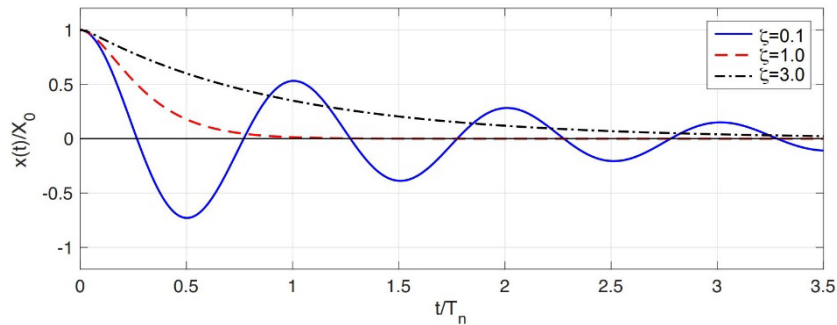
Figure 20: Types of damping (reprinted from Lestuzzi and Smith, 2019)

Since the type of damping expected in the study of the behavior of a geomembrane is a low damping, with therefore an oscillation around a position towards which the displacement converges, as shown on Figure 20, only the solution for this type of damping is proposed here.

Low damping : $\xi < 1$

In this case, the roots r_1 and r_2 are complex because the terms under the root in Equations 3.4 are negative. The general solution of Equation 3.3 thus takes the following form:

$$x(t) = e^{-\xi\omega_n t} \cdot (C \cdot \cos(\omega_D t) + D \cdot \sin(\omega_D t)) \tag{3.5}$$

with:

$$\omega_D = \sqrt{\omega_n^2 - (\xi\omega_n)^2} = \omega_n \cdot \sqrt{1 - \xi^2} \tag{3.6}$$

The determination of the constants with the boundary conditions, which is not detailed here, leads to the following expression describing the displacement as a function of time:

$$x(t) = \sqrt{X_0^2 + \left(\frac{V_0 + \xi\omega_n X_0}{\omega_D}\right)^2} \cdot e^{-\xi\omega_n t} \cdot \cos\left(\omega_D t - \tan^{-1}\left(\frac{V_0 + \xi\omega_n X_0}{\omega_D X_0}\right)\right) \tag{3.7}$$

The displacement over time corresponding to damped oscillations from an initial displacement X_0 is shown in Figure 21a.

The displacement repeats indefinitely with a pseudo-period $T_D = 2\pi/\omega_D$, but gradually attenuating according to an exponential envelope. Figure 21b shows the small lengthening of the period of the oscillations due to damping.
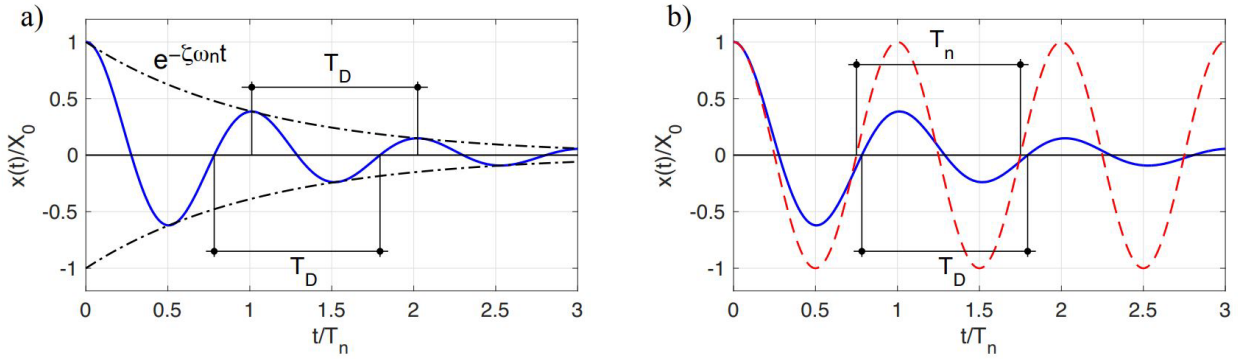
Figure 21: Free damped oscillations for SDOF system (adapted from Lestuzzi and Smith, 2019)

3.1.2 Free oscillations for a membrane

The basic theoretical concepts presented so far allow the understanding of the various phenomena governing the dynamic and vibratory behavior of a body as well as the implications of the transition to a multi-degree of freedom system on the complexity of the equations of motion and their resolution. However, the membranes diverge significantly from the systems studied until now with respect to the continuity of the body mass. Indeed, until now only bodies assimilated to systems with concentrated point masses have been considered, whereas the membrane is by definition a continuous planar body. The form of the equations governing the motion of a membrane thus differs quite a bit from what has been seen previously. The determination of these equations and the study of the oscillatory behavior of a membrane has been the subject of much work (Hettich et al., 1987; Mathieu, 1868; Troesch, 1973; Zhou-Lian et al., 2009).

The analytical development presented below is taken from (Greiner, 2010) and is valid for a rectangular membrane of dimensions a and b fixed at its boundary and subjected to a tension T as shown in Figure 22.
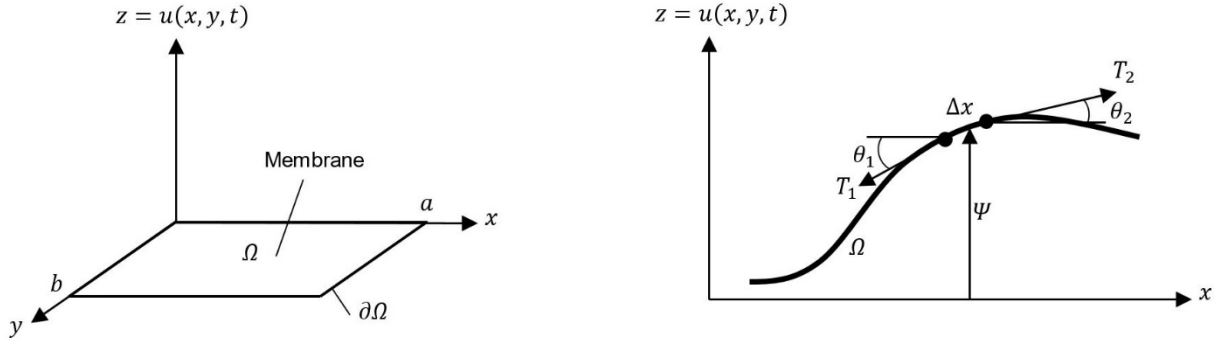
Figure 22: Schematic drawing of membrane motion and tension in case of free oscillations (adapted from Feynman, 1964; Greiner, 2010)

The figure above represents the deformation of the membrane Ω defined by its boundary $\partial\Omega$. This deformation embodied by the vertical displacement Ψ results in the surface tension T_1 with an angle to the horizontal θ_1 at a point of coordinate x and the surface tension T_2 with an angle to the horizontal θ_2 at a point of coordinate $x + \Delta x$.

In the absence of gravity and in the case of a tension T constant in time in a membrane of density ρ_m, the motion of the membrane can be described for small displacements by the linear second-order two-dimensional equation of motion (i.e. wave equation), where $\Psi(x, y, t)$ is the amplitude of the membrane's oscillation as shown on Figure 22.

$$\nabla^2\Psi - \frac{1}{v^2}\frac{\partial^2\Psi}{\partial t} = 0 \tag{3.8}$$

with $v = \sqrt{T/\rho_m}$ the wave velocity which is a real non-negative constant.

For membranes with fixed boundaries, the eigenmodes functions $\varphi(x, y)$ are such that $\Psi(x, y, t) = \varphi(x, y) \cdot e^{i\omega t}$ is the solution of the wave equation subject to uniform Dirichlet boundary conditions $\varphi(x, y) = 0$ for $(x, y) \in \partial\Omega$.

The eigenvalues then take a form such that they satisfy the Helmholtz equation:

$$\nabla^2\varphi = -\omega^2\varphi \tag{3.9}$$

The use of the superposition principle allows to obtain the non-trivial general solution of the wave Equation 3.8. After derivation, the vertical displacement $\Psi(x, y, t)$ of a rectangular membrane of size (a, b) fixed on all edges is given by (Greiner, 2010):

$$\Psi(x, y, t) = \sum_{m=1}^{\infty}\sum_{n=1}^{\infty}(A_{mn}\cos(\omega_{mn}t) + B_{mn}\sin(\omega_{mn}t))\sin\left(\frac{m\pi x}{a}\right)\sin\left(\frac{n\pi y}{b}\right) \tag{3.10}$$

where (m, n) is the eigenmodes identifier, ω_{mn} is the eigenfrequency and A_{mn} and B_{mn} are two coefficients obtained by:

$$A_{mn} = \frac{4}{ab}\int_0^a\int_0^b u(x, y, 0)\sin\left(\frac{m\pi x}{a}\right)\sin\left(\frac{n\pi y}{b}\right)dxdy \tag{3.11}$$

$$B_{mn} = \frac{4}{\omega_{mn}ab}\int_0^a\int_0^b\frac{\partial u}{\partial t}(x, y, 0)\sin\left(\frac{m\pi x}{a}\right)\sin\left(\frac{n\pi y}{b}\right)dxdy \tag{3.12}$$

The quantity ω_{mn} is defined by:

$$\omega_{mn} = v\pi \cdot \sqrt{\left(\frac{m}{a}\right)^2 + \left(\frac{n}{b}\right)^2} \tag{3.13}$$

The eigenfrequency is thus:

$$f_{mn} = \frac{\omega_{mn}}{2\pi} = \frac{v}{2} \cdot \sqrt{\left(\frac{m}{a}\right)^2 + \left(\frac{n}{b}\right)^2} \tag{3.14}$$

3.2   Forced oscillations

Oscillations are said to be forced, as opposed to free oscillations, if an external system, called an exciter, gives energy to the oscillator and imposes the frequency of its oscillations.

3.2.1 Forced oscillations for damped SDOF systems

Forced oscillations concern systems in which the vibrations are generated by an external harmonic force. They are therefore simple damped oscillators on which a periodic force is applied, like those shown in Figure 23.

$x(t)$:	displacement
k :	stiffness
c :	damping constant
m :	mass
ω :	pulsation of the harmonic force
F_0 :	amplitude of the harmonic force
$\omega_n = \sqrt{k/m}$:	circular frequency
$f_n = \omega_n/2\pi$:	natural frequency
$\xi = c/2m\omega_n$:	damping factor
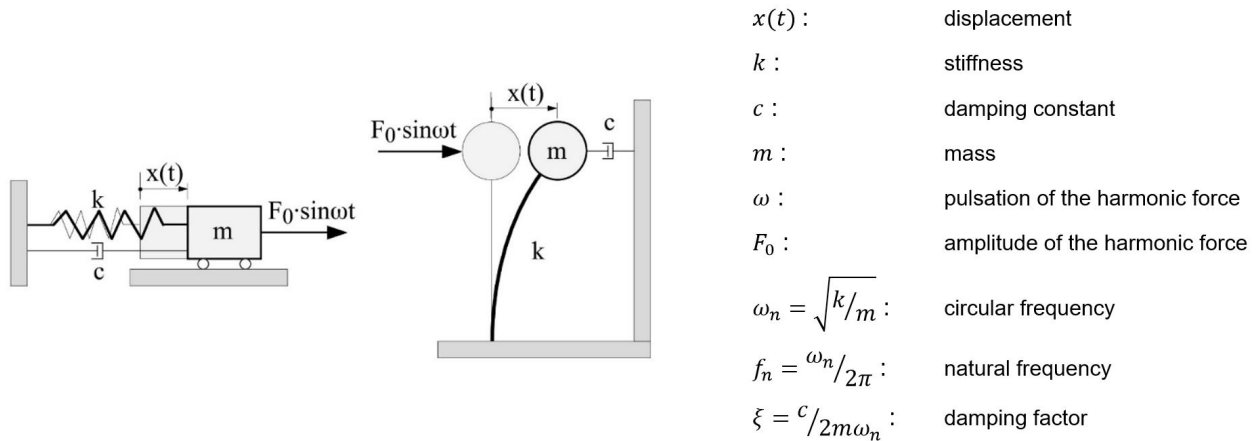
Figure 23: Simple damped oscillator subjected to a harmonic force. Mechanic oriented representation, structure oriented representation and definitions (adapted from Lestuzzi and Smith, 2019)

Following Newton's second law, the equation of motion is expressed according to Equation 3.15:

$$m \cdot \ddot{x} + c \cdot \dot{x} + k \cdot x = F_0 \cdot \sin(\omega t) \tag{3.15}$$

After division by m, the following refined expression is obtained:

$$\ddot{x} + 2\xi\omega_n \cdot \dot{x} + \omega_n^2 \cdot x = \frac{F_0}{m} \cdot \sin(\omega t) \tag{3.16}$$

A development that is not proposed here leads to the general solution indicated in Equation 3.17.

The constants C and φ_1 must still be determined with the initial conditions (generally $X_0 = 0$ and $V_0 = 0$ at $t = 0$). The complete detailed development leading to this equation can be followed in (Lestuzzi and Smith, 2019).

$$x(t) = Ce^{-\xi\omega_n t}\cos(\omega_D t - \varphi_1) + \frac{F_0/k}{\sqrt{\left(1 - \frac{\omega^2}{\omega_n^2}\right)^2 + 4\xi^2\left(\frac{\omega}{\omega_n}\right)^2}}\sin\left(\omega t - \tan^{-1}\left(\frac{2\xi\omega_n\omega}{\omega_n^2 - \omega^2}\right)\right) \tag{3.17}$$

As shown in Figure 24, the total response of the simple oscillator is composed of two sinusoids oscillating at different frequencies: a basic (equilibrium) sinusoid at the frequency of the disturbing force plus a sinusoid at the oscillator's natural frequency.
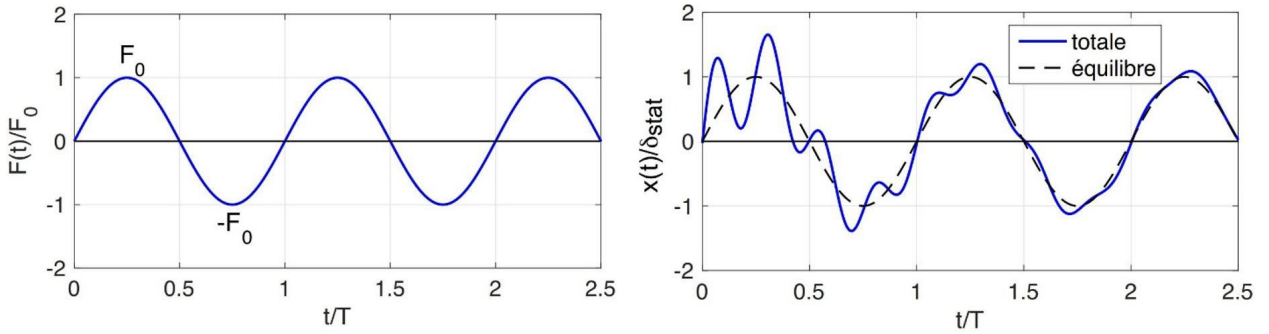
Figure 24: Forced damped oscillations for SDOF system, consisting of two sinusoids with different frequencies (adapted from Lestuzzi and Smith, 2019)

The first term of Equation 3.17 thus represents the homogeneous solution which disappears after a few damped oscillations. The second term persists indefinitely and represents the particular solution at the frequency of the disturbing force. The fraction in front of the sine corresponds to the dynamic amplification of the force F_0 if it were applied statically. The inverse of the root in the denominator represents the dynamic amplification factor R_d of the harmonic application of the force F_0 at the pulse ω:

$$R_d = \frac{1}{\sqrt{\left(1 - \frac{\omega^2}{\omega_n^2}\right)^2 + 4\cdot\xi^2\cdot\left(\frac{\omega}{\omega_n}\right)^2}} \tag{3.18}$$

As shown in Equation 3.18, without damping the R_d factor tends to infinity for an oscillation frequency equal to the natural frequency. This is the well-known phenomenon of resonance in which the displacements grow without limit. In the presence of damping, the displacements are no longer infinite and R_d is $R_d = 1/2\xi$ for $\omega/\omega_n = 1$. However, this is not the maximum value. The peak of the amplification factor appears for a slightly smaller frequency ratio, but close to one:

$$R_{d,max} = \frac{1}{2\xi\cdot\sqrt{1 - \xi^2}} \tag{3.19}$$
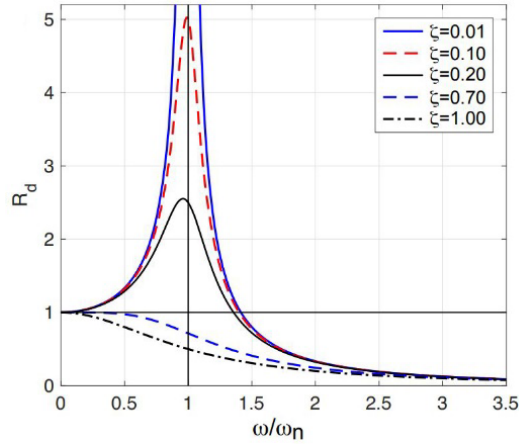
Figure 25: Dynamic amplification factor as a function of the frequency ratio (reprinted from Lestuzzi and Smith, 2019)

3.2.2 Forced oscillations for a membrane

After having seen the case of a membrane oscillating freely without energy input, it is proposed to study below the case of a membrane solicited by a fluid flow. The assumptions for the development of the equations of motion are similar to those used in the free case, namely a membrane of thickness h, fixed at its boundary, uniformly tensioned by a tension T and immersed in a flow with velocity U and fluid density ρ.

For simplicity purposes, the development of the equations is first proposed in the two-dimensional case, which corresponds to the consideration of a membrane of infinite width. The equation for the three-dimensional case is simply given at the end of the chapter.

The equation governing the dynamic behavior of the membrane is obtained in (Tiomkin and Raveh, 2021) by considering the balance of forces along the section of the membrane. For this purpose, the membrane is divided into small elements of equal size $d\xi$ as shown in Figure 26.
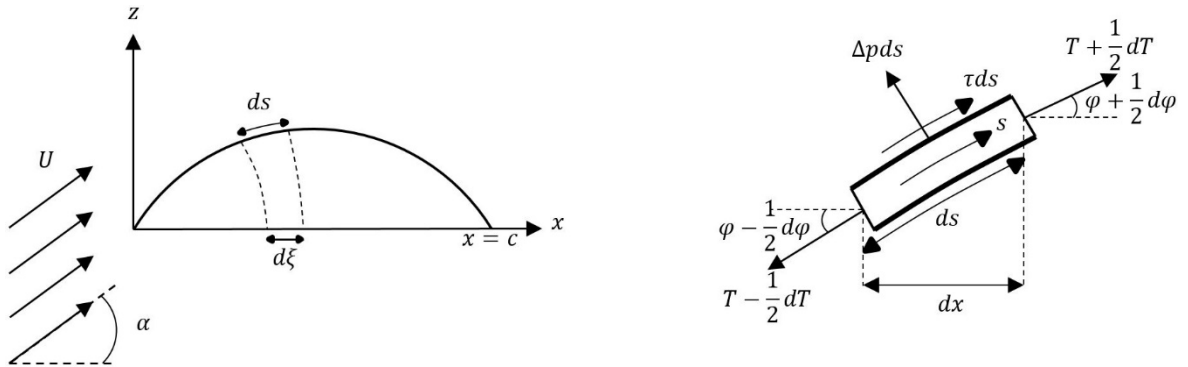
Figure 26: Schematic drawing of membrane motion and tension in case of forced oscillations induced by fluid flow (adapted from Tiomkin and Raveh, 2021)

Under dynamic loading, each element is deformed in the $x(\xi, t)$ and $y(\xi, t)$ directions while maintaining its mass per unit length of $\varphi_m h d\xi$, where φ_m is the density of the geomembrane. Thus the balance of forces in a general case of large deformations allows to write:

$$\rho_m h \frac{\partial^2 x}{\partial t^2} = \frac{\partial}{\partial \xi}(T \cos(\varphi)) - \Delta p \frac{\partial z}{\partial \xi} + \tau \frac{\partial x}{\partial \xi} \tag{3.20}$$

$$\rho_m h \frac{\partial^2 z}{\partial t^2} = \frac{\partial}{\partial \xi}(T \sin(\varphi)) + \Delta p \frac{\partial x}{\partial \xi} + \tau \frac{\partial z}{\partial \xi} \tag{3.21}$$

where $\Delta p(\xi, t)$ is the hydrodynamic load along the membrane, $\tau(\xi, t)$ is the shear stress due to viscous flow and $T(\xi, t)$ is the tension along the membrane, assumed uniform in initial state $T(\xi, 0) \equiv T_0$.

When only the vertical deformations of the membrane, i.e. those in the z direction, are considered, the x and ξ coordinate systems coincide and the nonlinear equation of the membrane is simplified.

$$\rho_m h \frac{\partial^2 z}{\partial t^2} = \frac{\partial}{\partial x}(T \sin(\varphi)) + \Delta p + \tau \frac{\partial z}{\partial x} \tag{3.22}$$

Several mathematical simplifications and in particular the consideration of the tangential equilibrium relation $T_s = -\tau$ allow to obtain the nonlinear dynamic equation for a membrane.

$$\rho_m h \frac{\partial^2 z}{\partial t^2} = T \frac{\partial^2 z}{\partial x^2} \left(1 + \frac{\partial(y^2)}{\partial x}\right)^{-3/2} + \Delta p \tag{3.23}$$

When potential flow is considered (yielding constant tension along the membrane), and small membrane deformation is assumed, a linear form of the membrane dynamic equation is introduced.

$$\rho_m h \frac{\partial^2 z}{\partial t^2} = T \frac{\partial^2 z}{\partial x^2} + \Delta p \tag{3.24}$$

in which T is constant along the membrane but can vary with time due to membrane elongation.

The formulation of the equation for the three-dimensional problem can be found in (Ormiston, 1971) and takes a form very similar to what was presented previously.

$$\rho_m h \frac{\partial^2 z}{\partial t^2} = T^x \frac{\partial^2 z}{\partial x^2} + T^y \frac{\partial^2 z}{\partial y^2} + \Delta p \tag{3.25}$$

where T^x and T^y are the tensions applied in the membrane plane, in the x and y directions

3.3 Dimensional analysis

Dimensional analysis is based on the premise that physical quantities have dimensions and that the physical laws relating these different quantities are not altered by a change in the units measuring these dimensions. This restricted field of physics is a set of rules whose goals are to propose dimensionless numbers allowing to simplify the basic equations by removing negligible terms, to reduce the number of relevant parameters necessary for the experimental study of the phenomena, to establish criteria to be respected in order to verify the representativeness of a reduced scale experiment and to provide these relations of change of scale. It is therefore particularly relevant to propose a dimensional analysis of the physical relationships presented in Section 3.2 in order to determine dimensionless numbers governing the behavior of geomembranes in a fluid flow.

3.3.1 Governing variables

The method for determining these principal dimensional numbers is based on the Vaschy-Buckingham (Buckingham's Pi) theorem. This theorem is fundamental in dimensional analysis and allows to establish how many independent dimensionless numbers can be constructed in a physical problem involving n variables. The independent variables governing the behavior of a membrane in a fluid flow and their corresponding dimensions are presented below by category.

Governing independent variables:

Fluid:
- Gravity: g $[LT^{-2}]$
- Fluid density: ρ $[ML^{-3}]$
- Dynamic fluid viscosity: μ $[ML^{-1}T^{-1}]$

Flow:
- Velocity: U $[LT^{-1}]$
- Pressure: P $[ML^{-1}T^{-2}]$

Membrane:
- Membrane density: ρ_m $[ML^{-3}]$
- Thickness: h $[L]$
- Span length: s $[L]$
- Chord lendgth: c $[L]$
- Grouped parameters of hyperelastic behaviour: C_{xx} $[ML^{-1}T^{-2}]$

The dynamic behavior of a membrane can therefore be described by $n = 10$ independent variables using $p = 3$ fundamental units. The problem is thus written in the implicit form given by the Equation 3.26.

$$\Phi(g, \rho, \mu, U, P, \rho_m, h, s, c, C_{xx}) = 0 \tag{3.26}$$

3.3.2 Addimensional numbers

The theorem of Vaschy-Buckingham then states that the solution to this problem can be represented using $k = n - r = 7$ independent dimensionless numbers, with $r = 3$ the rank of the dimensional matrix associated to the problem. Thus, instead of studying a problem of dimension $n = 10$, it is possible to reduce to a problem of dimension $k < n$ expressed in terms of dimensionless numbers as formulated in the Equation 3.27.

$$\Psi(\Pi_1, \Pi_2, \Pi_3, \Pi_4, \Pi_5, \Pi_6, \Pi_7) \tag{3.27}$$

Care should be taken to choose dimensionless numbers that have a physical meaning. Thus, in practice, it is common to try to form dimensionless numbers that are already established and widespread in order to ensure their physical meaning and to facilitate the interpretation of the values they will take. The dimensionless numbers chosen to express the problem of dynamic behavior of a membrane are presented below, again by category.

Static membrane problem:

- Aeroelastic number, (Tiomkin and Raveh, 2021):
  $\Pi_1 = Ae = \dfrac{C_{xx} \cdot h}{\frac{1}{2}\rho U^2 \cdot c}$
- Slenderness ratio:
  $\Pi_2 = \lambda = \dfrac{c}{s}$

Dynamic membrane problem:

- Mass ratio, (Tiomkin and Raveh, 2021):
  $$\Pi_3 = \omega = \frac{\rho_m \cdot h}{\rho \cdot c}$$
- Strouhal number, (Tiomkin and Raveh, 2021):
  $$\Pi_4 = St = \frac{fc}{U}$$

Fluid flow related numbers:

- Reynolds number, (Ruzicka, 2008):
  $$\Pi_5 = Re = \frac{\rho U c}{\mu}$$
- Froude number, (Hager and Castro-Orgaz, 2017):
  $$\Pi_6 = Fr = \frac{U}{\sqrt{gc}}$$
- Euler number, (Ruzicka, 2008):
  $$\Pi_7 = Eu = \frac{\Delta P}{\rho U^2}$$

The different dimensionless numbers presented above are particularly important to consider when selecting different boundary conditions for the flows being modeled to ensure that the results are sufficiently different to allow for meaningful analysis.

Chapter 4   Methodology

In order to answer the various questions posed in Section 2.4, numerical modeling using finite element software is conducted. This chapter aims at describing the approach undertaken, presenting the fundamentals of the numerical tools used and exposing the various parameters defined within the software. There are several numerical softwares allowing to model the dynamic behavior of a body submitted to a fluid solicitation but within the framework of this work, it was decided to use the American software ANSYS. This numerical modeling may be completed in the future by the creation of a physical model in the laboratory, but its development still needs to be discussed and is therefore beyond the scope of this work.

4.1   Numerical method

4.1.1 ANSYS

The numerical simulation will be performed using ANSYS v2021 R2 software. The software was originally developed by Dr. John Swanson, founder of the company ANSYS Inc. which is based in Houston, USA. It is an analysis tool for predicting the behavior of a body in its environment in a wide range of different fields. Indeed, ANSYS is composed of more than thirty modules developed by the company or bought from its competitors and allowing to treat very diverse problems, going for example from calculations in mechanics of the structures to the modeling of electromagnetic phenomena while passing by the simulation of fluid flows, this last functionality being obviously paramount within the framework of this work.

ANSYS code can be used in two different software environments: ANSYS Classic and ANSYS Workbench. The first of the above-mentioned environments is the first to have been developed by the company and allows direct use of the APDL (ANSYS Parametric Design Language) coding language. The entry of geometry, calculation parameters and the various options offered by the software is done by writing command lines in the form of code and therefore requires a good knowledge of programming to exploit its full potential.

Because of this operation, ANSYS Classic presents a graphical user interface less developed than the Workbench and is therefore more adapted to the modeling of simple geometries that can be built with basic operations. This first software environment can thus be particularly useful for cases where a repetition of calculations involving a systematic modification of variables is necessary but the environment is definitely complex to use. The numerical simulation will thus be carried out using ANSYS Workbench, which offers a more intuitive use of the tools offered by ANSYS and thus allows less experienced users to better visualize the modeling steps and the impacts of the different options chosen.

4.1.2 Two way fluid-structure interaction

The modeling of the vibratory behavior of a membrane solicited by a flow requires of course to model both the structural part, but also the part related to the flow. Since the flow acts on the behavior of the membrane but the reaction of the latter has in turn an effect on the flow, this problem is called a two way fluid-structure interaction.

Among all the modules offered by ANSYS, two modules are essential to model this problem: ANSYS Fluent and ANSYS Transient Structural Analysis. As their name may suggest, Fluent is responsible for modeling the part related to fluid flow, while Transient Structural allows modeling the transient behavior of solid structures. These two modules can be used separately to deal with problems related to one or the other of the fields of application of these modules, but their coupled use requires the addition of a module allowing their simultaneous use called System Coupling. This module allows the synchronized bilateral sharing of data from one of the modules to the other and thus the modeling of the global problem by taking into account the feedbacks of both parts. The communication between the fluid and the solid occurs in terms of forces from the fluid to the solid and in terms of displacements from the solid to the fluid (Ansys, 2021a). The general principle of how the modeling works is illustrated in Figure 27 below.
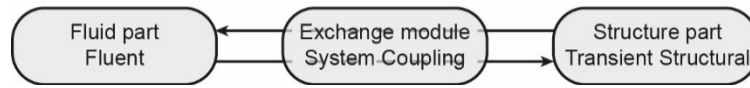
Figure 27: Representation of the modules involved in the two way fluid-structure interaction and of their relations

The fields of application of these different modules as well as the theoretical bases on which they are based are detailed in the following Sections 4.1.3, 4.1.4 and 4.1.5.

4.1.3 ANSYS Fluent

The simulation of the flow will be done using the module ANSYS Fluent. This program allows the modeling of fluid flows, turbulence, heat transfer and chemical reactions for a wide range of applications, especially in the industrial field. Its worldwide use testifies to the reliability of the results obtained from a robust and fast calculation as promoted by the brand.

The ANSYS Fluent solution method is based on the Finite Volume Method (FVM) which is a numerical technique that discretizes the differential equations governing the flow which are the conservation of mass and momentum equations (Wendt et al., 2008). In a stationary frame, these equations can be written in the form shown in Equations 4.1 and 4.2 as explained in (Ansys, 2021a).

Continuity equation:

$$\frac{\partial \rho}{\partial t} + \nabla \cdot (\rho \boldsymbol{u}) = S_m \tag{4.1}$$

where $\boldsymbol{u}$ is the overall velocity vector and the source S_m is the mass added to the continuous phase from the dispersed second phase, for example due to vaporization of liquid droplets.

Momentum equation:

$$\frac{\partial (\rho \boldsymbol{u})}{\partial t} + \nabla \cdot (\rho \boldsymbol{u} \times \boldsymbol{u}) = -\nabla p + \nabla \cdot \boldsymbol{\tau} + \rho \boldsymbol{g} \tag{4.2}$$

where p is the static pressure and $\boldsymbol{F}$ are the external body forces, for example that arise from interaction with the dispered phase. The deviatoric stress tensor $\boldsymbol{\tau}$ is given by equation 4.3.

$$\boldsymbol{\tau} = \mu \left(\nabla \boldsymbol{u} + (\nabla \boldsymbol{u})^T - \frac{2}{3} (\nabla \cdot \boldsymbol{u}) \boldsymbol{I} \right) \tag{4.3}$$

In the case where flows involving heat transfer or compressibility are considered, an additional energy conservation equation is solved. This equation is proposed in Equations 4.4, 4.5 and 4.6 that are developed in (Ansys, 2021a).

Total energy equation:

$$\frac{\partial}{\partial t}\left(\rho\left(e + \frac{u^2}{2}\right)\right) + \nabla \cdot \left(\rho u \left(H + \frac{u^2}{2}\right)\right) = \nabla \cdot \left(k_{eff}\nabla T - \sum_j H_j \boldsymbol{j_j} + \boldsymbol{\tau} \cdot \boldsymbol{u}\right) + S_h \tag{4.4}$$

where u is the velocity magnitude, k_{eff} is the effective conductivity defined as $k + k_t$ with k_t being the turbulent thermal conductivity, and $\boldsymbol{j_j}$ is the diffusion flux of species j. The term S_h includes volumetric heat sources and the heat generation rate from chemical reactions. The total enthalpy h is defined for incompressible materials in Equation 4.5.

$$H = \sum_j Y_j h_j + \frac{p_g}{\rho} \tag{4.5}$$

with Y_j being the mass fraction of species j.

The internal energy e is defined uniformly for compressible and incompressible materials in Equation 4.6.

$$e = H - \frac{p_{op} + p_g}{\rho} \tag{4.6}$$

In the above formulas, p_g and p_{op} are the gauge and operating pressure respectively. Both of these terms are derived from the pressure management of Fluent and the details of their definition are proposed in Section 4.2.6.

It may also be interesting to note that in cases where flows involve species mixing or reactions, a species conservation equation is solved, but its description is beyond the scope if this work.

Equations 4.1, 4.2 and 4.4 are specific formulations of the general transport equation describing the temporal and spatial evolution of a variable in the flow. Except for very basic applications, the transport equations 4.1, 4.2 and 4.4 are too complex to be solved analytically. In order to solve these fundamental flow equations, it is necessary to discretize them to proceed to a numerical solution. Fluent uses a control-volume-based technique to convert a general scalar transport equation to an algebraic equation that can be solved numerically. The computational domain is then divided into several sub-volumes called cells in the framework of the finite volume method. The control volume technique consists of integrating the transport equation about each cell, yielding a discrete equation that expresses the conservation law on a control-volume basis.

Discretization of the governing equations can be illustrated most easily by considering the unsteady conservation equation for transport of a scalar quantity φ. This is demonstrated by Equation 4.7 written in integral form for an arbitrary control volume V as indicated in (Ansys, 2021a).

$$\int_V \frac{\partial \rho \varphi}{\partial t} dV + \int_{\partial V} \rho \varphi \boldsymbol{u} \cdot \boldsymbol{dA} = \int_{\partial V} \Gamma \nabla \varphi \cdot \boldsymbol{dA} + \int_V S_\varphi dV \tag{4.7}$$

where $\boldsymbol{A}$ is the surface area vector and ∂V the boundaries of the arbitrary volume. The term Γ is the diffusion coefficient and S_φ is the source term of φ per unit volume.

In Equation 4.7, the first term is called the unsteady term and describes the temporal evolution of the quantity φ. The second term is the convection term, which is responsible for defining the spatial evolution of the quantity considered along a flow line while the third, the diffusion term, describes how this quantity diffuses in directions orthogonal to the flow line. Finally, the last term is the source term, which quantifies what the flow generates.

Equation 4.7 is discretized to be applied in each cell in the computational domain. The transport equation solved for each cell then takes the discrete form shown in Equation 4.8.

$$\frac{\partial \rho \varphi}{\partial t}V + \sum_{f}^{N_{faces}} \rho_f \varphi_f \boldsymbol{u}_f \cdot \boldsymbol{A}_f = \sum_{f}^{N_{faces}} \Gamma_\varphi \nabla \varphi_f \cdot \boldsymbol{A}_f + S_\varphi V \tag{4.8}$$

where N_{faces} is the number of faces enclosing the cell, φ_f is the value of φ convected through face f and $\boldsymbol{A}_f$ is the area vector of face f. The term $\rho_f \boldsymbol{u}_f \cdot \boldsymbol{A}_f$ is thus the mass flux through the face f, while $\nabla \varphi_f$ denotes the gradient of φ at face f.

In equation 4.8, the quantity φ must be evaluated at the faces of the cell, hence the notation φ_f, but this quantity is initially evaluated only at the middle of the cell. It is therefore necessary to interpolate the face level value from the center values of two neighboring cells. This interpolation is done by means of spatial discretization methods. Moreover, the first term, the unsteady term, also requires a discretization to be solved, but this time a temporal discretization involving also its discretization methods. The discretization methods for each of these two types must be selected during the design of the model on Ansys but their presentation goes beyond the scope of this work and it is possible to refer to the theoretical guide of Fluent (Ansys, 2021a) for more details.

4.1.4 ANSYS Transient Structural Analysis

The simulation of the membrane behavior will be performed using the ANSYS software called Transient Structural Analysis. As its name indicates, this software allows to model the behavior of structures whose applied load is a function of time. In the case of modeling a two way fluid-structure interaction, it is essential to use this module for the structural part, and not Static Structural Analysis, since the load on the membrane is defined by the flow and therefore varies with time.

The software integrates a calculation by finite elements method (FEM). This method, very widespread in the world of numerical modeling, consists in discretizing the linear differential equations translating at the local scale the generalized force equilibrium of an infinitesimal element.

In order to present this method, it is best to start by developing the isotropic linear elastic case. A solid body Σ surrounded by a boundary Ω is considered. In general, volume forces are applied on Σ while surface forces or displacements are imposed on Ω. The strain tensor $\boldsymbol{\varepsilon}$ can be calculated from the displacement vector $\boldsymbol{u}$ defined on Σ using Equation 4.9 (Ansys, 2023a).

$$\underline{\boldsymbol{\varepsilon}} = \frac{1}{2}(\nabla \boldsymbol{u} + (\nabla \boldsymbol{u})^T) \tag{4.9}$$

In the present context of linear isothermal and isotropic elasticity, the constitutive equation of the stresses $\boldsymbol{\sigma}$ is given by Equation 4.10.

$$\underline{\boldsymbol{\sigma}} = \frac{E}{1+v}\left(\frac{v}{1-2v}\operatorname{tr}(\underline{\boldsymbol{\varepsilon}})\underline{\boldsymbol{I}} + \underline{\boldsymbol{\varepsilon}}\right) \tag{4.10}$$

where $\boldsymbol{I}$ is the unit tensor, E the Young's modulus and v the Poisson's ratio.

The momentum equation is initially written:

$$-\rho \boldsymbol{a} + \nabla \cdot \underline{\boldsymbol{\sigma}} = 0 \tag{4.11}$$

where ρ is the density of the solid and $\boldsymbol{a}$ is the acceleration.

By introducing $\boldsymbol{\sigma}$ into the equation and substituting $\boldsymbol{\varepsilon}$ with its definition, the momentum equation is rewritten:

$$-\rho \boldsymbol{a} + \frac{E}{1+v} \nabla \cdot \left(\frac{v}{1-2v} \operatorname{tr}(\nabla \boldsymbol{u}) \underline{\boldsymbol{I}} + \frac{1}{2} (\nabla \boldsymbol{u} + (\nabla \boldsymbol{u})^T) \right) \tag{4.12}$$

Similar to what has been said about the fluid part, Equation 4.12 is too complex to be solved analytically except in very simple cases. It is then necessary to discretize the analyzed structure to proceed to a numerical solution of this equation. The analyzed structure is then decomposed into N elements connected by M points called nodes. The displacement unknowns are then defined at the level of the nodes and connected with appropriate interpolation functions ϕ_i at the level of each element. These interpolations functions as well as their first derivative are continuous for each element and have to guarantee continuity at the interface between adjacent elements. In particular, each interpolation function is such that $\phi_i = 1$ at the node i and equal to zero at the other nodes.

By omitting the acceleration term in Equation 4.12, it is possible to reformulate it in terms of interpolation functions and approximate displacement field $\tilde{u}$ to obtain a linear algebraic system of M vector equations with M vector unknowns described in the discretized Equation 4.13.

$$-\int_{\Omega} \phi_i f_{-\Omega} d\Omega + \int_{\Sigma} \frac{E}{1+v} \nabla \phi_i \cdot \left(\frac{v}{1-2v} tr(\nabla \tilde{\boldsymbol{u}}) \boldsymbol{I} + \frac{1}{2} (\nabla \tilde{\boldsymbol{u}} + (\nabla \tilde{\boldsymbol{u}})^T) \right) d\Sigma \tag{4.13}$$

where $f_{-\Omega}$ is the vector of external forces applied on the boundary Ω.

It is possible to rewrite Equation 4.13 in a simpler form that is well known to users of finite element software.

$$\underline{\boldsymbol{K}} \boldsymbol{u} = \boldsymbol{f} \tag{4.14}$$

where $\underline{\boldsymbol{K}}$ is the total stiffness matrix, $\boldsymbol{u}$ is the vector of nodal displacement unknowns and $\boldsymbol{f}$ results from the external (continuous or nodal) forces applied on the boundary of the solid body Σ.

The additivity property allows Equation 4.14 to be reduced to the level of each element to determine the local stiffness matrix, which is then assembled into a global matrix for the entire linear system. After the global stiffness matrix is established, the boundary displacement conditions are applied by removing the corresponding unknowns and equations from the system.

If a dynamic case is considered, then the system of equations proposed in Equation 4.14 becomes somewhat more complex since it then incorporates terms for the first and second derivatives of the displacement. The solved relation for a dynamic problem is presented in Equation 4.15 (Ansys, 2021a).

$$\underline{\boldsymbol{M}}\ddot{\boldsymbol{u}}(t) + \underline{\boldsymbol{C}}\dot{\boldsymbol{u}}(t) + \underline{\boldsymbol{K}}\boldsymbol{u}(t) = \boldsymbol{f}(t) \qquad (4.15)$$

where $\underline{\boldsymbol{M}}$ is the structural mass matrix, $\underline{\boldsymbol{C}}$ is the structural damping matrix and $\underline{\boldsymbol{K}}$ the stiffness matrix. The terms $\ddot{\boldsymbol{u}}(t)$, $\dot{\boldsymbol{u}}(t)$, $\boldsymbol{u}(t)$ are respectively the vectors of nodal accelerations, velocities and displacements and $\boldsymbol{f}(t)$ is the applied load vector.

In a linear structural dynamics system, the matrices are constant but the vectors are obviously a function of time.

If large displacements are expected, the assumption of a linear relationship between strain and displacement becomes invalid. The large changes in the initial geometry and the resulting geometric nonlinearity must then be incorporated into the algorithm solution. This is done by decomposing the stiffness matrix as shown in Equation 4.16.

$$\underline{\boldsymbol{K}} = \underline{\boldsymbol{K}^c} + \underline{\boldsymbol{K}^s} \qquad (4.16)$$

where $\underline{\boldsymbol{K}^c}$ is the current stiffness matrix and $\underline{\boldsymbol{K}^s}$ the stress stiffness matrix.

The current stiffness matrix is defined as:

$$\underline{\boldsymbol{K}^c} = \int \underline{\boldsymbol{B}}^T \underline{\boldsymbol{F}}\,\underline{\boldsymbol{C}}\,\underline{\boldsymbol{F}}^T \underline{\boldsymbol{B}}\,dV \qquad (4.17)$$

The stress stiffness matrix is defined as:

$$\underline{\boldsymbol{K}^s} = \int \underline{\boldsymbol{B}}^T \underline{\boldsymbol{S}}\,\underline{\boldsymbol{B}}\,dV \qquad (4.18)$$

where $\underline{\boldsymbol{B}}$ is the strain-displacement matrix, $\underline{\boldsymbol{F}}$ is the deformation gradient matrix (see Equation 2.5), $\underline{\boldsymbol{C}}$ is the constitutive matrix and $\underline{\boldsymbol{S}}$ is the second Piola-Kirchhoff stress tensor.

In order to solve numerically the semi-discrete equation of motion presented in Equation 4.15, there are again several methods allowing a direct time integration. These methods are not detailed here, but it is possible to consult the Ansys theoretical guides to see their development (Ansys, 2021a, 2023a).

4.1.5 System coupling

In addition to the modules for simulating the behavior of a body in its environment for a wide range of physics domains, there is also a component in the ANSYS Workbench that allows interdisciplinary simulations between these different domains. This tool coordinates the calculation process between the different coupling participants, which are the modules that take part in the modeling and that need data and provide it to the other modules so that each of them can carry out the simulation in the domain reserved for them. Indeed, the coupling participants are executed as independent computational processes and this mode of operation requires, as soon as the modeled problem is multidisciplinary, an inter-process communication. This communication between the different coupling participants is managed by the System Coupling Service which is the runtime component (i.e., the back end, which is responsible for heavy duty processing such as transfer of data between participants) of the System Coupling. During the resolution process, depending on the type of coupling, unidirectional or bidirectional data transfers in the form of socket communication are performed.

A data transfer is defined by a source and a destination and is able to transmit a type variable between two independent modules. Figure 28 shows how these transfers are represented in the ANSYS Workbench.
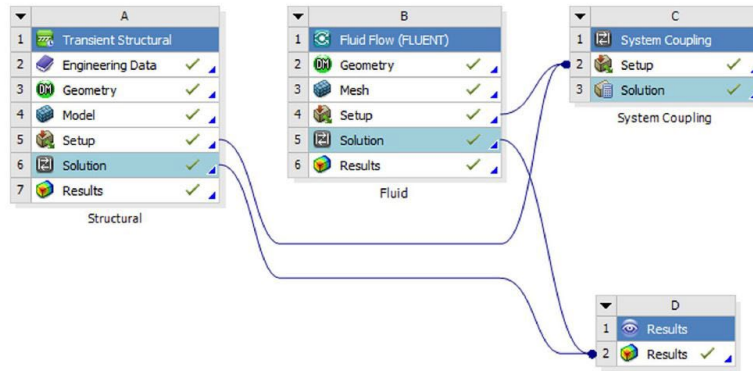

Figure 28: Snapshot from ANSYS Workbench showing a typical workflow for two-way fluid–solid interaction simulation

This communication is realized using a proprietary, light-weight, TCP/IP-based client-server infrastructure. All high level communication needed for process synchronization, brokering data transfers and managing convergence between the coupling service and participants are defined in terms of application programming interfaces (APIs) that use the low level IPC infrastructure. In a coupled analysis, the participants and the Coupling Service move forward in a synchronized manner. A high level of synchronization is achieved by using synchronization points. The five primary synchronization points correspond to key steps in the coupled analysis and consist of Initial Synchronization, Analysis Initialization, Solution, Check Convergence and Shutdown. Each of these synchronization points consists of a kind of gateway that prevents a participant from moving forward until all others have also reached that synchronization point. Between these primary synchronization points, a low level of synchronization is achieved using a token-based protocol. These different synchronization points are shown in Figure 29.
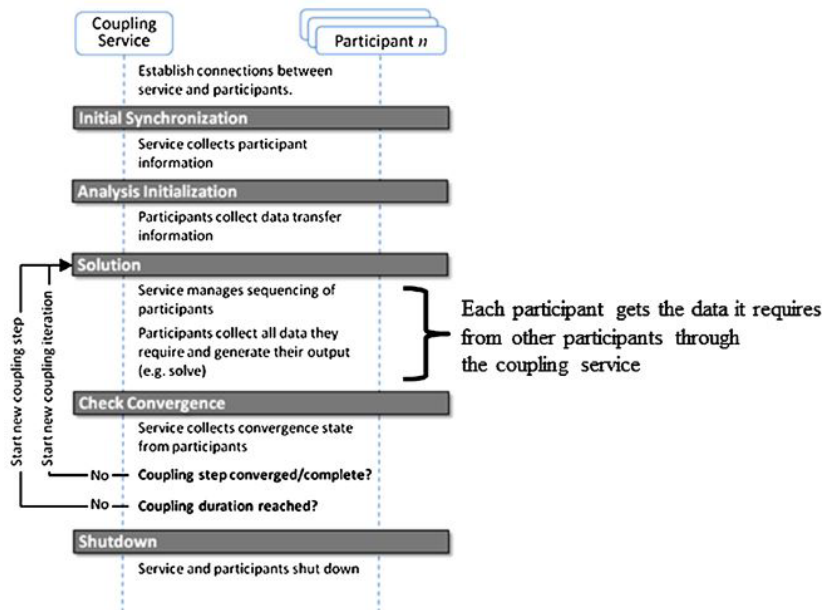

Figure 29: Execution sequence diagram for the System Coupling service and co-simulation participants (reprinted from Chimakurthi et al., 2018)

4.2 Numerical setup

4.2.1 General approach

The realization of a numerical modeling as complex and advanced as the one realized in this work requires the consideration of many distinct elements specific to a particular part of the modeling. The diagram presented in Figure 30 identifies the different steps to perform the calculation of the fluid-structure interaction. The arrows indicate the logical succession of these different steps.
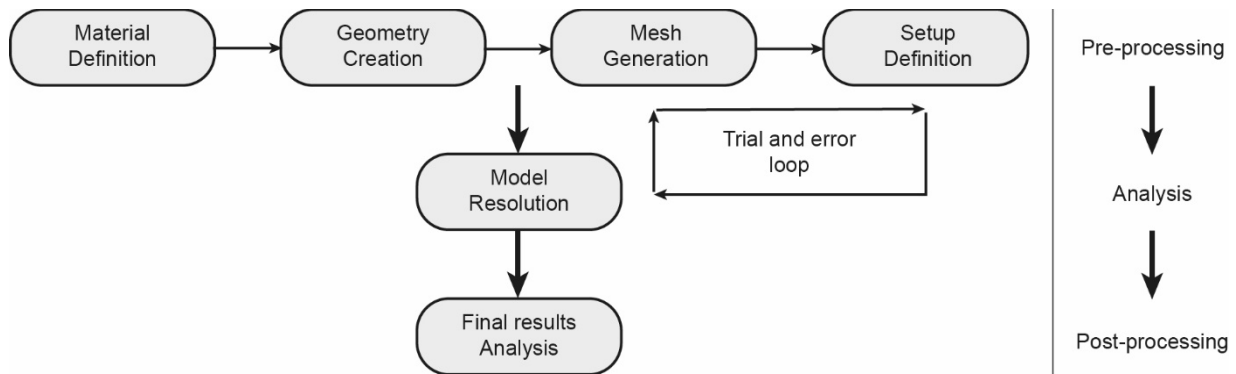

Figure 30: Representation of the general approach for the numerical setup

The first major part, called pre-processing, consists in building the model. The choices made in this part have a direct impact on the functioning of the model as well as on the reliability and accuracy of the results obtained afterwards. It is therefore essential to make documented choices while being aware of the pros and cons of the parameters proposed by the software.

It's important to mention at this point that the model is built without taking into account the effect of gravity on the membrane and on the water masses. Only the hydrostatic pressure due to the water column, as detailed in Section 4.2.7. Indeed, it turns out that the effects of gravity are negligible compared to those of pressure and flow velocity.

Once the model is built, the analysis phase consists in the calculation by the computer of the physical quantities governed by the parameters and methods defined in the pre-processing. Obviously, a lot of back and forth between this phase and the previous one is necessary in order to build a satisfactory model. It is also in this part that the systematic testing is performed.

Finally, the results analysis phase aims to draw conclusions from the calculations made. If everything went well, these results should allow us to answer the research questions posed in Section 2.4.

These different steps are realized with the following modules:

1. Material definition: Engineering Data

2. Geometry creation: SpaceClaim

3. Mesh generation: Fluent and Transient Structural Meshing

4. Setup definition: Fluent and Transient Structural

5. Model resolution: System coupling

6. Final results analysis: CFD-Post and Transient Structural

The next sections aim to detail the issues related to each of these pre-processing phases of the realization of numerical modeling as well as to detail the possible problems encountered and the choices made.

4.2.2 Material definition

The first element to be defined in the construction of the model is the material used for the membrane. As discussed in Sections 2.1.1 and 2.1.2, the geomembrane system is composed of a PVC-P membrane reinforced with a polypropylene geotextile. Also, although there is a database containing a large amount of pre-defined materials in the Ansys EngineeringData module, it was decided to try to model the behavior of the system encountered in practice as best as possible and thus to completely define a new material in EngineeringData. For this purpose, it was decided to model a geomembrane system from the company CarpiTech.

The company CarpiTech is based in the south of Ticino, in the city of Chiasso, and was founded in 1963. Since the 1970s, it has become a specialist in waterproofing hydraulic structures using a synthetic geomembrane system known as SIBELON ©. It is the CNT4400 variation of this geomembrane system that is modeled in this work. In this variation, the membrane has a thickness of 3mm and is reinforced by a geotextile weighing 500g/m^2. The stress-strain curve for this system for a uniaxial tension test was provided by CarpiTech and is shown in its entirety in Figure 31.
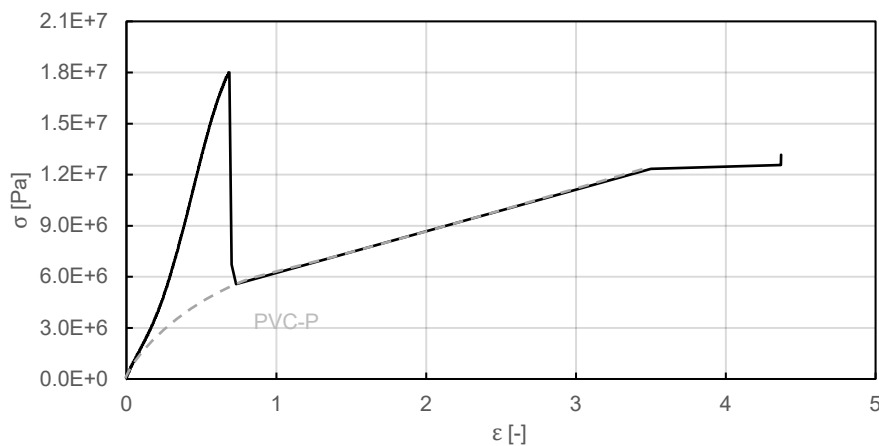

Figure 31: Total stress-strain curve for the SIBELON© CNT 4400 geomembrane system resulting from a uniaxial tension test

The stress-strain curve of the SIBELON© CNT4400 system presented above shows two distinct parts in the behavior of this system. The first part, from zero stress up to a stress of 1.8·10^7 Pa for an equivalent strain of 68%, shows a relatively high equivalent stiffness indicating that the system is working cohesively and that the geotextile is largely resisting the load applied to it. On the other hand, at this stress level, the system delaminates and the geotextile becomes uncoupled from the membrane, which then takes up the load independently, which explains why the system follows a different stress-strain curve corresponding to that of the PVC-P shown in dotted line in Figure 31.

Since this delamination process should not occur in practice, only the first part of the curve up to the delamination of the geotextile is considered in this work. Furthermore, when viewed in detail, the curve in Figure 31 shows a stepwise progression. This is due to the manner in which the uniaxial tension test was conducted. During the test, the tension was increased in steps and a certain amount of time is left for the system to deform before the tension is increased again. Also, in order to use this curve in the modeling software, it is necessary to smooth it.

This is done by connecting the points located in the middle of each stress level to obtain a smoothed curve. The result of the smoothing of the first part of the stress-strain curve is presented in Figure 32.
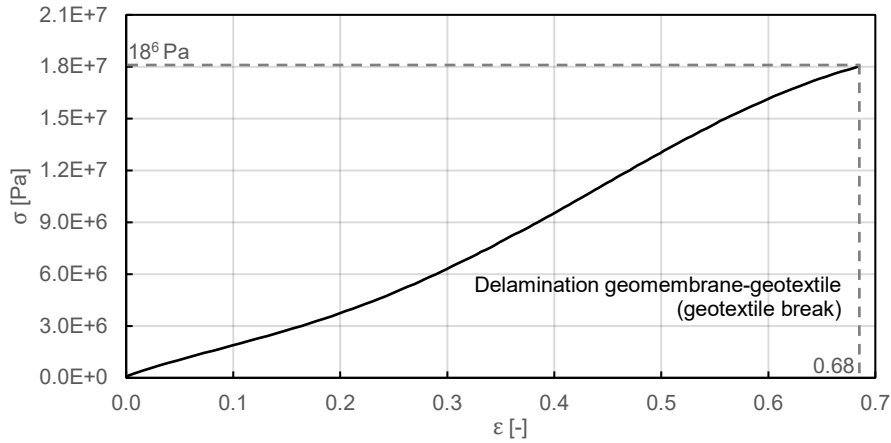

Figure 32: Smoothed partial stress-strain curve of the SIBELON© CNT 4400 geomembrane system until delamination of geomembrane and geotextile

Focusing on this first part of the stress-strain curve makes it possible to realize that the stress-strain relationship of the system is not linear. This non-linearity is one of the main characteristics of hyperelastic materials whose main properties are presented in Section 2.3. The modeling of the behavior of these hyperelastic materials requires the use of hyperelastic models whose main ones are presented in Section 2.3.3. In this work, it is chosen to use the Mooney-Rivlin model whose constitutive equation is recalled in Equation 4.19.

$$U = \sum_{i=0}^{N} \sum_{j=0}^{N} C_{ij} (\bar{I}_1 - 3)^i (\bar{I}_2 - 3)^j + \sum_{i=1}^{N} \frac{1}{D_i} (J - 1)^{2i} \tag{4.19}$$

The C_{ij} parameters of the model are automatically calculated by EngineeringData once the curve shown in Figure 32 is entered into the module. As the geomembrane system is considered incompressible, the term on the right hand side relating to the compressibility of the material becomes zero. The degree N of the model can be chosen by the user. A good compromise between model simplicity and data representativeness must be found. In this perspective, a comparison between the fit for a two and five parameters model is proposed in Figure 33.
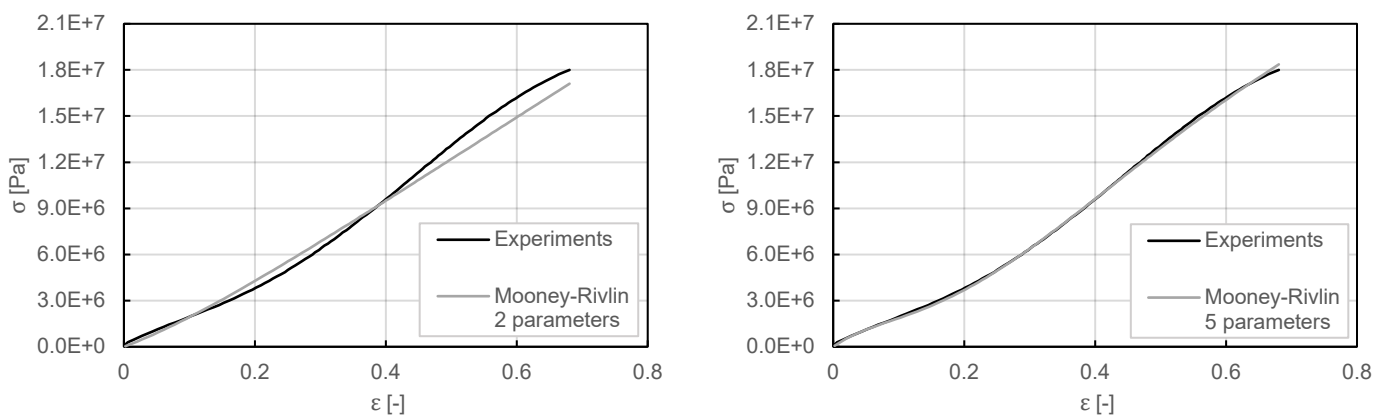

Figure 33: Stress-strain curves for the a) two and b) five parameters Mooney-Rivlin model fit for uniaxial tension test of the SIBELON© CNT 4400 geomembrane system

Figure 33 shows that consideration of a five-parameter model is both necessary and sufficient to obtain a good approximation of the data. Therefore, a five-parameter Mooney-Rivlin model is chosen to represent the behavior of the geomembrane system. The parameters of this model calculated by EngineeringData are presented in Table 2.

Table 2: Materials parameters for the Mooney-Rivlin model

Material parameter	Value [MPa]
C_{10}	-29.37
C_{01}	34.48
C_{11}	-77.96
C_{20}	20.70
C_{02}	89.99

The last material parameter to be defined is the material density. This is assumed to be equal to that of PVC-P and is therefore defined as: $\rho_m = 1400 \ \mathrm{kg/m^3}$ (British Plastics Federation, 2023).

4.2.3 Geometry

The considerations made in Section 2.2.4 concerning the geometry of the geomembrane system conclude in the possibility of defining the general behavior of this system by considering only a section of membrane. This observation allows us to significantly simplify the geometry of the model to be developed to conduct simulations on a thin planar volume immersed in the flow.

The geometry is built in the ANSYS SpaceClaim module and is shared by both Fluent and Transient Structural, each of which handles its own part of the geometry. The geometry consists of a parallelepiped with a length of 1000mm and constant cross-sectional characteristics. The section consists of a rectangle of 405mm high and 300mm wide in the center of which is a horizontal membrane of 5mm thickness extending over the entire parallelepiped. The membrane is maintained on its perimeter by means of simple supports. The displacement of the membrane at the level of these attachment points is therefore imposed as zero. Figure 34 represents the different geometrical characteristics of the model geometry.
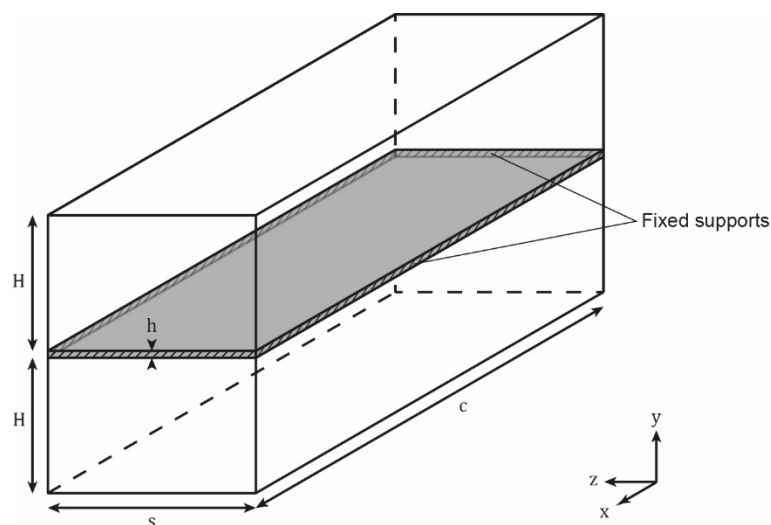

Figure 34: Schematic representation of the modeled geometry and its main dimensions

Table 3 presents the values of the main dimensions that define the geometry.

Table 3: Parameters of the modeled geometry

Dimension	Designation	Value [mm]
Span length	s	1000
Chord length	c	300
Membrane thickness	h	5
Water height	H	200

The arrangement of the membrane separates the parallelepiped into two separate volumes. The volume above the membrane is intended to simulate the main flow occurring within a hydro tunnel. The pressure and velocity imposed on this volume will therefore be higher than those imposed on the volume below the membrane, which simulates the residual flow that may occur outside the geomembrane system due to imperfect impermeability. Details about the boundary conditions and the different values they take for systematic testing are presented in Section 4.2.6.

4.2.4 Meshes

The methods presented in Sections 4.1.3 and 4.1.4 require spatial discretization of the constituent differential equations. The consideration of a larger number of discretization elements and therefore of smaller dimensions allows the results of these equations to be averaged over smaller portions of space and thus to obtain a final result that better reflects the actual behavior of the system. It is therefore generally accepted that the choice of a fine mesh leads to a better accuracy of results. However, a finer mesh also induces long computation times since the number of elements and nodes to be considered is thus multiplied. It is therefore necessary to strike a balance between accuracy of results and speed of calculation.

The meshing of the fluid domain and the structural domain is done separately on the modules Fluent and Transient Structural respectively. The characteristics of these two meshes are presented below.

Mesh of the fluid domain, Fluent.

The fluid domain is meshed using quadrilateral prism cells, also known as hexahedrons. Figure 35 below shows the configuration of one of these hexahedrons (Ansys, 2021b).
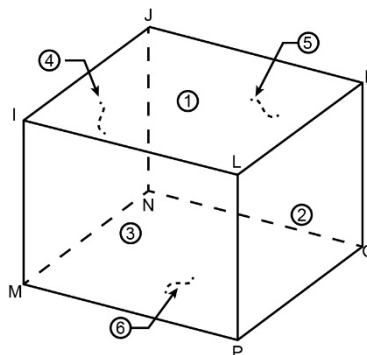

Figure 35: Hexahedron meshing cell constituting the fluid domain

The cell shown in Figure 35 thus comprises 6 faces, for which the parameters value determined at the center of the cell must be extrapolated using numerical methods, as well as 8 nodes, although these are less important than for a finite element method (see Section 4.1.3). The complete mesh layout is shown in Figure 36. The hexahedrons making up the fluid domain are easily recognizable.
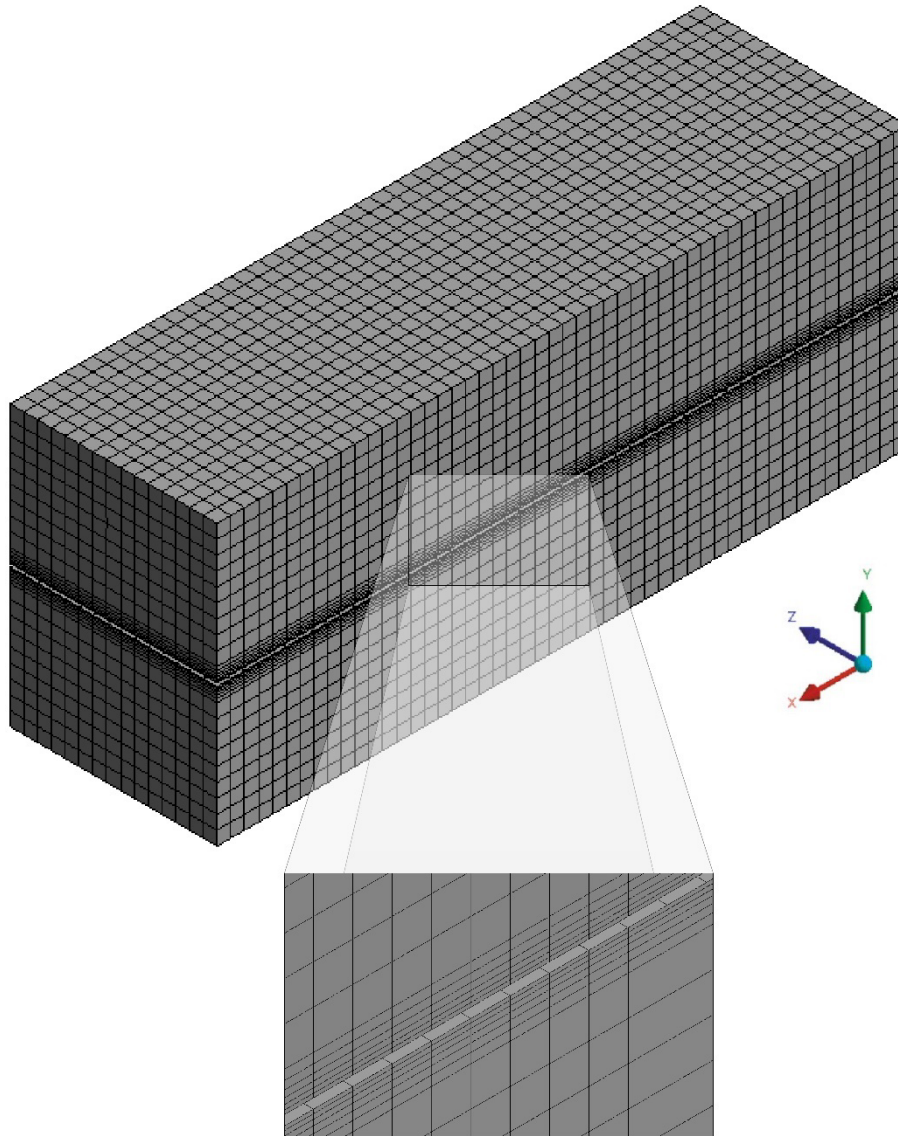

Figure 36: View of the general mesh of the fluid domain as well as the inflations installed close to the membrane faces

As explained in Section 2.4, the aim of this work is to study the behavior of a membrane stressed by the flow. This is why it is justified to set up a relatively coarse mesh far from the membrane, as the flow occurring in this zone has little impact on the membrane. Indeed, as the model geometry is uniform along its entire length, flow lines away from the membrane should be relatively parallel to the walls and therefore effectively have little impact on the behavior of the membrane.

However, it is particularly relevant to seek to refine the mesh in the zone in direct proximity to the membrane, since the flow occurring in this zone has a direct impact on the behavior of the membrane. For this reason, an inflation has been implemented close to the fluid domain boundaries in contact with the membrane faces.

Table 4 summarizes some of the main characteristics of the mesh used for the fluid domain.

Table 4: Main characteristics of the mesh of the fluid domain

Parameter	Detail	Value
Number of cells	-	22'500 [-]
Number of nodes	-	26'112 [-]
Body sizing	-	20 [mm]
Average aspect ratio	-	3.24 [-]
Maximum aspect ratio	-	9.96 [-]
Inflation	Number of layers	6 [-]
	Growth rate	1.2 [-]
	Maximum thickness	20 [mm]

A few explanations of the terms in Table 4 may be in required. Body sizing defines the maximum size a cell is allowed to be. It therefore sets an upper limit, but allows cells to be smaller, as in the case of inflation. The aspect ratio is the ratio between the largest and smallest principal dimension of a cell. It therefore gives an idea of the initial distortion of a cell, and should ideally be as close to unity as possible. For the inflation, the number of layers of inflation defines the number of cell rows on which inflation takes place. The growth rate is the ratio of progressive decrease in cell size, and the maximum thickness corresponds to the maximum extent of the inflation.

Mesh of the structural part, Transient Structural

While meshing the fluid domain was rather conventional and posed little difficulty, meshing the structural domain is particularly critical and tricky. Indeed, the accuracy and representativeness of the results depend directly on the quality of the membrane mesh. In addition to the direct influence of the mesh, the latter is subject to significant stresses.

Firstly, as the membrane is made of a hyperelastic material, the expected deformations are very high relative to the membrane's dimensions. This means that the elements making up the membrane are likely to be highly deformed, leading to a problem of distortion of the mesh elements. This problem of mesh element distortion is one frequently encountered when modeling hyperelastic materials and occurs when the elements are too distorted for the nodal coordinates of the elements to correspond to the natural coordinates of space. The software then generates an error message preventing the solver from proceeding further.
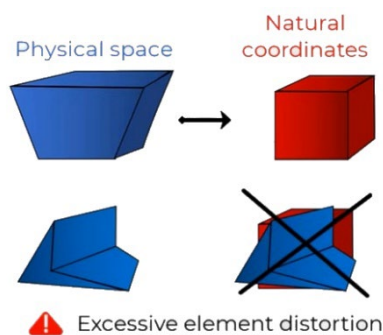

Figure 37: Element distortion error principle (reprinted from Ansys Learning, 2020)

Then there's a difficulty related to the membrane dimensions. The third dimension of the membrane, its thickness, is by definition smaller than the first two dimensions. This means that in order to have elements whose aspect ratio is close to unity, their size must be of the order of the membrane's thickness, i.e. very small, which generates a large number of elements and therefore a very high computational cost. This difficulty can theoretically be overcome by using planar elements with a constant virtual thickness, known as shell elements, which allow the thickness of the membrane to be ignored in the mesh. However, after the analysis detailed in Section 4.2.7, it was found that these elements are more exposed to the distortion problems described above than conventional solid elements. Their use was therefore abandoned and the structural domain was composed of a large number of conventional solid elements.

The technical literature proposed by Ansys indicates a series of mesh parameters to enable the mesh to better resist large deformations (Ansys Learning, 2020). In particular, the literature recommends choosing a linear-order element type. Indeed, linear elements tend to withstand large deformations better, and are less prone to distortion problems. For this reason, the mesh was created using tetrahedral elements called SOLID285. A schematic representation of one of these elements is shown in Figure 38.
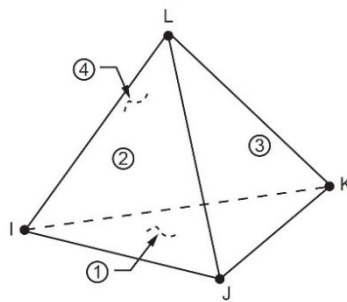

Figure 38: SOLID285 meshing element constituting the structural domain, reprinted from (Ansys, 2023b)

The element chosen to form the structural domain, shown in Figure 38, is a 3D element and has 4 faces and 4 nodes, each of which has three degrees of freedom corresponding to displacement in the three main directions of the space. The element is suitable for modeling irregular meshes and can support large deflection and hyperelasticity (Ansys, 2023b).

The complete mesh layout is shown in Figure 39. The first observation that can be made from the general mesh is that the elements of the structural mesh are much smaller than the cells that make up the fluid domain. This is due to the various issues presented above, namely that the mesh of the structural domain is directly responsible for modeling the membrane behavior, so a finer resolution is desirable, but above all that it is necessary to have small elements in order to obtain a rational appearance that is close to unity.

In addition, it is possible to notice that the elements are smaller near the edge of the membrane. This is due to the implementation of a refinement of the mesh at the edges of the membrane. Indeed, it was shown in Roberto Seixas' work, and confirmed in this one, that membrane displacements are concentrated in this zone. It is therefore desirable to have a finer resolution here, firstly to improve the accuracy of the results, but above all to avoid as far as possible the famous distortion problems by decomposing the displacement onto smaller elements.
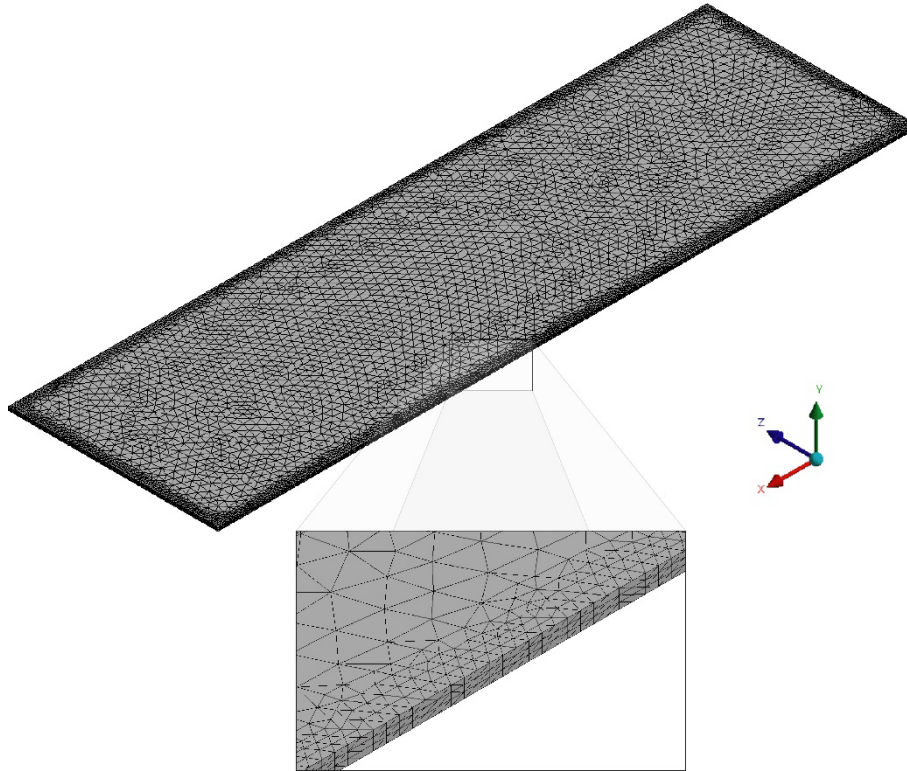
Figure 39: View of the general mesh of the structural domain as well as the refinement installed near the edges of the membrane

Given the central role played by the solid domain mesh in the results obtained by the model, it is necessary to determine the parameters to be used to define this mesh by carrying out a mesh sensitivity analysis. The aim of this sensitivity analysis is to test several different meshes for the solid domain in order to determine the level of mesh density required for acceptable convergence of the results. To this end, ten different meshes were selected, differing from each other only in the body sizing parameter. In order to compare the results provided by each of these meshes, it was decided to calculate the out-of-plane deformation of the membrane evaluated by the Transient Structural module, thus avoiding the need to perform a two-way fluid structure interaction using system coupling, and saving a considerable amount of calculation time.

This out-of-plane deformation is evaluated at the end of the total simulation time, during which the membrane is subjected to a linear pressure increase from 0bar at T=0s to 1bar at T=1s with 100 substeps. The reason for this choice of a gradual pressure increase is given in Section 4.2.7. It is also important to note that for each of these meshes, the refinement shown in Figure 39 remains applied around the perimeter of the membrane with a degree of refinement of 2. The conservation of refinement avoids the appearance of element distortion problems near the edges discussed earlier.

Table 5 summarizes the various parameter values used to generate the mesh and the resulting mesh characteristics. The computation time required to obtain the results is also indicated, to reflect the influence of the mesh's number of degrees of freedom on computational costs. The number of degrees of freedom (DoF) of the mesh is simply obtained by multiplying the number of nodes by the number of degrees of freedom of each node, i.e. 3 for the SOLID285 element.

Table 5: List of test of the mesh sensitivity analysis

Designation	Body sizing [mm]	Number of DoF [-]	Out-of-plane deformation [mm]	Computation time [s]
M1	32.0	21'426	46.606	101
M2	31.0	21'930	45.112	105
M3	28.0	22'209	52.933	106
M4	21.5	23'655	53.705	110
M5	20.0	24'360	56.135	113
M6	15.0	36'825	56.693	200
M7	10.0	55'953	56.757	312
M8	8.0	80'058	56.851	418
M9	6.0	124'020	56.935	632
M10	5.0	189'984	57.050	1079

Figure 40 represents the out-of-plane deformation as a function of the number of degrees of freedom (DoF) with a logarithmic scale for the x-axis.
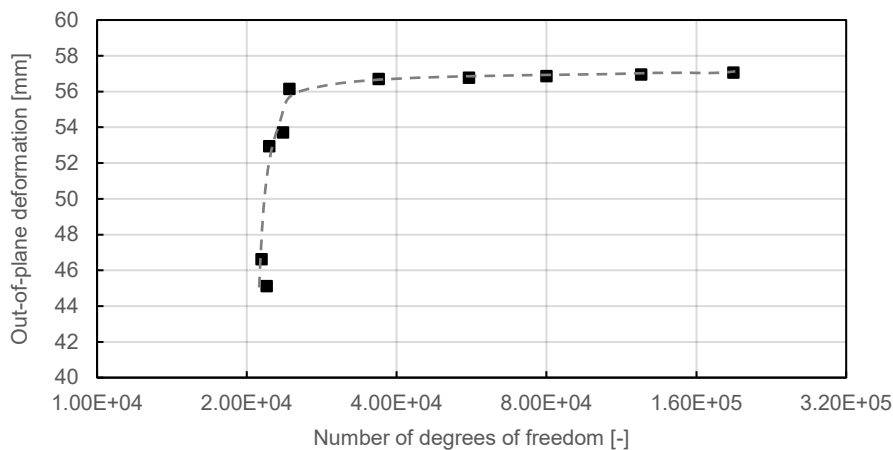
Figure 40: Out-of-plane deformation as a function of the number of degrees of freedom and the resulting hand-drawn trend curve

This representation shows that for a relatively coarse mesh, the results obtained are unstable and vary considerably, with variations of over 10% between two successive tests. But for numbers of degrees of freedom above around 25,000, the results converge towards a horizontal asymptote, meaning that the model has reached its accuracy threshold.

Figure 41 shows the calculation time as a function of the number of degrees of freedom. The axes both have a logarithmic scale, but with the same base, which means that the trend line visible on the graph does indeed transcribe a linear dependency between the number of mesh degrees of freedom and the calculation time required.
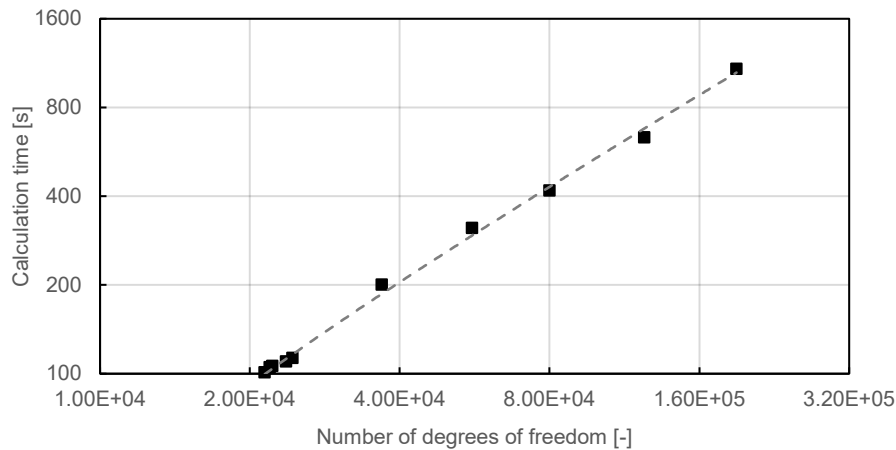
Figure 41: Calculation time as a function of the number of degrees of freedom and the resulting linear trend curve

The two graphs shown in Figures 40 and 41 give a clearer idea of the consequences of choosing one mesh rather than another, both in terms of the accuracy of the result obtained, and also in terms of the computation time required to achieve it. In view of these two trends, the M7 mesh, which offers a good compromise between calculation time and accuracy of results, is selected as the mesh for the structural domain of the model.

Table 6 summarizes some of the main characteristics of the mesh used for the structural domain.

Table 6: Main characteristics of the mesh of the structural domain

Parameter	Detail	Value
Number of elements	-	68'588 [-]
Number of nodes	-	18'651 [-]
Body sizing	-	10 [mm]
Average aspect ratio	-	2.44 [-]
Maximum aspect ratio	-	12.98 [-]
Refinement	Degree of refinement	2

4.2.5 Time discretization

In addition to the spatial discretization embodied by the mesh, the constitutive equations presented in Sections 4.1.3 and 4.1.4 require a temporal discretization. Furthermore, since the solution can obviously only be calculated over a limited period of time, a simulation time must be defined.

The simulation time corresponds to the time interval within which the problem solution is evaluated. The calculation of the solution is performed by evaluating the solution at discrete points in time called steps that are separated by a temporal interval called time step that is defined as constant in this work. Similar to what has been said about the mesh, it is obvious that small time steps lead to a more frequent evaluation of the solution and thus to a better approximation of the real behavior of the membrane but have a higher computational cost and thus generate a longer computation time. It is therefore once again necessary to find a balance between the precision and reliability of the results and the time required to calculate them.

Moreover, in order to ensure the good convergence of the solution, the progress of the calculation between two time steps is done by iterations. The number of iterations can vary locally according to the needs of the calculation, but it is possible to define limits for this number. A schematic illustration of the general operation of the time discretization is proposed in Figure 42.
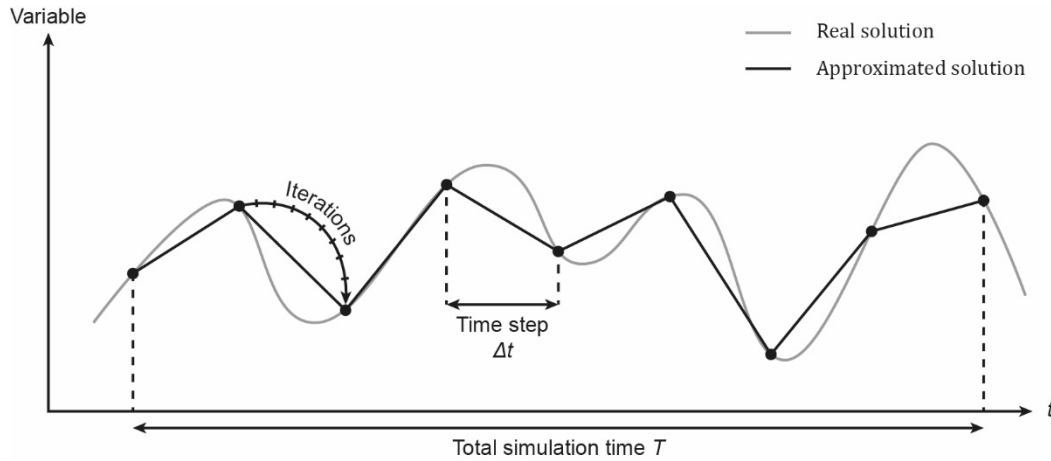

Figure 42: Illustration of the general operation of the time discretization

It has been shown experimentally in the work of Roberto Seixas that the first natural frequencies of a membrane of the same size as the one studied in this work, are between 10 and 15 Hz. This means that in order to capture any vibrations close to a resonant frequency, a time step of at most 0.05s is required to capture the two extrema of the deformation occurring during a period of oscillation. However, an even finer time step of the order of 0.01s is desirable in order to best assess the amplitude of any vibrations.

An additional constraint is linked to the gradual increase in pressure presented in Section 4.2.7. The time step size must be small enough to ensure that the pressure increment does not distort the solid mesh elements. Details of this constraint are given in Section 4.2.7, but in general, an upper bound on the ratio between time step and total simulation time is required to avoid distortion problems.

The values assumed by the various time-discretization parameters may vary from one test to another, depending on the objective of each test, and are presented in Section 4.2.10. Table 7 below shows the constant characteristics for each test.

Table 7: Parameters of the time discretization

Parameter	Designation	Value
Total simulation time	T	-
Time step size	Δt	$T/100$
Minimum number of iterations	n_{min}	1
Maximum number of iterations	n_{max}	10

These parameters are applied for the entire coupling system. This means that both the modeling of the structural part and the fluid part are done with these same parameters. This correspondence is essential for the synchronization of the two modules allowing the exchange of data (Ansys, 2023c).

4.2.6 Boundary conditions

In addition to the spatial and temporal discretization, the resolution of the governing equations presented in Sections 4.1.3 and 4.1.4 need to be closed by introducing boundary conditions.

The boundary conditions for the structural domain are very simple, consisting simply of the fixed supports around the perimeter of the membrane as shown in Figure 34.

The boundary conditions of the fluid domain are applied on each of the different faces composing the geometry presented in Section 4.2.3. Figure 43 shows the names of the different boundary conditions governing the flow.
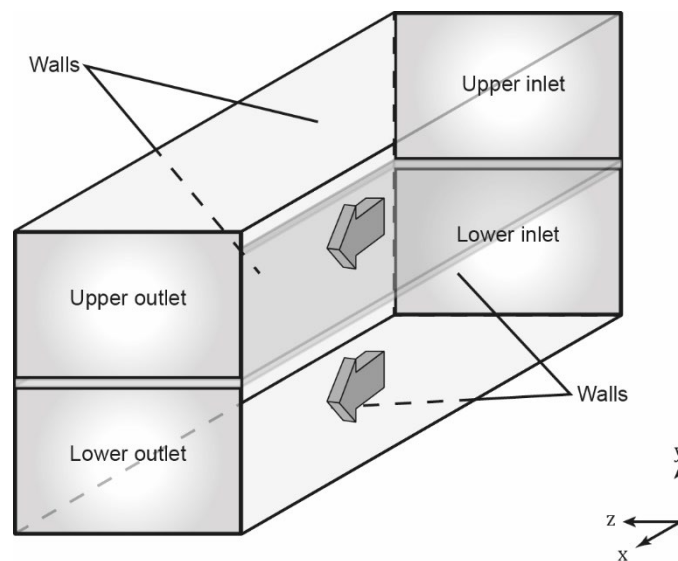
Figure 43: Location and naming of the flow boundary conditions

The fluid domain is divided into two sub-domains, called the upper and lower domain, which are separated by the membrane. The direction of flow is indicated by the two grey arrows, and is therefore in the x direction for both subdomains. The flow thus runs from the inlet of each sub-domain to the corresponding outlet and is framed by the static outer walls and the moving membrane.

Table 8 summarizes the conditions applied to each boundary.

Table 8: Boundary conditions of the numerical model

Boundary	Condition	Details
Upper inlet	Inlet	Absolute velocity
Lower inlet	Inlet	Absolute velocity
Upper outlet	Outlet	Gauge pressure
Lower outlet	Outlet	Gauge pressure
External walls	Wall	No slip wall
Upper membrane face	Wall	Shear defined
Lower membrane face	Wall	Shear defined

There are many different types of boundary conditions, but the focus here is solely on those used in the model. First of all, both inlets experience a velocity condition for which the flow velocity is fixed at that level. The value chosen for this condition for each test is presented in Section 4.2.10.
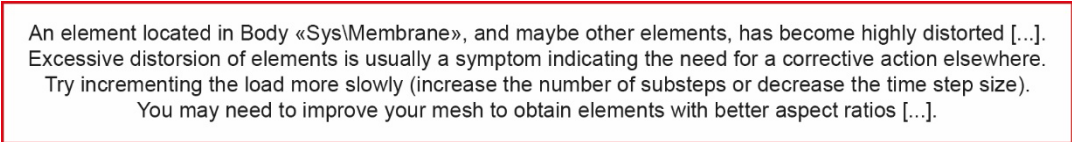
Then, at the other end of the flow, both outlets have a pressure condition. This type of boundary condition requires the input of a Gauge pressure. In order to understand what this term means, it is necessary to go into a little more detail about how pressure is managed by the Fluent module. To avoid having to calculate very small pressure differences when the pressure value is very high, Fluent divides the pressure field into two distinct components, the sum of which is equal to the absolute pressure. The operating pressure, a pressure field that is constant throughout the simulation and often equal to atmospheric pressure, is subtracted from the absolute pressure so that Fluent only has to deal with the Gauge pressure, the same pressure that must be entered in the pressure boundary conditions. However, as explained in Section 4.2.7, the pressure on the membrane is defined in the structural domain and therefore the Gauge pressure at the outlets of the fluid domain is always defined as zero.

There are also different boundary conditions for walls. In the model used, the external walls are set to a condition called no slip, which defines both the normal and tangential velocity at the wall as zero. This condition was chosen to best represent the conditions experienced by a physical model that could be subsequently built by the laboratory. As for the membrane, a shear condition involving the roughness of the material was chosen. The membrane's roughness is thus defined according to the equivalent sand-grain roughness of PVC-P, assumed to be $1.5 \cdot 10^{-6}$m.

4.2.7 Loading

Despite the use of linear order elements such as SOLID285 as recommended in the technical literature of Ansys, the structural domain mesh distortion problem presented in Section 4.2.4 remains pervasive throughout the model. Indeed, it seems that the application of relatively high pressures on a hyperelastic material that naturally deforms a lot leads to very high stress on the sensitive mesh of the membrane, which is by definition a thin body and therefore has few elements over its thickness.

It soon became clear that the few adjustments to the mesh parameters would be insufficient for it to withstand the pressure of the order of several bars to which the membrane is exposed in the pressure tunnels. When the pressure applied instantaneously on the membrane exceeds a value of 3000Pa, the Transient Structural module returns the error message shown in Figure 44.

An element located in Body «Sys\Membrane», and maybe other elements, has become highly distorted [...].
Excessive distorsion of elements is usually a symptom indicating the need for a corrective action elsewhere.
Try incrementing the load more slowly (increase the number of substeps or decrease the time step size).
You may need to improve your mesh to obtain elements with better aspect ratios [...].

Figure 44: Error message for element distortion returned by Transient Structural

Since improving the mesh size proved to be an insufficient solution, an attempt was made, as suggested in the error message in Figure 44, to increase the pressure linearly over the time steps to reach the desired pressure. It turns out that this solution of ramping up the pressure does indeed work and that one way of overcoming this distortion is to divide the modeling process into two distinct phases. Figure 45 shows how the pressure is defined and varies over the course of the calculation, as well as the consequences of this evolution on the membrane deformation.
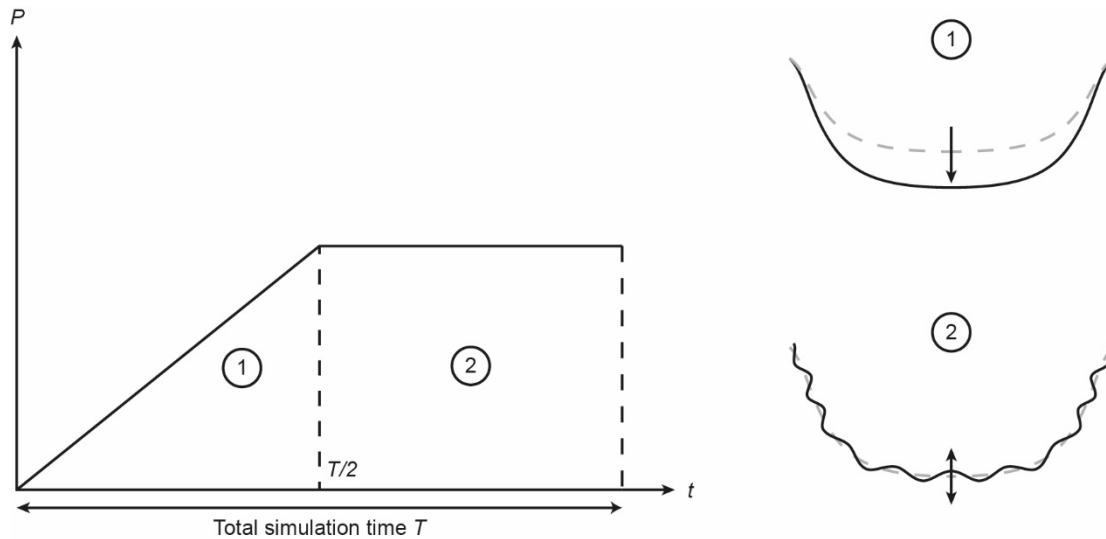
Figure 45: Evolution of the pressure over the course of the calculation and resulting deformation of the membrane

In the first phase, the pressure is increased incrementally to allow the membrane to deform gradually, thus avoiding mesh distortion errors. In this first phase, the membrane's deflection gradually increases until it reaches the deformation corresponding to the final pressure applied. The membrane is already in contact with the flow during this first phase to avoid problems of mapping, i.e. matching of the meshes of the solid and fluid domains since one would be deformed and the other not but this phase can still be seen as the formation phase of the deformation generated by the hydrostatic component of the flow.

Although it is already possible for membrane oscillations to occur in this phase, and it is interesting for quantifying static membrane deformation, it is not sufficient to answer the questions posed in Section 2.4.

In order to answer these questions, it is necessary to model a phase in which the boundary conditions are constant. For this reason, in the second phase, the pressure is kept constant as the corresponding deformation is reached, so that the dynamic behavior of the membrane can be analyzed. This phase corresponds to the phase during which the hydrodynamic component linked to flow and turbulence is properly added to the membrane deformation. It is mainly in this second phase that membrane oscillations can occur, which is why the deformation of the membrane during this phase in Figure 45 is shown with undulations.

An attempt to implement this pressure evolution was first made by defining in Fluent the boundary conditions at the pressure outlets presented in Section 4.2.6 as time-varying expressions in order to reproduce the graph shown in Figure 45. However, this attempt proved unsuccessful, as the problem of distortion of the structural domain mesh elements continued to appear without any explanation being found. It was therefore necessary to apply pressure not in the fluid domain with Fluent, but in the structural domain with Transient Structural. The actual fluid pressure is therefore modeled by an equivalent pressure applied homogeneously in the structural domain on the top surface of the membrane. The consequence of this solution is that the pressure field in the fluid domain does not correspond to the real pressure field, since it does not include the static pressure component. It is therefore somehow homogeneously shifted by the pressure value defined by Transient Structural.

Since the first phase is mainly used to set up the hydrostatic deformation, and therefore contributes little to the analysis of the membrane's dynamic behavior, it is essential that it contains as few time steps as possible, so as not to increase the computational cost of modeling unnecessarily, and thus limit computation time. An analysis was carried out to determine the maximum pressure increment that can be added to each time step without triggering a problem of mesh element distortion. This analysis was carried out both on the mesh created using 3D SOLID285 elements, and on the mesh made up of SHELL181 planar elements by omitting the effect of gravity and applying a pressure increasing linearly from 0bar at time T=0s to the maximum pressure attainable without causing distortion of the elements at time T=1s. The main resulxts are presented in Table 9 and are available in their full form in the appendix.

Table 9: Analysis of maximum pressure increment for meshes with SOLID285 and SHELL181 elements

Characteristic	SOLID285	SHELL181
Number of nodes	18'651	12'616
Degrees of freedom per node	3	6
Total degrees of freedom	55'963	75'696
Maximal pressure for 1 time step [bar]	0.03	0.01
Computation time for 1 time step [s]	14	8
Maximal pressure for 10 time steps [bar]	0.30	0.11
Computation time for 10 time steps [s]	43	24
Maximal pressure for 100 time steps [bar]	3.08	1.10
Computation time for 100 time steps [s]	314	140
Total deformation for 1bar with 100 time steps [mm]	57.4	57.3

The results presented in Table 9 justify the choice made in Section 4.2.4, i.e. to use SOLID285 volume elements rather than SHELL181 planar elements with virtual thickness, since the maximum pressure supported by the latter is systematically lower than that supported by 3D elements, whatever the number of time steps.

Another important finding is that there is a clear linear dependency between the number of time steps and the maximum pressure supported for both meshes. This indicates that the triggering condition of the mesh element distortion problem lies not in the final absolute pressure applied, but in the pressure increment added at each time step, which is why the error message shown in Figure 44 suggests gradually increasing the pressure. The results show that the maximum pressure increment that can be added to each time step is around 3000Pa. In reality, this limit may well be slightly lower, since during system coupling, the hydrodynamic component of the deformation due to flow is also added, whereas the analysis whose results are presented above is carried out only on the structural domain.

Finally, the last row of Table 9 provides a rather reassuring result, since it shows that for an equal load, the two meshes provide a substantially similar result. This concordance testifies to the precision of the mesh used. It is unfortunately not possible to assess the representativeness of the results until a physical model has been built in the laboratory and the results provided by the two models compared.

4.2.8 Turbulence model

The Navier-Stokes equations describe both laminar and turbulent flows. However, for the modeling of turbulence, turbulence models are used in order to reduce the computational costs. These models are a computational procedure to close the governing equations. There are many models available for modeling turbulence in Ansys Fluent. The development of each of them is well beyond the scope of this work, and this section is therefore intended simply as a quick introduction to turbulence modeling in fluid flow simulation software, as well as a presentation of the turbulence model used in this work.

These numerous turbulence models can be divided into three main categories. The first category contains models called RANS for Reynolds-Averaged Navier-Stokes, offering the most economical approach to computing complex turbulent industrial flows and based on the Reynolds Ensemble Averaging method (Ansys, 2021b). In this method, the solution variables in the instantaneous Navier-Stokes equations are decomposed into the mean component, that can be ensemble-averaged or time-averaged, and the fluctuating component. By substituting this decomposition for the variable flow in the continuity and momentum equations presented in Section 4.1.3, the RANS equations are obtained. These equations have the same general form as the instantaneous Navier-Stokes equations, but introduce an additional term called Reynolds stresses (Ansys, 2021a). In order to close the momentum equation, these Reynolds stresses must be modeled, and this is the role of every turbulence model in this category.

The second category is made up of SRS, scale-resolving simulation, models, the best-known of which is probably the LES model for Large Eddy Simulation. This type of model offers greater representativeness and fidelity of the solution, since they resolve at least a portion of the turbulence for at least a portion of the flow domain, but at higher computational costs due to its high resolution requirements for wall boundary layers (Ansys, 2021b). The central resolution principle lies in the filtering of the time-dependent Navier-Stokes equations. The filtering process effectively filters out the eddies whose scales are smaller than the filter width or grid spacing used in the computations. By applying this convolution operation, the effect is to average out any phenomena that happens on small length scales and small time scales, thereby eliminating the influence of fast flow fluctuations and small length scale flow behavior. Similarly to RANS modeling, in LES turbulence models aim at resolving the unknown terms in the filtered Navier-Stokes equations, called the Sub-grid Scale stresses.

The third and final main category of turbulence models is made up of hybrid models, incorporating parts of each of the approaches from the first two categories. Although at first sight the concepts of the RANS and SRS methods may appear to be incompatible, since they result in different additive terms in the momentum equation, it is actually possible to get the best out of each by dividing the fluid domain into sub-domains covered by one or other of the methods. With hybrid models, the attached wall boundary layers are typically covered by the RANS part of the model, while large detached regions are handled in 'LES' mode, meaning with a partial resolution of the turbulent spectrum in space and time. Many hybrid models have been developed in recent years to avoid the high resolution requirements of SRS models, while still allowing partial resolution of turbulence where necessary. These models are particularly useful in cases where there is an obstacle in the flow, in order to model the vortices forming behind the obstacle.

The turbulence model defined for the moment is a RANS-type model called the k-ω SST turbulence model. This turbulence model is an improvement on the k-ω BST turbulence model and it is therefore necessary to first understand how this first model works in order to understand the model used.

The k-ω BST turbulence model is the result of a merger between two other turbulence models developed earlier: the k-ε and the k-ω models. It turns out that each of these models, developed first, has its problems. Thus, the near wall damping functions used in the k-ε model become unreliable when the model is used in a variety of flows that differ from those used for model calibration, whereas the values given by the k-ω model are sensitive to the freestream value of turbulence that is applied at the inlet (Menter, 1994). These two problems often lead to an overestimation of wall shear stress, and thus to the modeling of flows that do not separate from smooth surfaces, whereas practical experience shows that they do. The k-ω BST turbulence model attempts to address these problems and give a better separation prediction by introducing a blending function that allows to to switch from the k- model to the k-ω model and vice versa, depending on the location in the fluid domain under consideration.

The transport equation for turbulent kinetic energy k for the k-ω BST model then becomes (Menter, 1994):

$$\frac{\partial(\rho k)}{\partial t} + \nabla \cdot (\rho \boldsymbol{u} k) = \nabla \cdot \left(\left(\mu + \frac{\mu_t}{\sigma_k} \right) \nabla k \right) + P_k - \rho \epsilon \tag{4.20}$$

And the transport equation for the turbulent dissipation rate ω is:

$$\frac{\partial(\rho \omega)}{\partial t} + \nabla \cdot (\rho \boldsymbol{u} \omega) = \nabla \cdot \left(\left(\mu + \frac{\mu_t}{\sigma_k} \right) \nabla \omega \right) + \frac{\gamma}{\nu_t} P_k - \beta \rho \omega^2 + 2(1 - F_1) \frac{\varphi \sigma_{\omega 2}}{\omega} \nabla k \cdot \nabla \omega \tag{4.21}$$

The idea is thus to define this blending function F_1 as taking a value equal to one close to the walls in order to recover the k-ω model, and on the contrary to define the blending function as zero far from the walls in order to fall back on the k-ε model. Figure 46 illustrates how this blending function works.
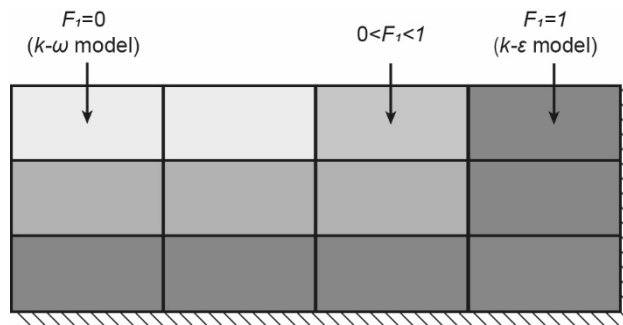
Figure 46: General operation of the blending function

The bending function is described by Equation 4.22.

$$F_1 = \tanh(arg_1^4) \tag{4.22}$$

The term arg_1 is described by a complex relationship that is not detailed here, but this term mainly depends on the distance to the nearest wall. The bending function thus follows the curve shown in Figure 47.
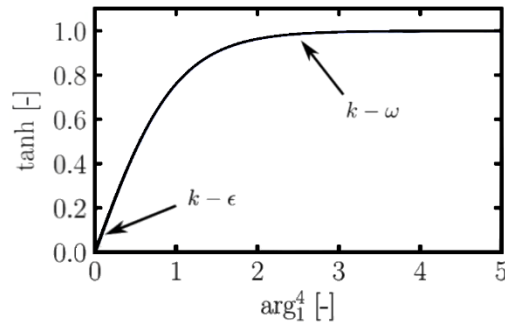
Figure 47: General form of the bending function

Despite the introduction of this F_1 blending function, it turns out that the k-ω BST model tends to encounter the same problem as the two models from which it is derived, namely an overestimation of wall shear stress. To overcome this problem once and for all, the k-ω SST model was created, with the addition of a viscosity limiter.

Viscosity is thus no longer defined as $\mu_t = \frac{\rho k}{\omega}$ as in the BST model, but takes the form described in Equation 4.23.

$$\mu_t = \frac{a_1 \rho k}{\max(a_1 \omega, SF_2)} \tag{4.23}$$

where F_2 is another belnding function similar to F_1 and S is the magnitude of the shear stress. Thus, if F_2 or S is large, then the viscosity is limited.

The addition of this viscosity limiter enables the k-ω SST model to gives a better agreement with the experiments of midly separated flows. Hence, it is best for external aerodynamics or simulations where separation is important.

4.2.9 Configuration of the system coupling

Since the aim of this work is to study the influence of flow on the membrane, it is necessary that the system coupling participants exchange data in order to take into account the influence of the behavior of one on the behavior of the other.

So, since the membrane is meshed using volume elements and is in contact with the flow on its two main faces, it was necessary to define two fluid-structure interaction interfaces, one for the upper face and the other for the lower face of the membrane. As the model simulates a two-way fluid-structure interaction, two data exchange links are created for each fluid-structure interface. Table 10 below shows the characteristics of each of these coupling system links.

Table 10: System coupling data transfers resulting in the dynamic boundary conditions

Designation	Region	Source	Target	Variable
L1	Upper face	Fluent	Transient Structural	Force
L2	Upper face	Transient Structural	Fluent	Displacement
L3	Lower face	Fluent	Transient Structural	Force
L4	Lower face	Transient Structural	Fluent	Displacement

As explained in Section 4.1.5, each link transmits data from the fluid domain to the solid domain or vice versa. In this case, the links from the fluid domain to the structural domain transmit the force applied by the flow on the membrane, while the links from the structural domain to the fluid domain transmit the resulting displacements of the membrane.

4.2.10   List of experiments

In order to test the model and visualize its results, numerous tests were carried out. Many of these proved to be error-prone in one way or another, but enabled the model's development to move forward. The tests presented in Table 11 are those that could be carried out successfully using the final phase of the model as described in the previous sections.

Table 11: List of the successful tests

Designation	Total simulation time [s]	Time step size [s]	Maximum pressure applied [bar]	Upper inlet velocity [m/s]	Lower inlet velocity [m/s]
T1	10	0.1	1	0	0
T2	10	0.1	1	1	0
T3	10	0.1	1	4	1
T4	10	0.1	2	1	0

Table 11 shows that the time step size defined for successful tests does not correspond to the optimum size for capturing possible membrane vibrations discussed in Section 4.2.5, which is around 0.1s. The reason for this choice is that selecting time steps close to the optimum size generates errors during the computation, as discussed in Section 6.2.3.

Chapter 5   Preliminary results

This failure to obtain a very fine temporal discretization, the long calculation time and the time required to develop the model make it impossible to carry out a precise study to characterize the vibratory behavior of the membrane in a single semester. The results presented in this chapter are therefore preliminary, intended more to visualize the model outcomes than to be used for a quantitative analysis of membrane dynamic behavior. However, as the model has been developed with accuracy and representativeness in mind, the order of magnitude of the static variables is assumed to be correct.

5.1   Hydraulic results

As mentioned in Section 4.2.1, results for the fluid domain are processed using the CFD-Post module. Although there are software packages available that allow a more cosmetic presentation of the results, this module is proposed by default and has the great advantage of not requiring results to be exported, since it reads the resulting files directly from the coupling system. Even if CFD-Post doesn't offer all the existing functions, its ease of use makes it an ideal tool for presenting preliminary results.

5.1.1 Pressure field

Figure 48 shows the hydrodynamic pressure distribution along a longitudinal plane passing through the center of the membrane for the last time step of the simulation for test 3.
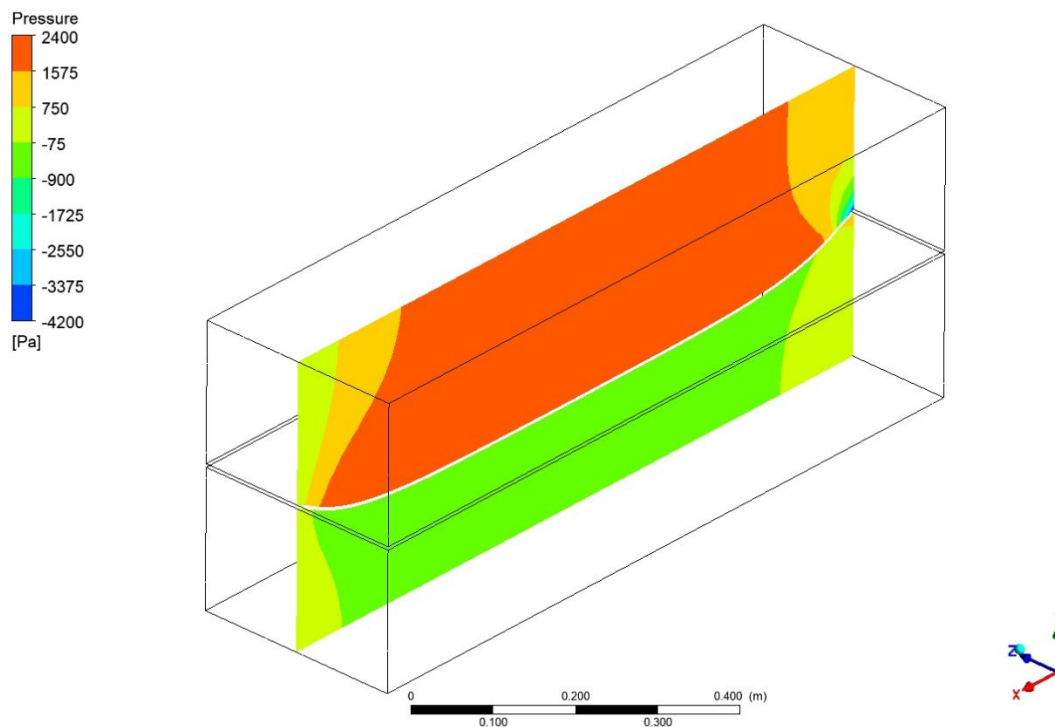
Figure 48: Hydrodynamic pressure [Pa] in the XY plane at *t*=10s for test 3

Figure 49 shows the hydrodynamic pressure distribution along a transverse plane passing through the center of the membrane for the last time step of the simulation for test 3.
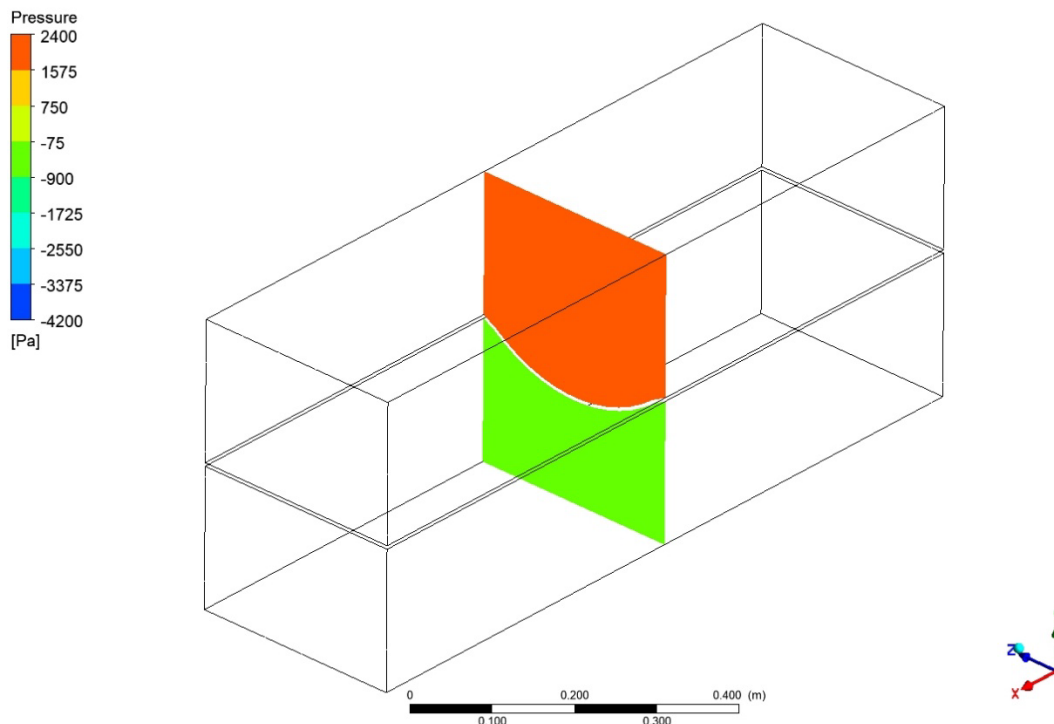

Figure 49: Hydrodynamic pressure [Pa] in the YZ plane at t=10s for test 3

As explained in Section 4.2.7, the forced decision to apply hydrostatic pressure directly to the membrane with Transient Structural rather than to the flow with Fluent means that the pressure field calculated by the latter module does not take the hydrostatic component into account. The pressure field shown in Figures 48 and 49 therefore does not correspond to the real pressure field, since it only represents the hydrodynamic component. The actual pressure field thus corresponds to the field shown above shifted by a constant value equal to hydrostatic pressure.

However, the advantage of this representation is that it allows the analysis of the hydrodynamic pressure field and the comparison between the static component, which is known because it is parameterized in Transient Structural, and the dynamic component shown here.

In particular, it's possible to notice that the results tend to find a certain symmetry in the plane that presents them. Figure 48 shows that the boundary conditions encountered at the start of the flow are close to those at the other end of the fluid domain. This symmetry, leading to similar conditions at the very upstream and downstream ends, can also be seen in the velocity field presented in Section 5.1.2. Figure 49 shows that the hydrodynamic pressure distribution is relatively constant across the section in the z direction. This can be explained by the symmetry of the section and the absence of a boundary condition defining the pressure on the surrounding walls.

However, the most interesting finding is that the figures above show that the hydrodynamic pressure is between -4200 and 2400 Pa in the highest case, corresponding to test 3, while hydrostatic pressure is at least 100'000 Pa. Flow-induced pressure variations are therefore insignificant compared with the hydrostatic pressure in place.

5.1.2 Velocity field

Figure 50 shows the velocity distribution along a longitudinal plane passing through the center of the membrane for the last time step of the simulation for test 3.
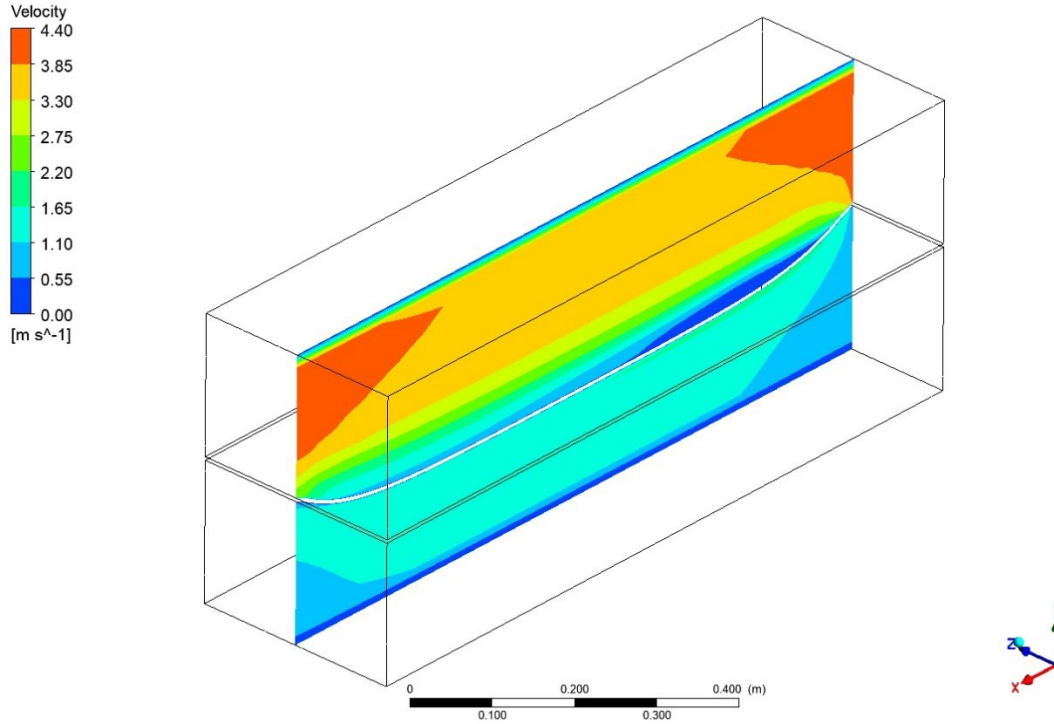
Figure 50: Water velocity [m/s] in the XY plane at *t*=10s for test 3

Figure 51 shows the velocity distribution along a transverse plane passing through the center of the membrane for the last time step of the simulation for test 3.
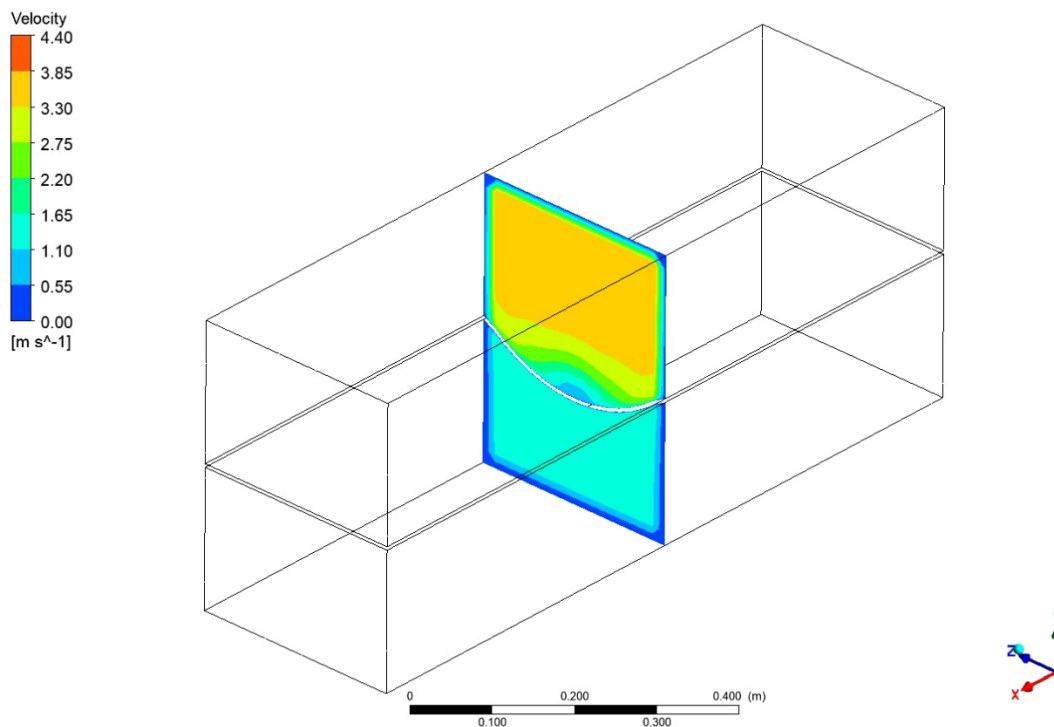
Figure 51: Water velocity [m/s] in the YZ plane at *t*=10s for test 3

Figures 50 and 51 above show that the applied velocity boundary conditions are effective and impact the flow as expected. Indeed, it can be seen in Figure 50 that the velocities at the start of the flow correspond to 4 and 1 m/s, as indicated in Table 11. The velocity then tends to decrease in the upper fluid sub-domain due to the increase in flow cross-section caused by membrane deformation, before increasing again as the outlet approaches, since the cross-section decreases again, while the opposite phenomenon logically occurs in the lower sub-domain. Figure 51 shows that slipping conditions at wall level are effective. It can be seen that the velocity is zero at the perimeter of the outer walls, while it also decreases in the vicinity of the membrane due to its roughness.

It is also interesting to note that the flow velocity is homogeneous in the lower fluid sub-domain, whereas very different velocities can be observed near the membrane in the upper sub-domain. It would seem, therefore, that the movement of the membrane tends to create more disturbance in the flow when confronted with a convex than a concave obstacle. So, even if no turbulence is perceptible in the results produced here, it may seem legitimate to think that this phenomenon is more likely to occur in the upper subdomain, close to the membrane, than in the lower subdomain.

In addition to representing velocity by means of contours on different planes, the CFD-Post module also allows to visualize the flow by means of streamlines and velocity vectors. These two types of representation give a better idea of the general behavior of the flow and of any curvatures in the streamlines.

Figure 52 shows streamlines whose color corresponds to the flow velocity for the last time step of the simulation for test 3.
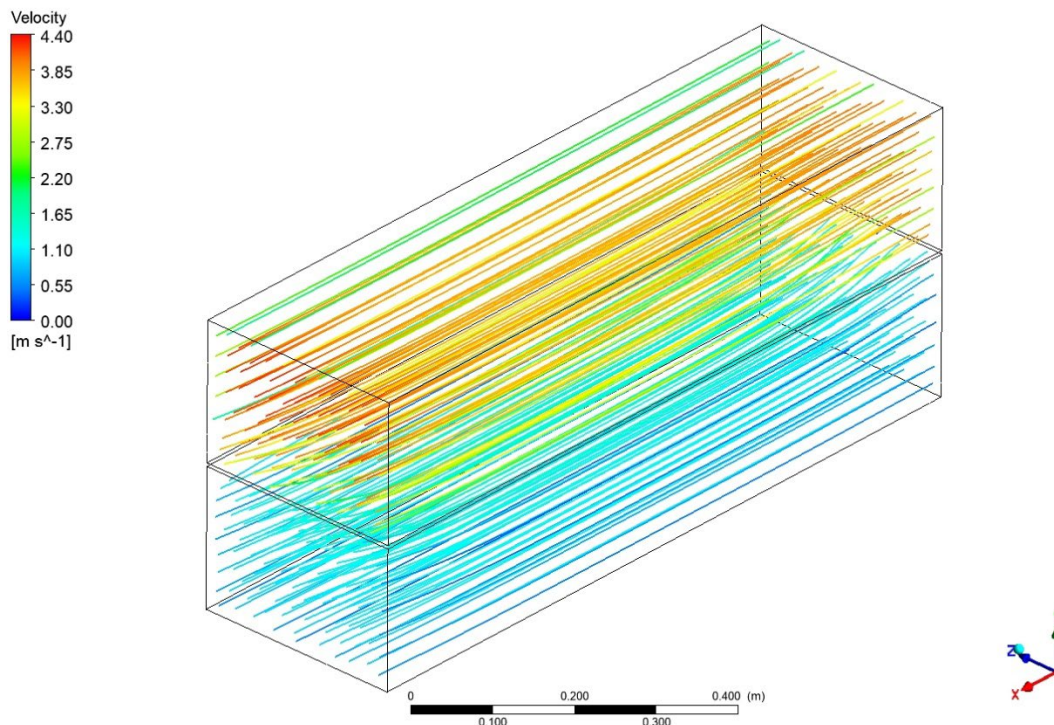
Figure 52: Streamlines [m/s] at *t*=10s for test 3

Figure 53 shows the velocity vectors for different points in the flow for the last time step of the simulation for test 3. The color and intensity of these vectors both enable to visualize the corresponding velocity.
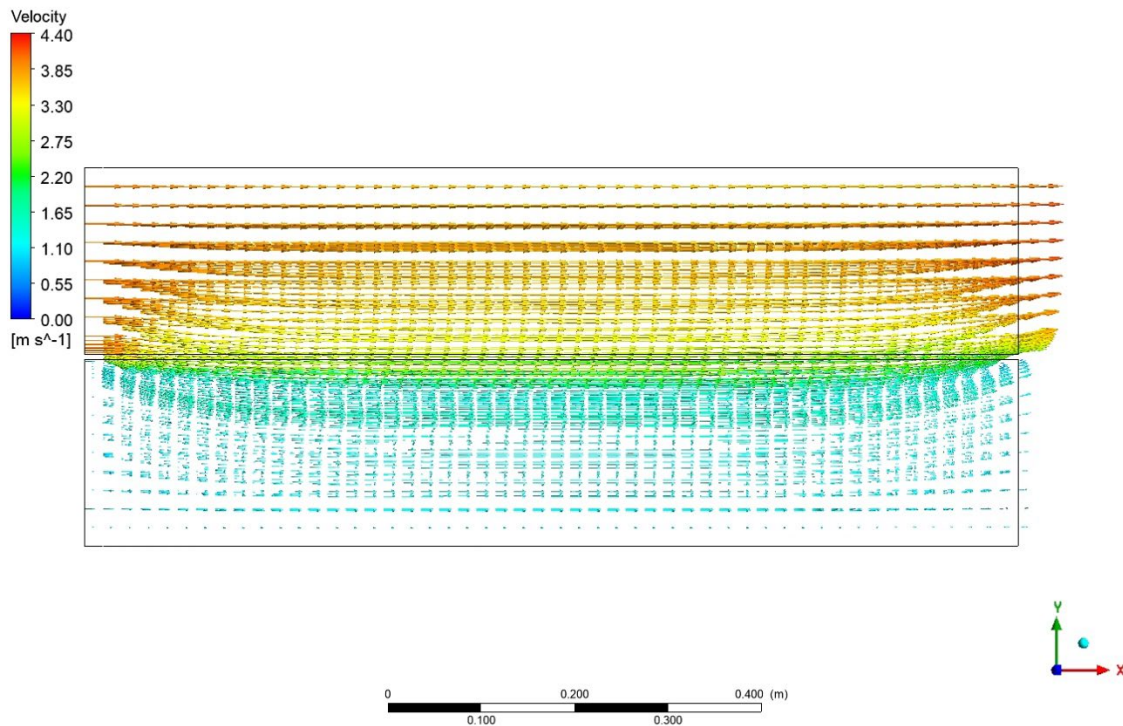
Figure 53: Velocity vectors [m/s] in the XY plane at *t*=10s for test 3

Figures 52 and 53 show the wireframe of the fluid domain in its undeformed position, since the deformation of the membrane is managed by the Transient Structural module, but the deformation is taken into account by the flow. Indeed, it can be seen that the streamlines are curved near the membrane and that the velocity vectors are not all parallel. This confirms that the coupling system is working properly, since membrane deformation does have an impact on the flow.

These results also confirm what can be observed on the different sections presented previously, namely that velocities progressively decrease in the upper sub-domain for streamlines approaching the membrane, while velocity is very homogeneous in the lower sub-domain. This break between the two sub-domains is particularly visible in Figure 53, where the color and density of vectors change abruptly on an interface corresponding to the membrane in its deformed position.

5.2   Structural results

The results for the structural domain are processed using the Transient Structural module. The software interface is the same as that already used to create the mesh or define pressure and boundary conditions in the structural domain. The interface is easy to use and allows to quickly visualize a wide range of results. Therefore, not all results obtained for the different variables of interest are presented in the body of the report, but the full set of results is available in the appendix.

Rather than successively presenting a series of results for different variables, as was done for the fluid domain, this section proposes to study the impact of the choice of different boundary conditions, i.e. velocity and pressure, on membrane deformations. A final section is devoted to the analysis of a strange oscillation phenomenon that occurs systematically during simulation.

5.2.1 Influence of pressure

To assess the impact of hydrostatic pressure applied to the membrane on its deformation, the results obtained for tests 2 and 4 are compared. In fact, these tests have the advantage of having the same boundary conditions in terms of velocity, with only the hydrostatic pressure changing, test 2 having a pressure of 1bar and test 4 a pressure of 2bar.

Figure 54 shows the out-of-plane deformation of the geomembrane for the last time step of the simulation for test 2.
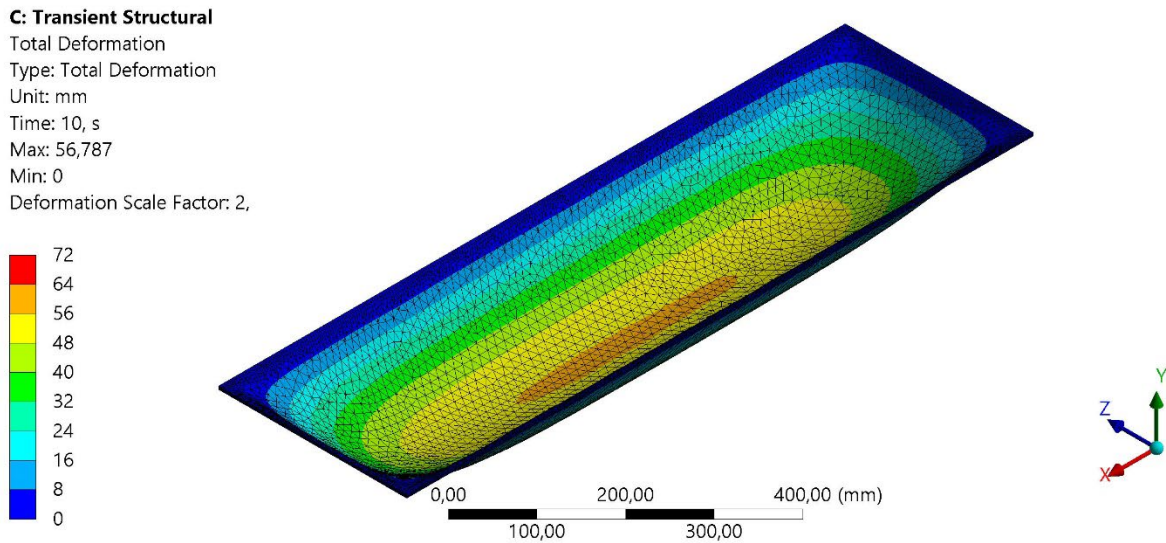
Figure 54: Geomembrane out-of-plane deformations [mm] at *t*=10s with a deformation scale factor of 2 for test 2

Figure 55 shows the out-of-plane deformation of the geomembrane for the last time step of the simulation for test 4.
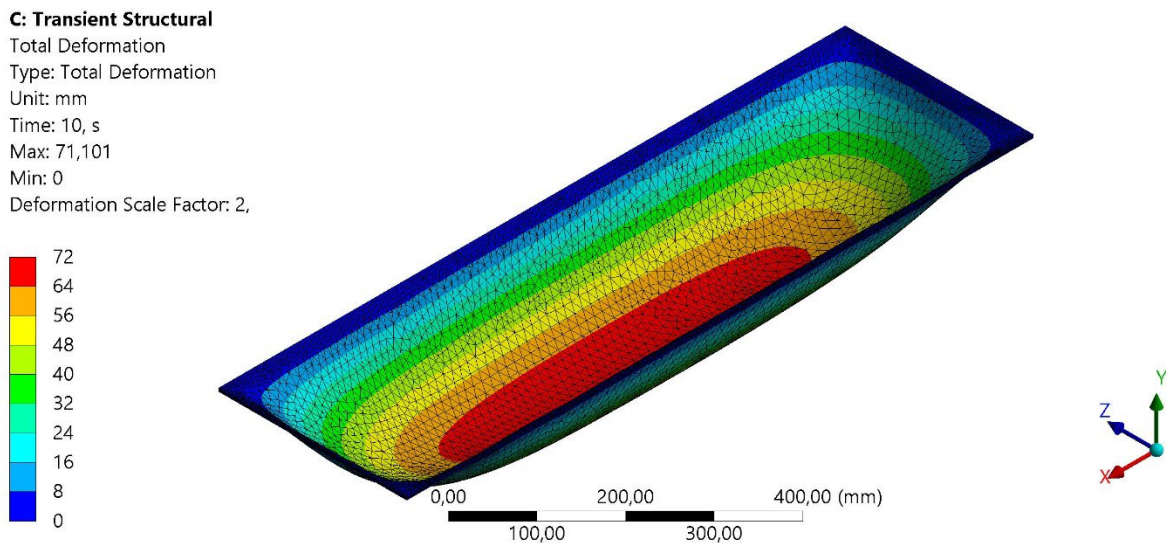
Figure 55: Geomembrane out-of-plane deformations [mm] at *t*=10s with a deformation scale factor of 2 for test 4

Figures 54 and 55 confirm the expected logic, i.e. that greater hydrostatic pressure applied to the membrane induces greater membrane deformation. In order to quantify this increase, membrane deformation values can be exported and plotted in the graphs shown in Figures 56 and 57.
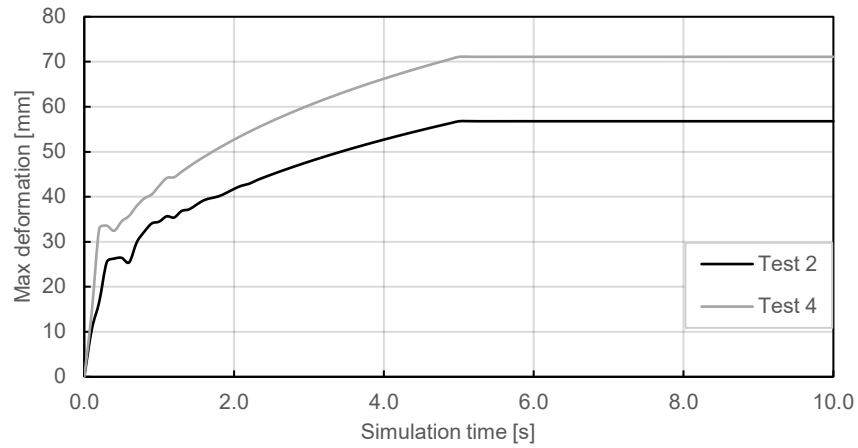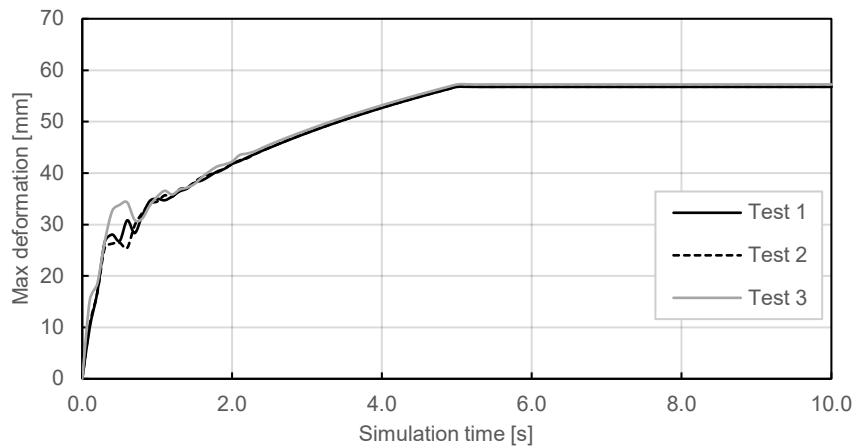
Figure 56: Evolution of the maximum out-of-plane deformation of the geomembrane over time for tests 2 and 4
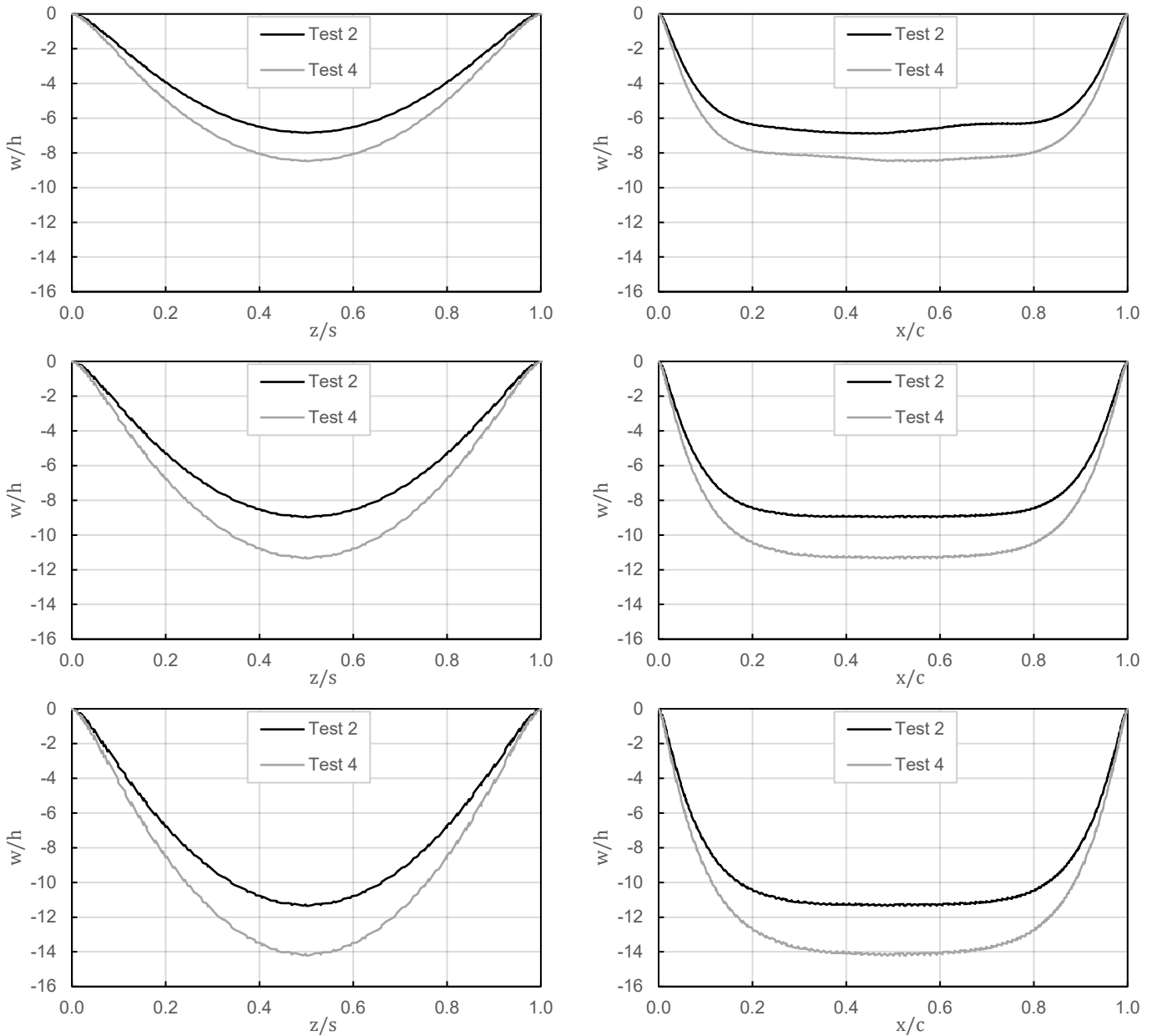
Figure 57: Cross-sections of membrane out-of-plane deformation in YZ plane (section cut) for the left column and XY plane (longitudinal cut) for the right column at times t=1s for the first row, t=2.5s for the second row and t=10s for the third row for tests 2 and 4

Figure 56 shows the evolution of the maximum out-of-plane deformations experienced by the membrane over the course of the simulation for tests 2 and 4, while Figure 57 shows scaled cross-sections of the membrane deformation in the XY and YZ planes for different phases of the simulation.

The graphs in Figures 56 and 57 show that doubling the pressure significantly increases the resulting membrane deformation. It is interesting to note, however, that although the pressure is doubled, the deformations are not multiplied by the same factor. This is due to the simple supports present around the perimeter of the membrane, which induce a non-linearity between the applied pressure and the resulting out-of-plane deformations.

Figure 57 also shows that membrane dimensions obviously have an impact on membrane deformation. Transversal sections thus take on a relatively marked u-shape, while longitudinal sections show a relatively flat deformation at its maximum. This means that deformations tend to be concentrated at the edges of the membrane. This postulate can be confirmed by looking at the distribution of strains on the membrane, illustrated as an example in Figure 58 for the last time step of test 4.
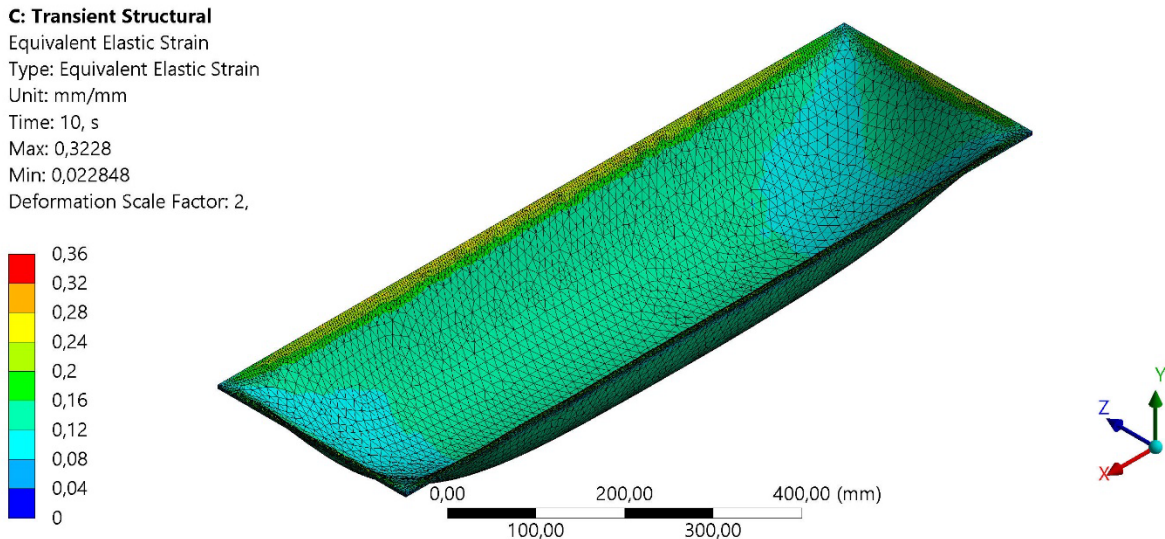
Figure 58: Geomembrane strains [-] at t=10s with a deformation scale factor of 2 for test 4

Figure 58 above clearly shows that the most important strains, indicated in yellow, are concentrated near the edges of the membrane, which means that this is where the mesh elements deform the most. This observation justifies the implementation of mesh refinement, as detailed in Section 4.2.4, which helps combat the problem of mesh element distortion and improves the accuracy of results.

5.2.2 Influence of velocity

In order to study the influence of the velocities defined at each of the fluid sub-domain inlets, the results of tests 1, 2 and 3 are compared, since these tests all have the same hydrostatic pressure applied to the membrane.

In order to vary the variables represented for these preliminary results, it was decided this time to represent the results obtained for strain energy. Figure 59 shows the strain energy distribution for each membrane element for the last time step of the simulation for test 1.
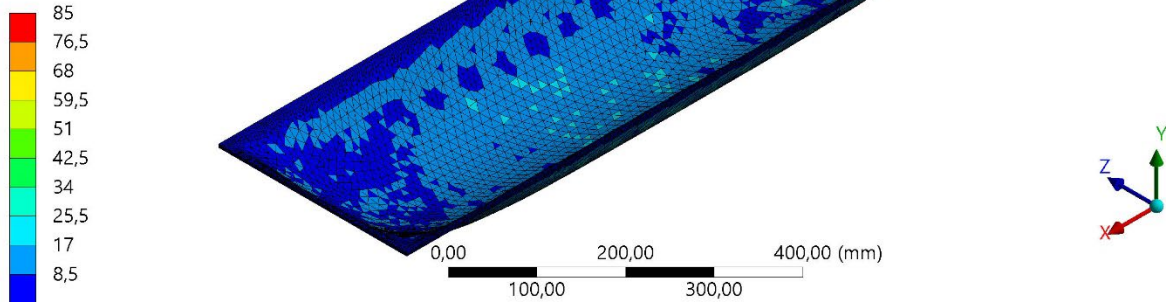
Figure 59: Geomembrane strain energy [mJ] at t=10s with a deformation scale factor of 2 for test 1

Figure 60 shows the strain energy distribution for each membrane element for the last time step of the simulation for test 3.
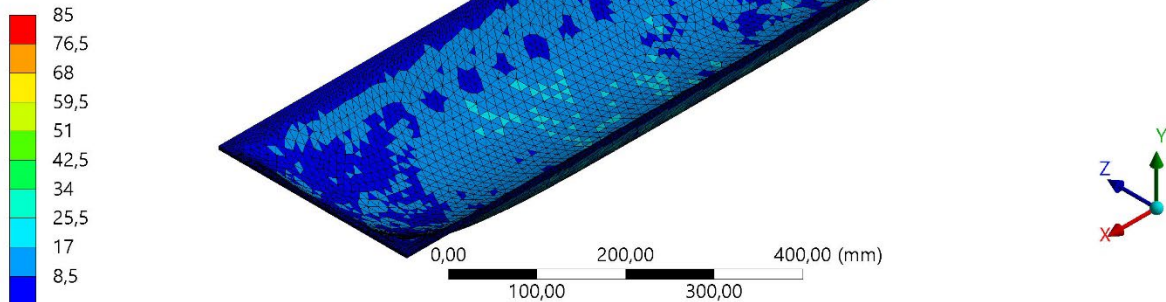
Figure 60: Geomembrane strain energy [mJ] at t=10s with a deformation scale factor of 2 for test 3

Figures 59 and 60 look almost identical. On closer inspection, however, it can be seen that the overall strain energy is slightly higher for test 3 than for test 1. This observation can be confirmed by the fact that the maximum strain energy is indeed slightly higher for test 3.

In order to confirm whether this similarity can also be found in the out-of-plane deformations of the membrane for each of the considered tests, the evolution of these deformations over the course of the simulations is shown in Figure 61.

Figure 61: Evolution of the maximum out-of-plane deformation of the geomembrane over time for tests 1, 2 and 3

As shown in Figure 61, a difference in velocity between the two fluid subdomains induces far less deformation than an increase in hydrostatic pressure. Indeed, with the exception of the oscillation phase discussed in Section 5.2.3, no difference is discernible in Figure 61 for the different tests, despite their different velocity boundary conditions. To see whether this difference nevertheless implies a small variation in maximum deformation, a focus is proposed on the phase during which pressure and deformation are static in Figure 62.
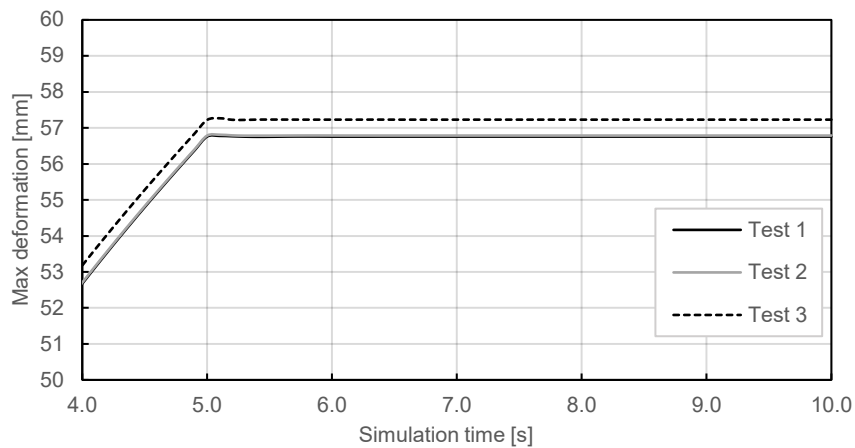
Figure 62: Zoom on the static part of Figure 61

As it can be seen in Figure 62, test 3 induces a slightly greater membrane deformation than tests 1 and 2, which are almost cofounded. This result is quite logical, since test 3 is the one with the greatest difference in velocity, with a difference of 3 m/s, whereas tests 1 and 2 have a difference of 0 and 1 m/s respectively.

In order to determine whether differences in the shape of the deformation appear as a function of flow velocity, the same cuts as above are again performed and presented in Figure 63.
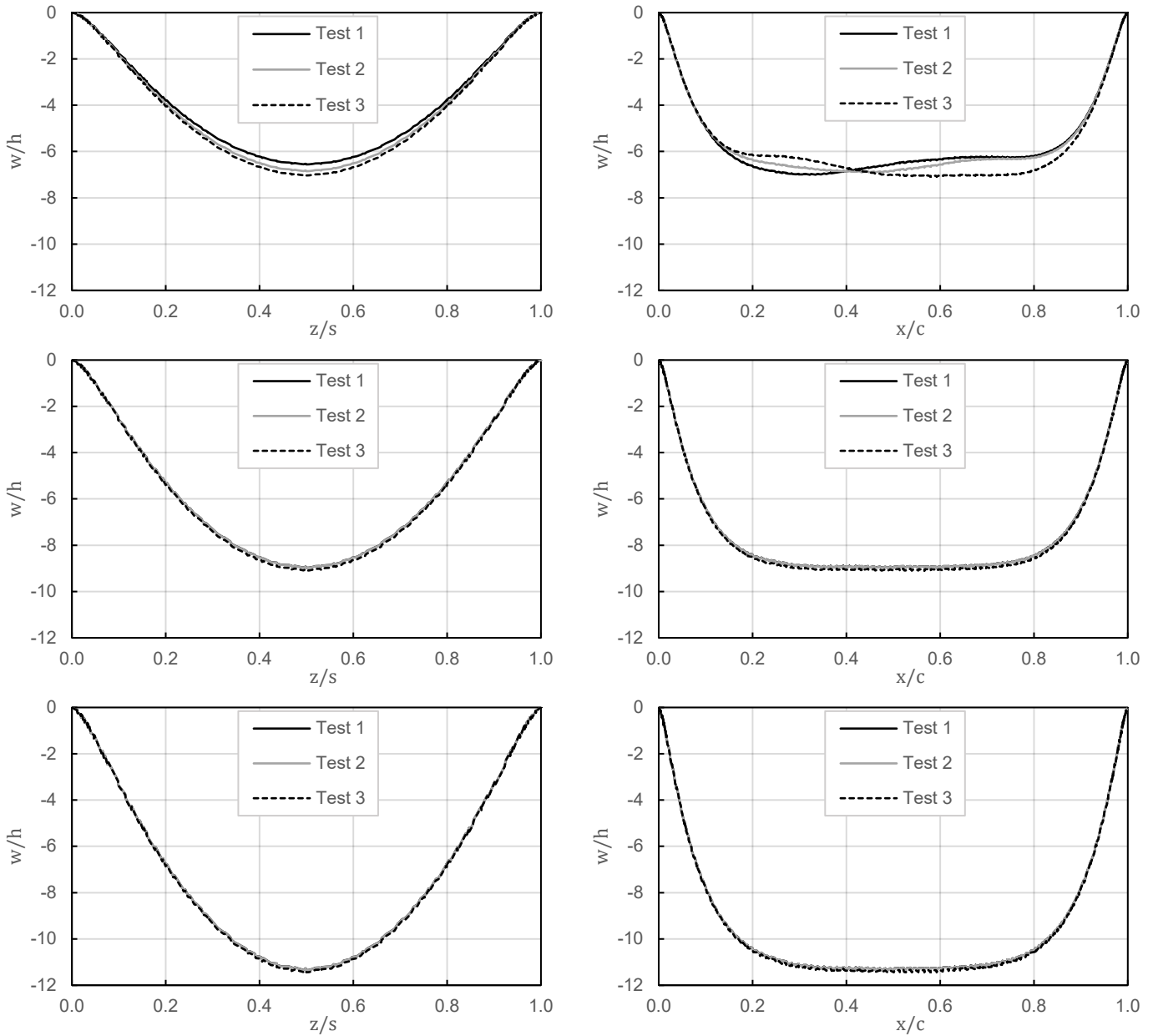
Figure 63: Cross-sections of membrane out-of-plane deformation in YZ plane (section cut) for the left column and XY plane (longitudinal cut) for the right column at times *t*=1s for the first row, *t*=2.5s for the second row and *t*=10s for the third row for tests 1, 2 and 3

Figure 63 shows that the maximum deformation is roughly the same for all the tests considered, with the deformation for test 3 slightly higher, and that the shape of the deformation is also similar. These few results allow us to draw the conclusion that the velocities defined at the inlet of the fluid sub-domains have an important consequence for the flow itself, but have little direct influence on membrane deformation. However, it is possible that flow velocity is an important factor in the appearance of turbulence phenomena, which could not be perceived in the results provided, and which may themselves lead to membrane vibration. So, although the effect of velocity on static deformation is small, it is quite possible that the effect of velocity is greater on the oscillatory movements of the membrane.

5.2.3 Potential oscillations

The various graphs showing the evolution of the maximum out-of-plane deformation show that there is a phase in the simulation occurring between approximately 1s and 1.5s, during which the deformation deviates from the smooth curve it takes the rest of the time to follow an oscillatory behavior. Figure 64 below shows a clear focus on the membrane behavior observed during this oscillation phase for the various tests.
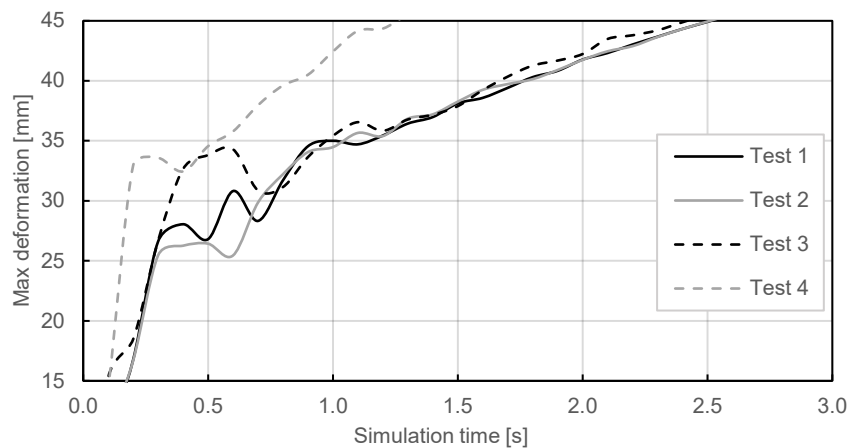
Figure 64: Focus on the oscillatory phase of maximum out-of-plane deformation evolution

Two potential explanations for the appearance of this oscillatory phenomenon are currently being considered. These oscillations could simply be due to imprecision in the calculation at this stage of the resolution. But it's hard to explain why this computation divergence would occur only during this phase and not during the rest of the simulation.

The second explanation, which is more interesting and perhaps more likely given the conditions of appearance, is to consider that these oscillations are actually traces of vibrations picked up by the simulation. In fact, it's possible that the deformation and tension induced in the membrane during this phase create favorable conditions for the membrane to resonate, so that it begins to vibrate, but that the relatively coarse size of the time step doesn't allow the full amplitude of the vibration to be captured, resulting in these kinds of oscillations.

The consequence of this oscillatory phase when refining the time step size is discussed in Section 6.2.3, and ideas that could provide answers as to the reason for these oscillations are proposed in Section 6.3.1.

Chapter 6   Discussion

6.1   Main findings

6.1.1 Consistent but insufficient results

The results presented in Chapter 5 clearly show that the ambition to characterize the dynamic behavior of a geomembrane subjected to pressure flows using numerical software is justified. Indeed, these results are highly consistent with the theoretical behavior of the membrane governed by the equations presented in Section 3.2.2, but above all with the behavior predicted by intuition. In particular, it can be seen that the boundary conditions applied have the desired impact on the results, and that the deformation of the membrane is perfectly consistent with the various loading phases and with the final pressure applied. The built model therefore works properly and allows to analyze the influence of flow on the membrane under certain conditions, the limits of which are presented in Section 6.2. In this way, the model's proper operation testifies to the resolution of many of the problems that can arise during such a simulation. So, although it may seem trivial to a reader uninitiated in numerical modeling, the fact that it is possible to obtain consistent results for such a complex model, as detailed in Section 6.1.2, is in fact already an important finding.

However, these results, promising as they are, are not sufficient to study the dynamic vibratory behavior of the geomembrane. In fact, the modeling parameters chosen do not result in proper vibrations of the membrane, and the model developed is therefore not yet able to characterize the dynamic behavior of the membrane. Although some tests were carried out with parameters that might have allowed the development of membrane vibrations, notably by choosing smaller time step sizes, these led to errors that could not be resolved in the time available for this work. The sources of these errors are explained in Section 6.2, and some possible solutions and development paths are presented in Section 6.3.

6.1.2 Difficulty in building the model

The fact that it is currently impossible to provide results that allow a complete analysis of the dynamic behavior of a geomembrane subjected to pressurized flow is due to the main finding of this work, the difficulty of building a model that can cope with the extreme complexity of this kind of simulation. Indeed, it has been felt throughout this work that the complexity of the model flirts with the limits of what a numerical software like Ansys is capable of modeling today. This approach to the limit of what is technically feasible also explains the difficulty encountered in finding technical literature to solve the problems that arose during model construction. Indeed, even if Ansys offers tutorials (Ansys, 2021c) on how to design a model simulating two-way fluid-structure interaction, for example, or how to model a hyperelastic material, or how to create a mesh for very fine elements, no tutorial describes how to combine these difficulties in a single model. This relative lack of resources is one of the reasons why it was not possible to solve all the problems that arose during model design in a single semester.

What makes the construction of the model so difficult is the combination of the many constraints linked to the characteristics of the problem to be modeled. Modeling a two-way fluid structure interaction is by its very nature a complex task, since it consists in communicating two domains managed by two different modules using different resolution methods, as explained in Section 4.1.

But this original complexity is further exacerbated by the significant stresses generated on the solid mesh by the use of a hyperelastic material subjected to very high pressures and the consideration of a very thin membrane, as detailed in Section 4.2.4. Finally, the need to consider two fluid-structure interfaces rather than just one, as considered in most available technical tutorials, adds further complexity to the model.

Even though the geometry of the model may seem simple, consisting in the end of a parallelepiped with a rectangular membrane at its center, the consequences of this choice of geometry are in fact much heavier than they appear, making the construction of the corresponding model a particularly technical and laborious task. So, although a significant proportion of the problems encountered have been solved, as indicated in Section 4.2, the model still faces certain limits which have not yet been overcome, and which are presented in Section 6.2.

6.2   Limits of the model

The limits of the model appear when the time step size is reduced to around 0.02s. These limitations are the reason for the failures experienced for the tests presented in Table 12, aiming at refining the time discretization in order to characterize possible membrane vibrations occurring at the corresponding time scales.

Table 12: List of unsuccessful tests

Designation	Total simulation time [s]	Time step size [s]	Maximum pressure applied [bar]	Upper inlet velocity [m/s]	Lower inlet velocity [m/s]
F1	1	0.01	1	1	0
F2	1.5	0.01	1	1	0
F3	2	0.02	1	1	0

The failure of these tests can be attributed to several different sources of error or complication, presented in the following Sections 6.2.1 to 6.2.3.

6.2.1 Negative volume of the fluid domain cell

The first problem encountered when refining the size of time steps is an error when updating the dynamic mesh of the fluid domain. The message returned by Ansys when confronted with this error is shown in Figure 65.

Update-Dynamic-Mesh failed. Negative cell volume detected

Figure 65: Error message for negative cell volume returned by Fluent

The principle of dynamic meshing has not been discussed so far, but to put it simply, it's a mesh that evolves over time, adapting to changes in the geometry of the fluid domain as a result of membrane displacement. Ansys therefore reports that updating this mesh to take account of the change in membrane position has resulted in a cell with negative volume, which in effect means that one cell has been covered by another. This problem actually seems to be quite common, and several possible solutions are given in the literature. One frequently encountered solution is to refine the time step, which is rather surprising since, in the case studied, this error occurs precisely when the time step size decreases.

Another proposal suggests that this error is linked to the use of inflation in the creation of the fluid mesh, and that the resulting flattening of the elements could be the cause of the error. After testing, it turns out that eliminating inflations in the fluid domain mesh does indeed avoid this error. In order to maintain greater accuracy of the velocity field near the membrane, the inflations were replaced by refinements. As it happens, setting up these refinements rather than the inflations greatly increases the number of degrees of freedom in the mesh (around 10x), which considerably lengthens the calculation time.

Also, since even with refinements, the calculation generates the error presented in Section 6.2.3, it has been decided, in order to save calculation time, to keep the fluid domain mesh with inflations as presented in Section 4.2.4 for the time being knowing that this error could be overcome by modifying the mesh.

6.2.2 Computation time requirement

Another challenge in modeling a two-way fluid structure interaction is the computation time required to build the model. Indeed, this kind of modeling tends, due to its complexity, to generate significant computation times. To obtain the computation times, it is possible to refer to the system coupling log that gives the total computation time and its distribution among the three participants once the coupling is solved. Table 13 below shows the calculation times required for each of the different tests carried out.

Table 13: Computation time required for each test and division between the system coupling participants

Designation	Fluent coupling time [h]	Transient Structural coupling time [h]	Coupling engine time [s]	Total computation time [h]
T1	0.50	69.16	0.08	69.74
T2	0.44	62.53	0.08	63.05
T3	0.54	89.32	0.08	89.94
T4	0.42	64.39	0.08	64.89

A first important observation is that these results confirm the trend that two-way fluid structure interactions require very high computation times, since the resolution of the model constructed can require up to nearly 4 days of continuous computation. And yet the machine used for the calculations, whose characteristics are shown in Table 14, is relatively powerful. In fact, calculation time depends mainly on the quality of the processor, and this machine has an excellent processor, since Intel estimates its market value at nearly $3,000 (Intel, 2023).

Table 14: Characteristics of the machine used to solve the model

Component	Specification
Operating system	Windows Server 64bits 2019
Processor	Intel Xeon Gold 6142 CPu 2.6 GHz
Number of processors used	11 out of 12
Intalled memory (RAM)	16 GB

An interesting observation from Table 13 concerns the distribution of computing time between the Fluent and Transient Structural modules.

While we might expect these two modules to share roughly equal computing time, it would appear that Transient Structural requires far more computational resources than Fluent. This is all the more surprising given that the fluid domain mesh has a greater number of degrees of freedom than the structural domain mesh. Although no precise explanation could be found, it is possible that this imbalance stems from the type of variable transmitted by the coupling system. Since the data transfer from Fluent to Transient Structural transmits forces, it is possible that converting these forces into displacements using the hyperelastic model is computationally relatively costly, whereas Transient Structural transmits displacements to Fluent, which can be directly used as such.

If these computational costs were to increase in the course of future model development, resulting in unreasonably high computation times, adjustments would probably have to be made to reduce them. One potential solution is to use the system coupling's parallel computation tool. This tool enables the computational load to be distributed over several machines simultaneously, so that the computational power of each can be combined to give a greater total computational force. If this solution were to prove impossible or insufficient, the model would have to be thoroughly modified. One possible solution would be to use SHELL181 planar elements with virtual thickness to mesh the structural domain, despite their greater sensitivity to the problem of element distortion. Indeed, their use would probably enable the creation of a single fluid-structure interface instead of the current two, and thus reduce the complexity of the model.

6.2.3 Element distortion of the structural mesh

While the first two limitations of the model presented in Sections 6.2.1 and 6.2.2 are in fact difficulties that can be overcome, rather than real barriers, the error presented here is indeed prohibitive for the resolution of the model, and no solution has yet been found.

The problem presented here consists again in the structural domain mesh element distortion problem presented in Section 4.2.4, and the error message displayed by Ansys is the same as that shown in Figure 44, but the conditions under which it appears are different from those that led to the choice to increase pressure progressively. In fact, the error requiring a gradual increase in pressure appears as early as the first time step of the calculation, and indicates a problem in the application of static pressure. The case presented here is significantly different, since the distortion error of the structural domain mesh elements no longer appears at the first time step, but after 10 to 15% of model resolution. As it happens, this phase of the resolution corresponds to the phase where oscillations appear in tests carried out with larger time step sizes, as shown in red in Figure 66.
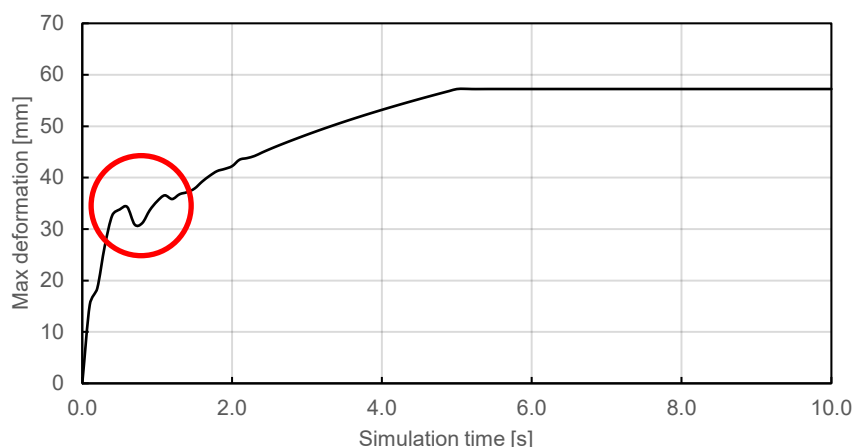
Figure 66: Evolution of the maximum out-of-plane deformation over time for test 3

One explanation for the appearance of this mesh element distortion error at this point in the resolution could be that the time step refinement enables oscillations occurring in this phase to be captured over their entire amplitude (c.f. Figure 42), and that this amplitude and therefore the displacement of the membrane between two consecutive time steps is such that it generates this mesh element distortion error.

If this explanation were to prove correct, it would have two consequences, one positive and the other negative. The first, positive, is that the constructed model does generate membrane vibrations, but its resolution simply doesn't allow to model them fully without error messages appearing. This means that if this problem of element distortion is solved, it is likely that it will be possible to characterize membrane vibrations properly.

The second consequence is rather negative. Indeed, since the deformations causing the error are induced indirectly by the boundary conditions of the model, it is much more difficult to implement mitigating measures to avoid the problem. For example, it is not possible to gradually increase these displacements, as was done for static pressure.

6.3   Further development paths

6.3.1 Resolution of the remaining problem

First and foremost, it is necessary to study in detail this problem of distortion of the mesh elements of the structural domain after just over a tenth of the resolution in order to finalize the model so that it is fully operational.

With this in mind, it might be interesting to run a calculation with a pressure of less than 1bar, so that this induces a maximum membrane deformation roughly equal to that for which oscillations seem to appear in Figure 66. If these oscillations of the maximum deformation do indeed correspond to membrane vibrations, then they should occur throughout the rest of the simulation, since the conditions favorable to their appearance are constant. This test would perhaps provide a better understanding of these oscillations, and enable to determine whether they are due to numerical divergence during resolution, or to real momentary vibrations of the membrane.

The results of this test must then be used to guide research into solving the distortion problem. In any case, solving this problem is likely to be highly technical, requiring advanced skills in numerical modeling software and considerable expertise in Ansys software. It may therefore be wise to get in touch with an Ansys expert, at least via the dedicated technical forums, or even better, to arrange an interview, in order to explain in detail the purpose of the modeling and the major problem encountered, so as to obtain advice from a professional in the field who knows the limitations of the software. Indeed, an outcome that has not yet been discussed could simply consist in the finding of the impossibility to proceed with the modeling as currently conceived. The model would then have to be simplified, for example by breaking it down into several simpler sub-models.

6.3.2 Systematic testing and comparison

If the element distortion problem can be solved and the model is working as it should, it is now possible to make final adjustments to the model. Particular attention must be paid to the choice of turbulence model and its influence on the results. Since, for the moment, a relatively simple turbulence model has been implemented, it would be interesting to test a more complex model, such as an LES model, in order to analyze the differences between the results provided by one and the other, and to determine whether a more complex model is necessary.

Once the model is fully configured, it is then possible to move on to the systematic testing phase. The aim of this phase is to quantify the dynamic behavior of the membranee, based on the results of several tests in which only the boundary conditions are changed. These results should, for example, make it possible to define the influence of pressure and velocity on the amplitude and frequency of any induced vibrations of the membrane.

In order to study the reliability and representativeness of the results provided by the numerical model developed, it could be very interesting to develop a physical laboratory model with the same geometric and material characteristics as those used for the numerical model. Comparing the results of the two models would then enable to give them greater credibility in the case of agreement, or to better calibrate the numerical model, in particular by refining the type of boundary conditions or material roughness in the case where the results should be different.

Chapter 7   Conclusion

The need to maintain and expand hydraulic structures is a major challenge for the coming energy transition, especially in Western countries. One technique already widespread allowing to meet these issues consists in the use of geomembranes to overcome problems of permeability or deterioration of traditional linings. A recent development is the use of these geomembranes, in the form of geomembrane systems, in pressure tunnels and penstocks in hydroelectric schemes to increase their productivity and durability. However, although a few applications have already been identified, little is known about the behavior of these geomembrane systems when faced with the high pressure and velocity flow that takes place in these pressure waterways and therefore very few technical recommendations are available for the installation of these systems. An in-depth study of the dynamic behavior of geomembrane systems when subjected to pressurized flow is therefore necessary to better understand how these systems interact with the flow, and in particular under what conditions membrane vibrations, potentially dangerous to the integrity of the structure, are likely to occur. With this in mind, a numerical model was built to provide answers to these questions.

This work has shown that one approach to numerically model this problem is to simulate in parallel the behavior of the fluid domain embodied by the flow and that of the structural domain embodied by the membrane by means of a two-way fluid-structure interaction. In this type of model, the influence of one domain on the other and vice versa is taken into account by the creation of exchange interfaces enabling data transfer between the two modules responsible for calculating each domain. This transfer of data between the two modules occurs throughout the resolution of the model and is managed by a third module, called system coupling, which is responsible for coordinating the computation process.

The geomembrane is made of a material known as hyperelastic, which does not follow the linear stress-strain curves that can generally be assumed for most conventional materials. To model the behavior of this material in the numerical software, a behavioral model needs to be selected and the results of solicitation tests imported. The material is thus defined using the Mooney-Rivlin model and the test results supplied by CarpiTech, a Swiss company specialized in geomembranes. Once the materials have been defined, it is necessary to discretize the solid and fluid domains using a mesh. The mesh of the membrane is particularly critical, as the mesh is subject to large displacements and the accuracy of the results depends directly on its quality. An analysis of the density of elements required to obtain a good convergence of results has thus been carried out, but does not allow to avoid certain mesh-related errors.

Indeed, this work has highlighted the difficulty of building a model to simulate the problem. Models implementing two-way fluid-structure interactions are inherently complex, but this complexity is further exacerbated in the case under study by the consideration of a hyperelastic material subjected to very high hydrostatic pressure. The complexity of the model is thus reflected in the computational costs of its resolution with calculation times of up to four days. But these high stresses are especially problematic for the mesh of the structural domain, which then encounters problems of element distortion, preventing the model from working under all the desired boundary conditions. These few residual problems do not allow to consider the construction of the model as a complete success, but the results presented above are encouraging and nonetheless bear witness to all the problems already solved.

References

Ali, A., Hosseini, M., Sahari, B.B., 2010. A Review of Constitutive Models for Rubber-Like Materials.

Ansys, 2023a. Ansys Mechanical Theory Reference.

Ansys, 2023b. Element Reference.

Ansys, 2023c. Ansys System Coupling User's Guide.

Ansys, 2021a. Ansys Fluent Theory Guide.

Ansys, 2021b. Ansys Fluent User's Guide.

Ansys, 2021c. System Coupling Tutorials.

Ansys Learning, 2020. Handling Element Distortion Errors in Hyperelastic Material Models Using Ansys Mechanical — Lesson 3 [WWW Document]. URL https://www.youtube.com/watch?v=fI2a_xP0veI (accessed 5.31.23).

Beatty, M.F., 1987. Topics in Finite Elasticity: Hyperelasticity of Rubber, Elastomers, and Biological Tissues—With Examples. Applied Mechanics Reviews 40, 1699–1734. https://doi.org/10.1115/1.3149545

Berga, L., 2016. The Role of Hydropower in Climate Change Mitigation and Adaptation: A Review. Engineering 2, 313–318. https://doi.org/10.1016/J.ENG.2016.03.004

Botelho, A., Ferreira, P., Lima, F., Pinto, L.M.C., Sousa, S., 2017. Assessment of the environmental impacts associated with hydropower. Renewable and Sustainable Energy Reviews 70, 896–904. https://doi.org/10.1016/j.rser.2016.11.271

Boyce, M.C., Arruda, E.M., 2000. Constitutive Models of Rubber Elasticity: A Review. Rubber Chemistry and Technology 73, 504–523. https://doi.org/10.5254/1.3547602

British Plastics Federation, 2023. Polyvinyl Chloride PVC [WWW Document]. British Plastics Federation. URL https://www.bpf.co.uk/plastipedia/polymers/PVC.aspx (accessed 5.23.23).

Cazzuffi, D., Giroud, J.-P., Scuero, A., Vaschetti, G., 2012a. Cinquante ans de différentes applications des géomembranes dans les barrages: Sciences Eaux & Territoires Numéro 8, 2–13. https://doi.org/10.3917/set.008.002

Cazzuffi, D., Giroud, J.-P., Scuero, A., Vaschetti, G., 2010. Geosynthetic barriers systems for dams.

Cazzuffi, D., Scuero, A., Vaschetti, G., 2012b. Hydraulic tunnels, in: Handbook of Geosynthetic Engineering: Geosynthetics and Their Applications. ICE, London, pp. 303–315.

Chagnon, G., Marckmann, G., Verron, E., 2004. A Comparison of the Hart-Smith Model with Arruda-Boyce and Gent Formulations for Rubber Elasticity. Rubber Chemistry and Technology 77, 724–735. https://doi.org/10.5254/1.3547847

Chang, T.Y.P., Saleeb, A.F., Li, G., 1991. Large strain analysis of rubber-like materials based on a perturbed Lagrangian variational principle. Computational Mechanics 8, 221–233. https://doi.org/10.1007/BF00577376

Chimakurthi, S.K., Reuss, S., Tooley, M., Scampoli, S., 2018. ANSYS Workbench System Coupling: a state-of-the-art computational framework for analyzing multiphysics problems. Engineering with Computers 34, 385–411. https://doi.org/10.1007/s00366-017-0548-4

Enzinger, N., Cerjak, H., 2006. Investigation of cracks in original material of Cleuson-Dixence shaft. Science and Technology of Welding and Joining 11, 347–351. https://doi.org/10.1179/174329306X113244

Feynman, R.P. (Richard P., 1918-1988, 1964. The Feynman lectures on physics. Reading, Mass. : Addison-Wesley Pub. Co., c1963-1965.

Gascón-Pérez, M., 2017. Acoustic Influence on the Vibration of a Cylindrical Membrane Drum Filled with a Compressible Fluid. Int. J. Appl. Mechanics 09, 1750072. https://doi.org/10.1142/S1758825117500727

Giroud, J.P., 2016. Leakage Control using Geomembrane Liners. S&R 39, 213–235. https://doi.org/10.28927/SR.393213

Giroud, J.P., 1984. Geotextiles and Geomembranes.

Giroud, J.-P., Perfetti, J., 1977. Classification of fabrics and measurement of their properties with a view to utilisation in geotechnics.

Greiner, W., 2010. The Vibrating Membrane. https://doi.org/10.1007/978-3-642-03434-3_10

Hager, W.H., Castro-Orgaz, O., 2017. William Froude and the Froude Number. J. Hydraul. Eng. 143, 02516005. https://doi.org/10.1061/(ASCE)HY.1943-7900.0001213

Hettich, R., Haaren, E., Ries, M., Still, G., 1987. Accurate Numerical Approximations of Eigenfrequencies and Eigenfunctions of Elliptic Membranes. ZAMM - Journal of Applied Mathematics and Mechanics / Zeitschrift für Angewandte Mathematik und Mechanik 67, 589–597. https://doi.org/10.1002/zamm.19870671201

ICOLD, the International Comission on Large Dams, 2010. Bulletin 135. Geomembrane sealing systems for dams. Innov. Infrastruct. Solut.

Intel, 2023. Processeur Intel® Xeon® Gold 6142 [WWW Document]. Intel. URL https://www.intel.fr/content/www/fr/fr/products/sku/120487/intel-xeon-gold-6142-processor-22m-cache-2-60-ghz/specifications.html (accessed 6.13.23).

International Energy Agency, 2021. Hydropower Special Market Report: Analysis and forecast to 2030. OECD. https://doi.org/10.1787/07a7bac8-en

International Hydropower Association, 2023. Hydropower 2050: Identifying the next 850+ GW towards Net Zero.

International Hydropower Association, 2022. 2022 Hydropower Status Report.

Khaniki, H.B., Ghayesh, M.H., Chin, R., Amabili, M., 2022. A review on the nonlinear dynamics of hyperelastic structures. Nonlinear Dyn 110, 963–994. https://doi.org/10.1007/s11071-022-07700-3

Korochkina, T., Claypole, T., Gethin, D.T., 2017. Choosing constitutive models for elastomers used in printing processes. pp. 431–435. https://doi.org/10.1201/9781315140216-71

Lestuzzi, P., Smith, I., 2019. Dynamique des structures. Bases et applications pour le génie civil.

Li, G., Jaiman, R.K., Khoo, B.C., 2021. Flow-excited membrane instability at moderate Reynolds numbers. arXiv:2011.11422 [physics].

Manik, G., Kalia, S., Verma, O.P., Sharma, T.K. (Eds.), 2023. Recent Advances in Mechanical Engineering: Select Proceedings of CAMSE 2021, Lecture Notes in Mechanical Engineering. Springer Nature Singapore, Singapore. https://doi.org/10.1007/978-981-19-2188-9

Marence, M., Lilliu, G., Lemke, S., 2020. Composite membrane lining in pressure tunnels and shafts: design practice and new possibilities.

Mathieu, É., 1868. Mémoire sur le mouvement vibratoire d'une membrane de forme elliptique.

Melly, S.K., Liu, L., Liu, Y., Leng, J., 2021. A review on material models for isotropic hyperelasticity. Int Journal of Mech Sys Dyn 1, 71–88. https://doi.org/10.1002/msd2.12013

Menter, F.R., 1994. Two-equation eddy-viscosity turbulence models for engineering applications. AIAA Journal 32, 1598–1605. https://doi.org/10.2514/3.12149

Mooney, M., 1940. A Theory of Large Elastic Deformation. Journal of Applied Physics 11, 582–592. https://doi.org/10.1063/1.1712836

Moran, E.F., Lopez, M.C., Moore, N., Müller, N., Hyndman, D.W., 2018. Sustainable hydropower in the 21st century. Proc. Natl. Acad. Sci. U.S.A. 115, 11891–11898. https://doi.org/10.1073/pnas.1809426115

Nogueira, H.I.S., Pfister, M., Schleiss, A.J., 2016. Approaches to Reduce Friction Losses in Headrace Waterways of Hydropower Plants. J. Hydraul. Eng. 142, 02516001. https://doi.org/10.1061/(ASCE)HY.1943-7900.0001123

Ormiston, R.A., 1971. Theoretical and experimental aerodynamics of the sailwing. Journal of Aircraft 8, 77–84. https://doi.org/10.2514/3.44232

Perera, D., Smakhtin, V., Williams, S., North, T., Curry, A., 2021. Ageing Water Storage Infrastructure: An Emerging Global Risk. United Nations University Institute for Water, Environment and Health. https://doi.org/10.53328/QSYL1281

Plaut, R.H., Cotton, S.A., 2005. Two-dimensional vibrations of air-filled geomembrane tubes resting on rigid or deformable foundations. Journal of Sound and Vibration 282, 265–276. https://doi.org/10.1016/j.jsv.2004.02.032

Quaranta, E., Aggidis, G., Boes, R.M., Comoglio, C., De Michele, C., Ritesh Patro, E., Georgievskaia, E., Harby, A., Kougias, I., Muntean, S., Pérez-Díaz, J., Romero-Gomez, P., Rosa-Clot, M., Schleiss, A.J., Vagnoni, E., Wirth, M., Pistocchi, A., 2021. Assessing the energy potential of modernizing the European hydropower fleet. Energy Conversion and Management 246, 114655. https://doi.org/10.1016/j.enconman.2021.114655

Rawal, A., Shah, T.H., Anand, S.C., 2016. Geotextiles in civil engineering, in: Handbook of Technical Textiles. Elsevier, pp. 111–133. https://doi.org/10.1016/B978-1-78242-465-9.00004-5

Rivlin, R.S., 1948. Large elastic deformations of isotropic materials IV. further developments of the general theory. Phil. Trans. R. Soc. Lond. A 241, 379–397. https://doi.org/10.1098/rsta.1948.0024

Ruzicka, M.C., 2008. On dimensionless numbers. Chemical Engineering Research and Design 86, 835–868. https://doi.org/10.1016/j.cherd.2008.03.007

Scuero, A., Vaschetti, G., 2021. Geomembranes to Line Surge Shafts, in: Shehata, H., Badr, M. (Eds.), Advancements in Geotechnical Engineering, Sustainable Civil Infrastructures. Springer International Publishing, Cham, pp. 106–120. https://doi.org/10.1007/978-3-030-62908-3_8

Scuero, A., Vaschetti, G., 2017. Geomembrane sealing systems for dams: ICOLD Bulletin 135. Innov. Infrastruct. Solut. 2, 29. https://doi.org/10.1007/s41062-017-0089-0

Shukla, S.K., Yin, J.-H. (Eds.), 2006. Fundamentals of geosynthetic engineering, Proceedings and monographs in engineering, water and earth sciences. Taylor & Francis/Balkema, London ; New York.

Swiss Federal Office of Energy, 2019. Potentiel hydroélectrique de la Suisse.

Tiomkin, S., Raveh, D.E., 2021. A review of membrane-wing aeroelasticity. Progress in Aerospace Sciences 126, 100738. https://doi.org/10.1016/j.paerosci.2021.100738

Troesch, B.A., 1973. Elliptical Membranes with Smallest Second Eigenvalue.

Vaschetti, G., 2022. Geomembranes in Dam Engineering.

Vorlet, S., De Cesare, G., 2023. A comprehensive review on geomembrane systems application in hydropower and pressure waterways. Renewable and Sustainable Energy Reviews (under review).

Wendt, J.F., Anderson, J.D., Von Karman Institute for Fluid Dynamics (Eds.), 2008. Computational fluid dynamics: an introduction, 3rd ed. ed. Springer, Berlin ; [London].

Wex, C., Arndt, S., Stoll, A., Bruns, C., Kupriyanova, Y., 2015. Isotropic incompressible hyperelastic models for modelling the mechanical behaviour of biological tissues: a review. Biomedical Engineering / Biomedizinische Technik 60. https://doi.org/10.1515/bmt-2014-0146

Wiggert, D.C., Tijsseling, A.S., 2001. Fluid transients and fluid-structure interaction in flexible liquid-filled piping. Applied Mechanics Reviews 54, 455–481. https://doi.org/10.1115/1.1404122

Zhou-Lian, Z., Chang-Jiang, L., Xiao-Ting, H., Shan-Lin, C., 2009. Free Vibration Analysis of Rectangular Orthotropic Membranes in Large Deflection. Mathematical Problems in Engineering 2009, 1–9. https://doi.org/10.1155/2009/634362

Appendix

Analysis of maximum pressure increment for meshes with SOLID285 and SHELL181 elements

Table 15: Analysis of maximum pressure increment for meshes with SOLID285 and SHELL181 elements

Characteristic	SOLID285	SHELL181
Number of elements	68'588	11'963
Number of nodes	18'651	12'616
Degrees of freedom per node	3	6
Total degrees of freedom	55'963	75'696
Body sizing [mm]	10	8
Degree of refinement [-]	2	3
Number of elements through the thickness at the membrane edeges [-]	3	1 (by def)
Maximal pressure for 1 time step [bar]	0.03	0.01
Computation time for 1 time step [s]	14	8
Maximal pressure for 10 time steps [bar]	0.30	0.11
Computation time for 10 time steps [s]	43	24
Maximal pressure for 100 time steps [bar]	3.08	1.10
Computation time for 100 time steps [s]	314	140
Total deformation for 1bar with 100 time steps [mm]	57.4	57.3
Max equivalent strain for 1bar with 100 time steps [-]	0.255	0.238

Results for test 1

Hydraulic results
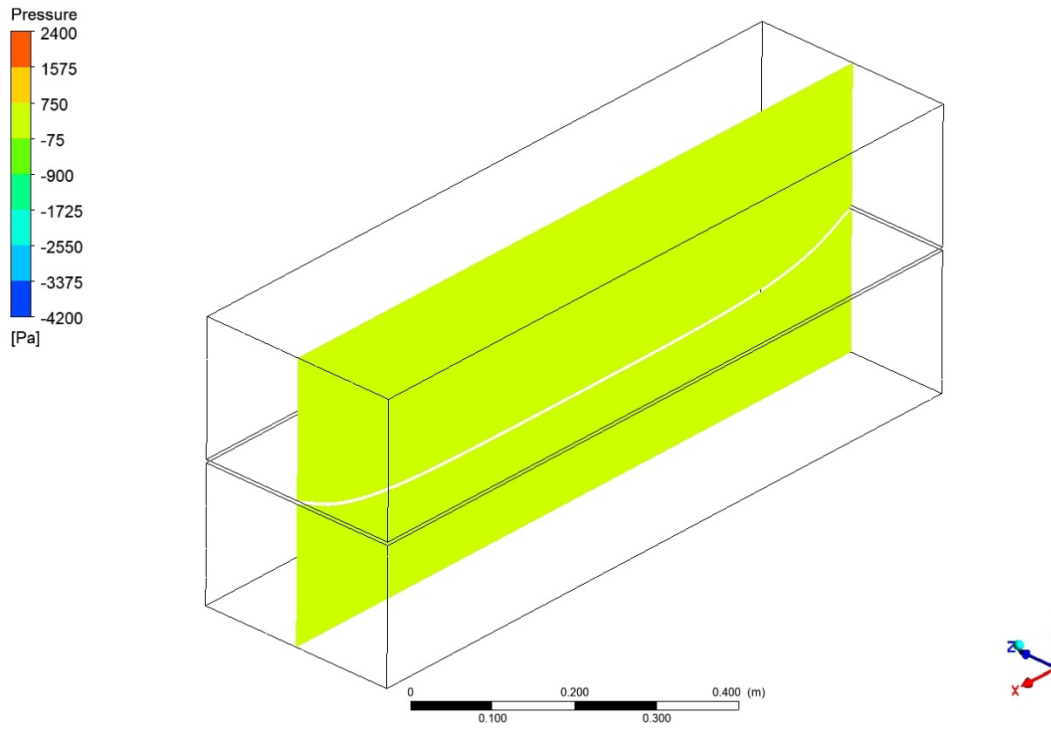
Figure 67: Hydrodynamic pressure [Pa] in the XY plane at *t*=10s for test 1
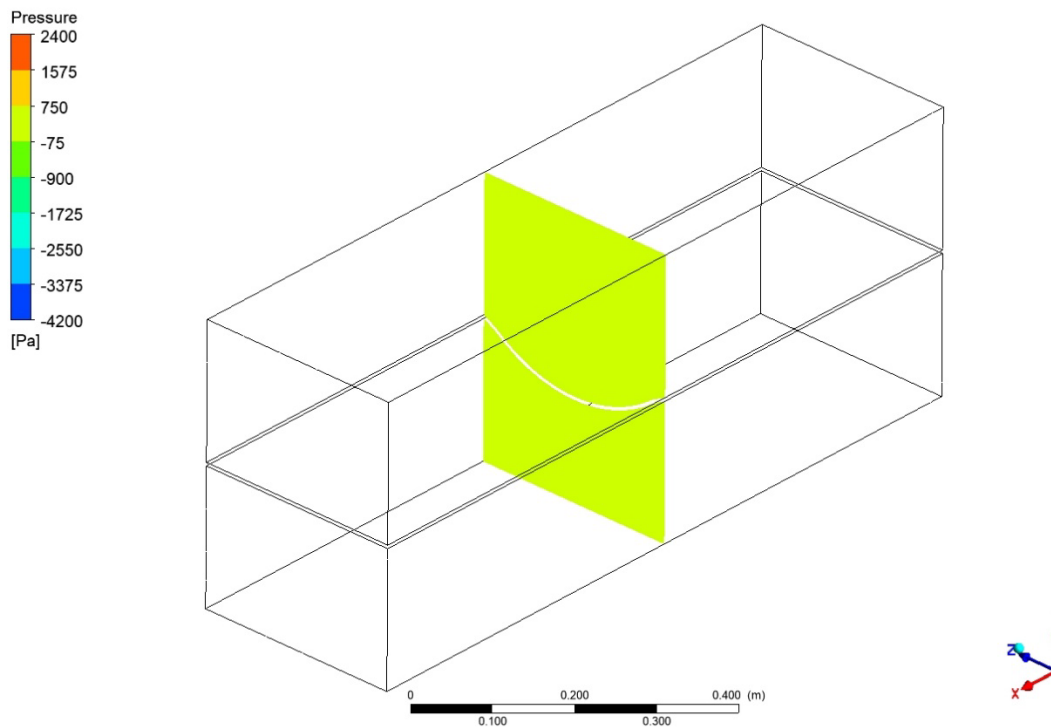
Figure 68: Hydrodynamic pressure [Pa] in the YZ plane at *t*=10s for test 1
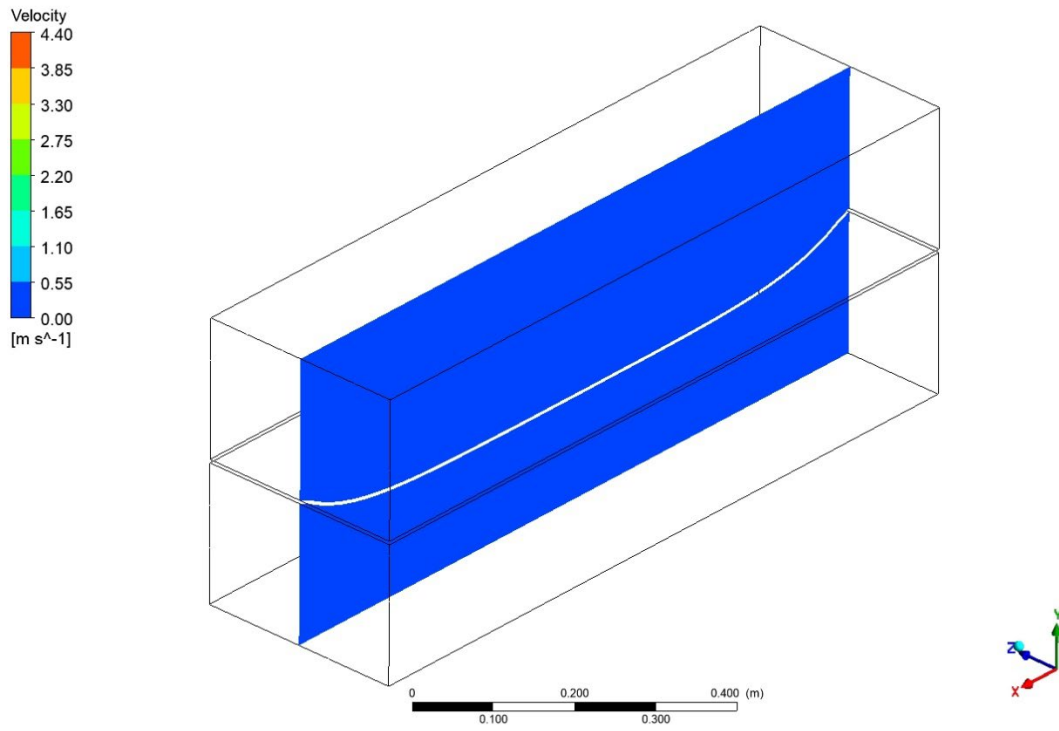
Figure 69: Water velocity [m/s] in the XY plane at *t*=10s for test 1
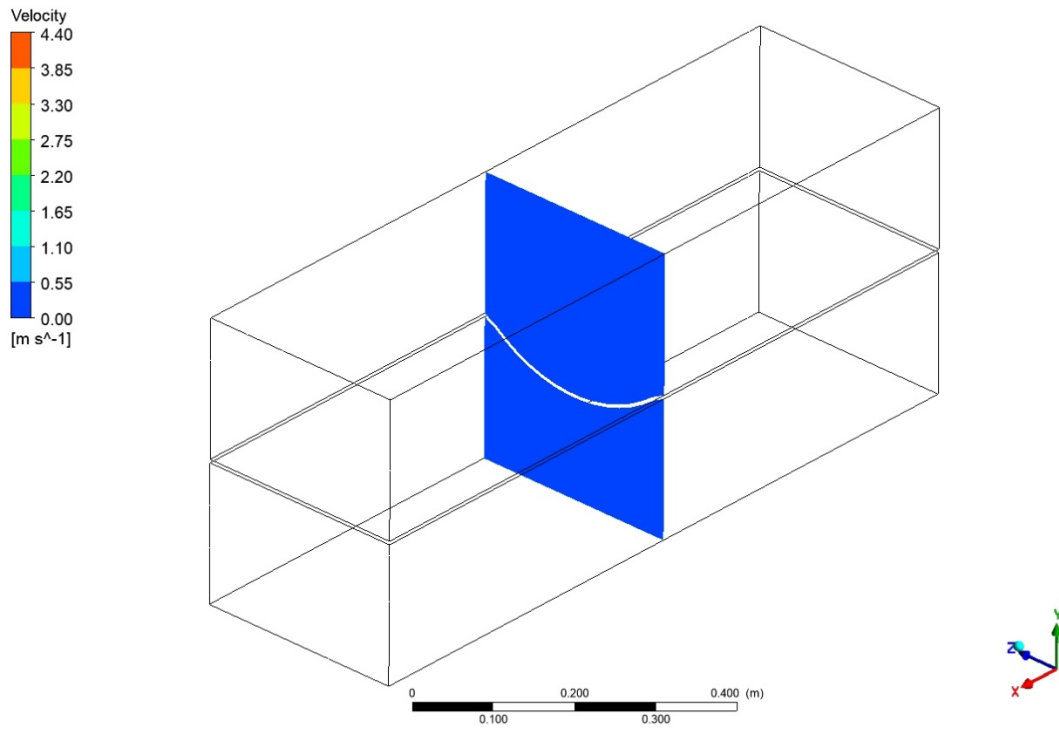
Figure 70: Water velocity [m/s] in the YZ plane at *t*=10s for test 1
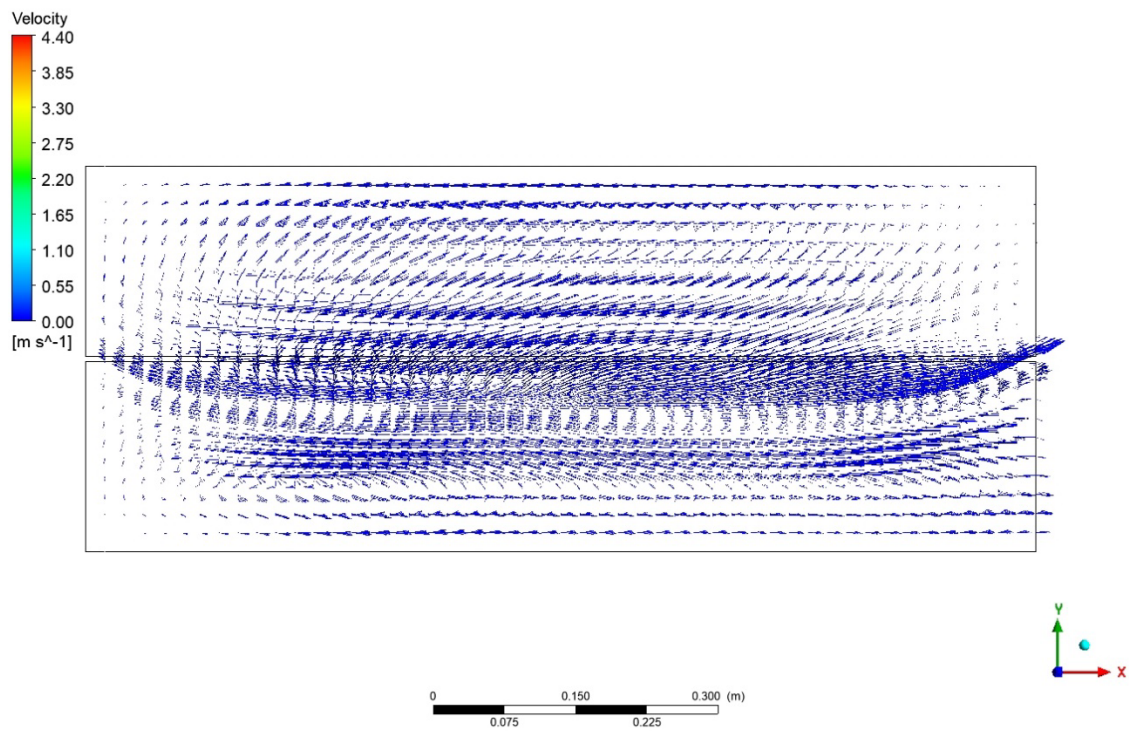
Figure 71: Velocity vectors [m/s] in the XY plane at *t*=10s for test 1

Structural results

C: Transient Structural
Total Deformation
Type: Total Deformation
Unit: mm
Time: 10, s
Max: 56,759
Min: 0
Deformation Scale Factor: 2,

72
64
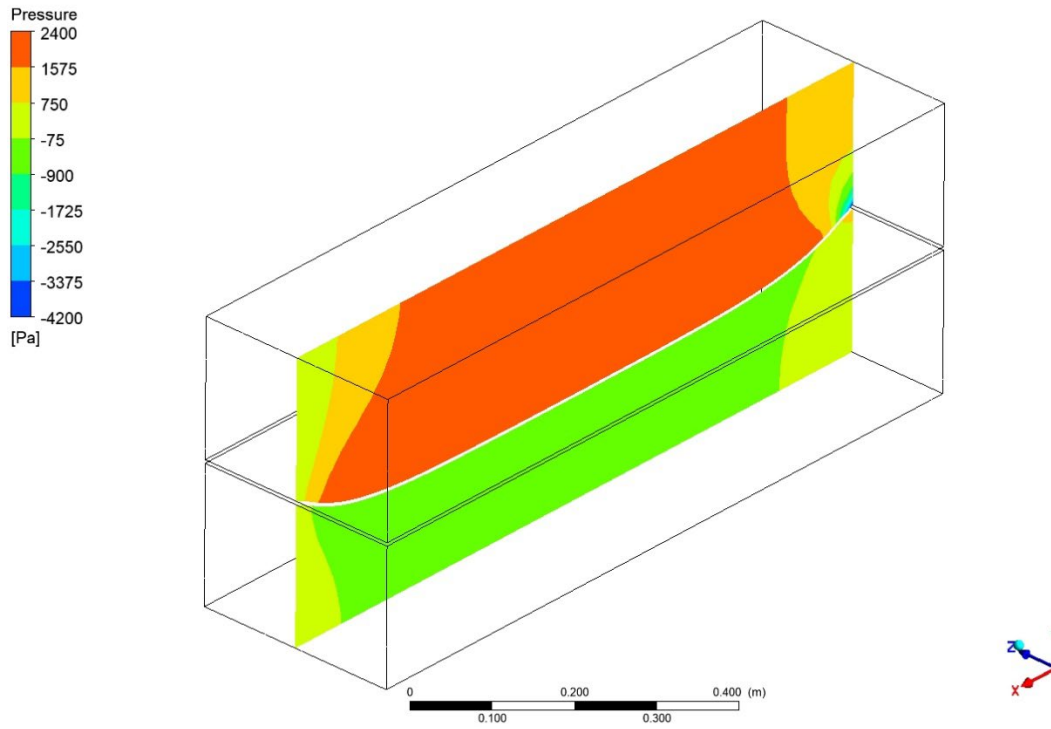56
48
40
32
24
16
8
0
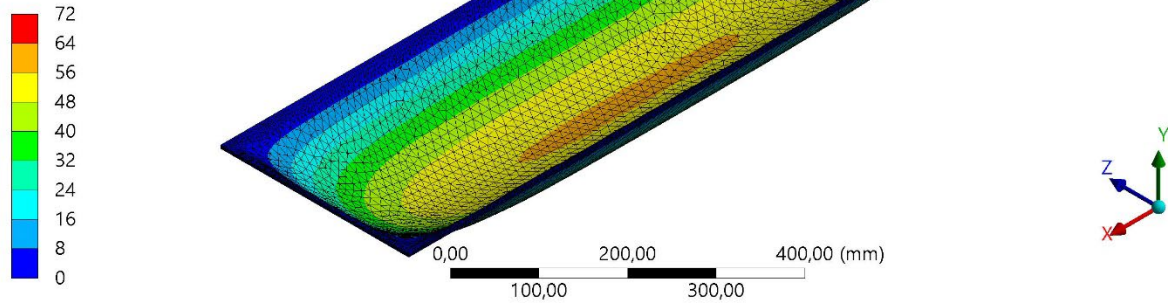
Figure 72: Geomembrane out-of-plane deformations [mm] at *t*=10s with a deformation scale factor of 2 for test 1

C: Transient Structural
Total Deformation
Type: Total Deformation
Unit: mm
Time: 10, s
Max: 56,759
Min: 0
Deformation Scale Factor: 0.0 (Undeformed)

72
64
56
48
40
32
24
16
8
0
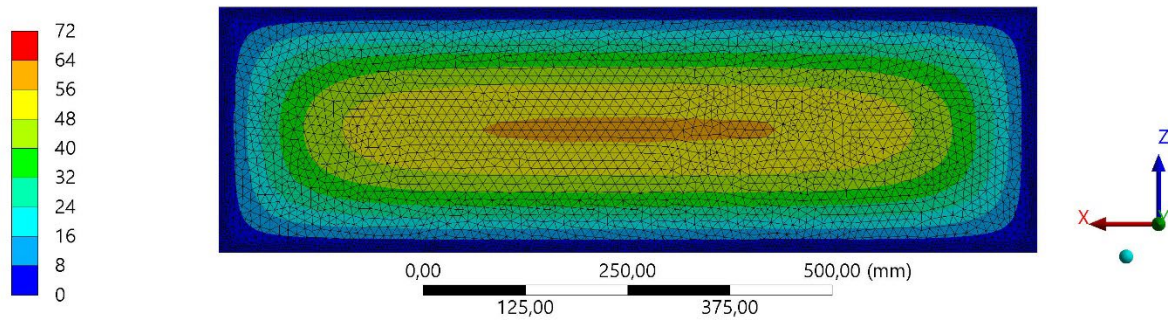
Figure 73: Plan view of geomembrane out-of-plane deformations at *t*=10s in the undeformed state for test 1

C: Transient Structural
Equivalent Stress
Type: Equivalent (von-Mises) Stress
Unit: MPa
Time: 10, s
Max: 22,383
Min: 0,27001
Deformation Scale Factor: 2,

45
40
35
30
25
20
15
10
5
0

0,00   200,00   400,00 (mm)
     100,00   300,00
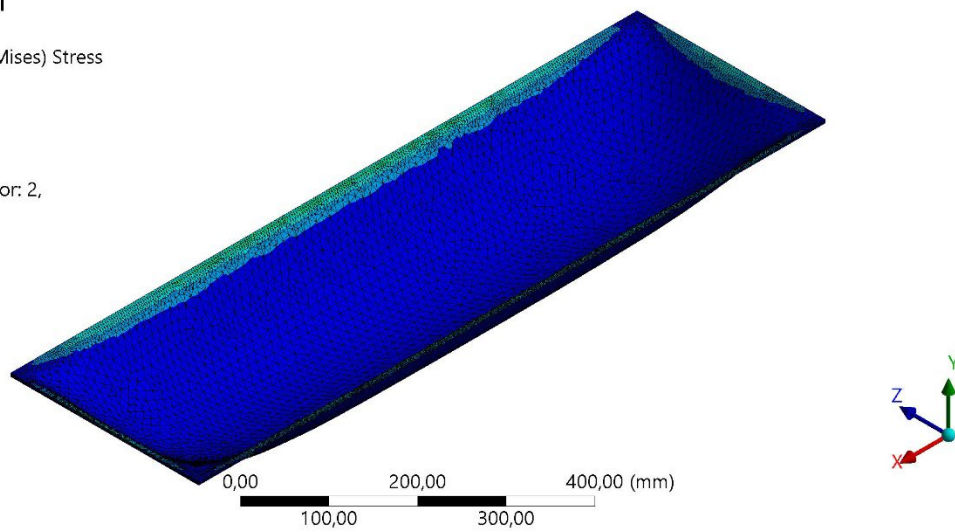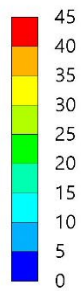
Figure 74: Geomembrane stresses [MPa] at *t*=10s with a deformation scale factor of 2 for test 1

C: Transient Structural
Equivalent Elastic Strain
Type: Equivalent Elastic Strain
Unit: mm/mm
Time: 10, s
Max: 0,25412
Min: 0,010755
Deformation Scale Factor: 2,

0,36
0,32
0,28
0,24
0,2
0,16
0,12
0,08
0,04
0

0,00   200,00   400,00 (mm)
     100,00   300,00
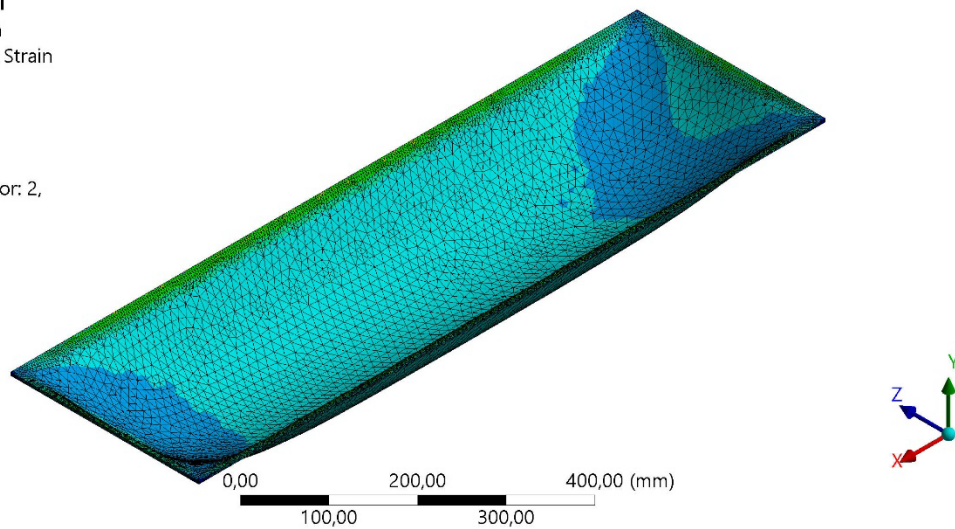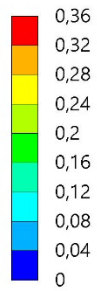
Figure 75: Geomembrane strains [-] at *t*=10s with a deformation scale factor of 2 for test 1

C: Transient Structural
Strain Energy
Type: Strain Energy
Unit: mJ
Time: 10, s
Max: 35,716
Min: 0,0030423
Deformation Scale Factor: 2,

85
76,5
68
59,5
51
42,5
34
25,5
17
8,5
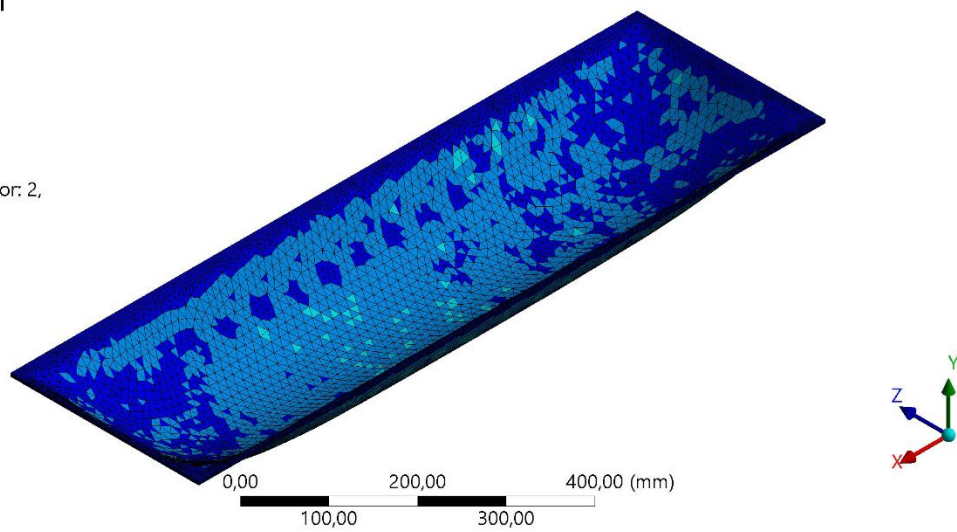
Figure 76: Geomembrane strain energy [mJ] at t=10s with a deformation scale factor of 2 for test 1
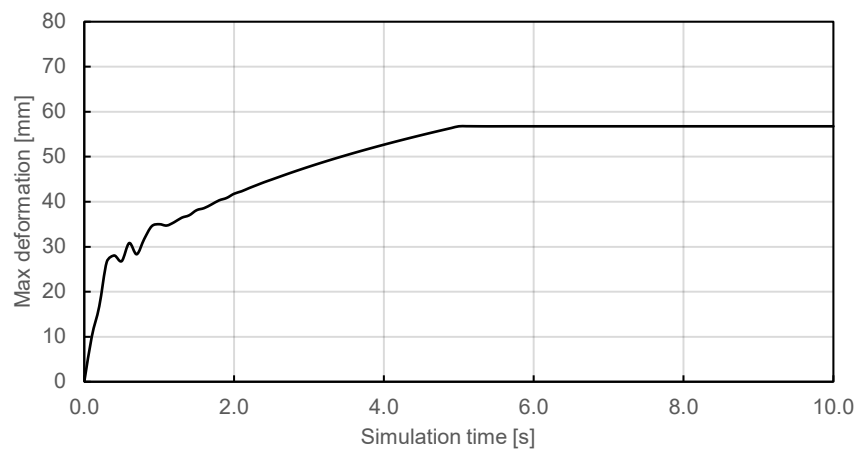
Figure 77: Evolution of the maximum out-of-plane deformation of the geomembrane over time for test 1
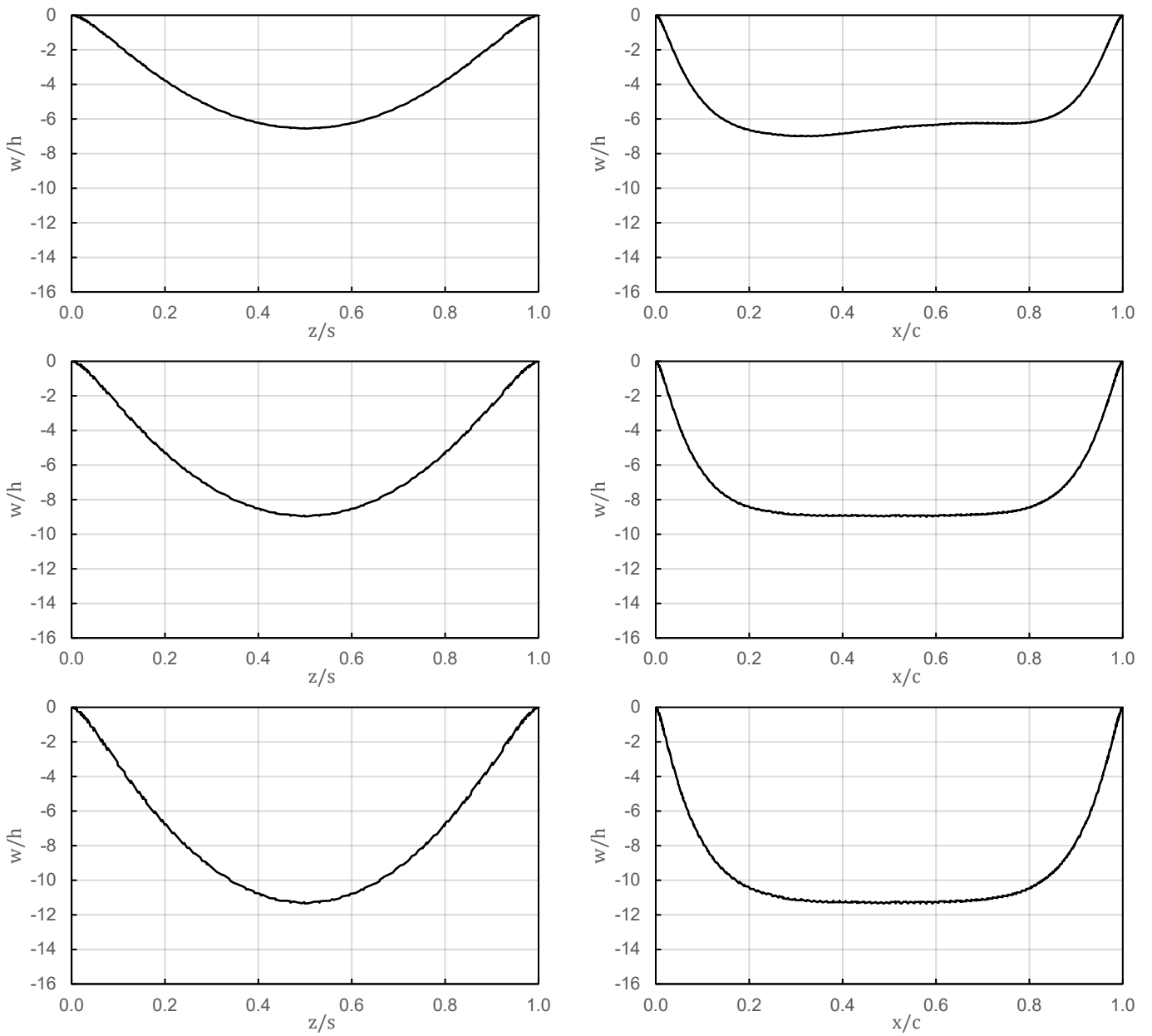
Figure 78: Cross-sections of geomembrane out-of-plane deformation in YZ plane (section cut) for the left column and XY plane (longitudinal cut) for the right column at times t=1s for the first row, t=2.5s for the second row and t=10s for the third row for test 1

Results for test 2

Hydraulic results
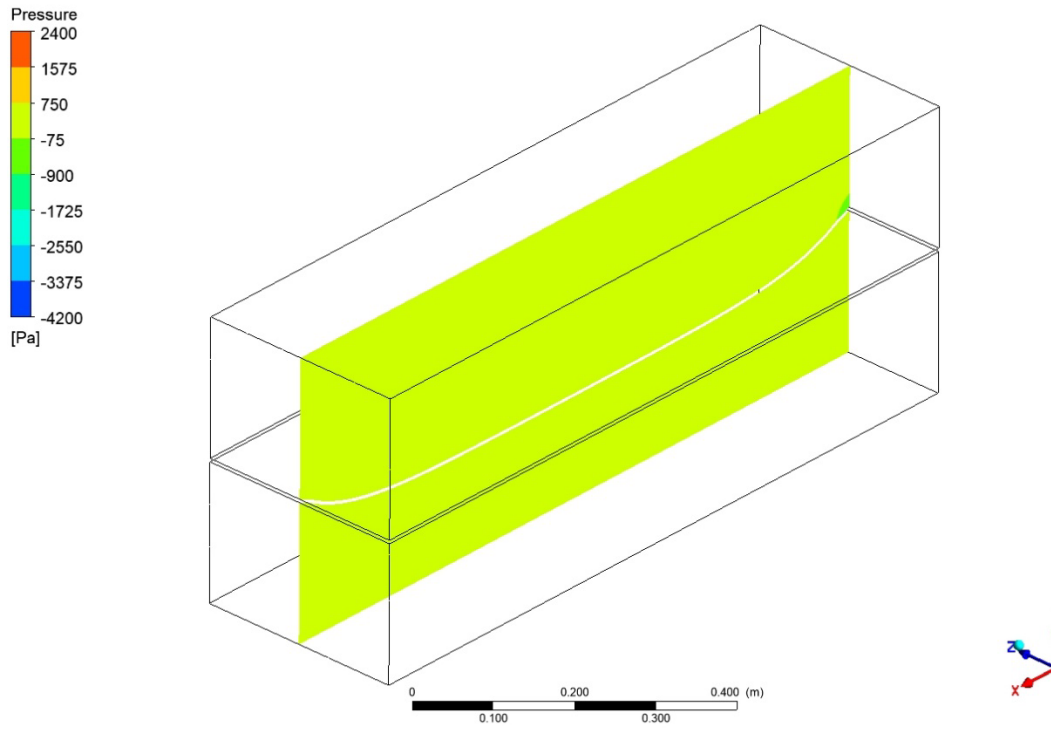
Figure 79: Hydrodynamic pressure [Pa] in the XY plane at *t*=10s for test 2
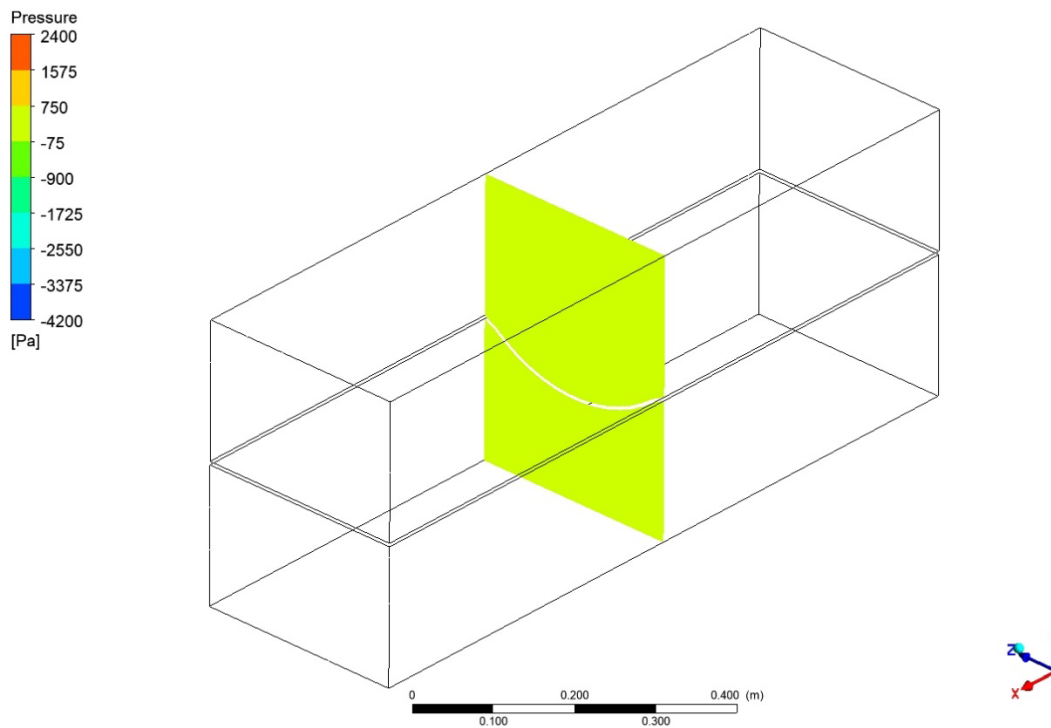
Figure 80: Hydrodynamic pressure [Pa] in the YZ plane at *t*=10s for test 2
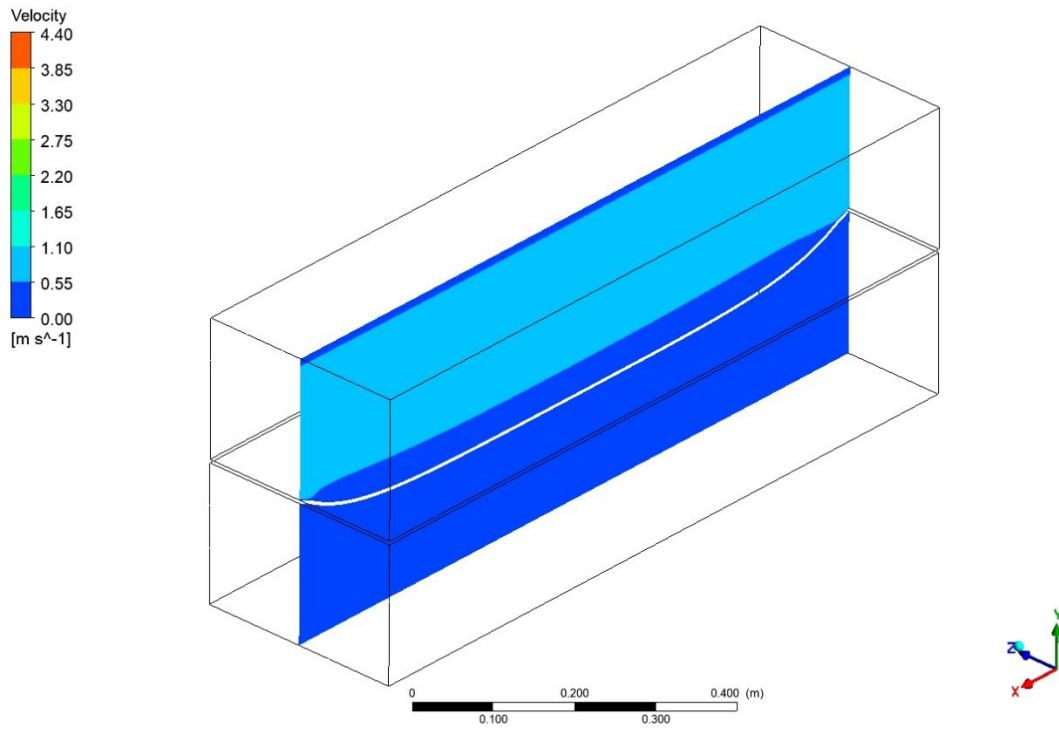
Figure 81: Water velocity [m/s] in the XY plane at *t*=10s for test 2
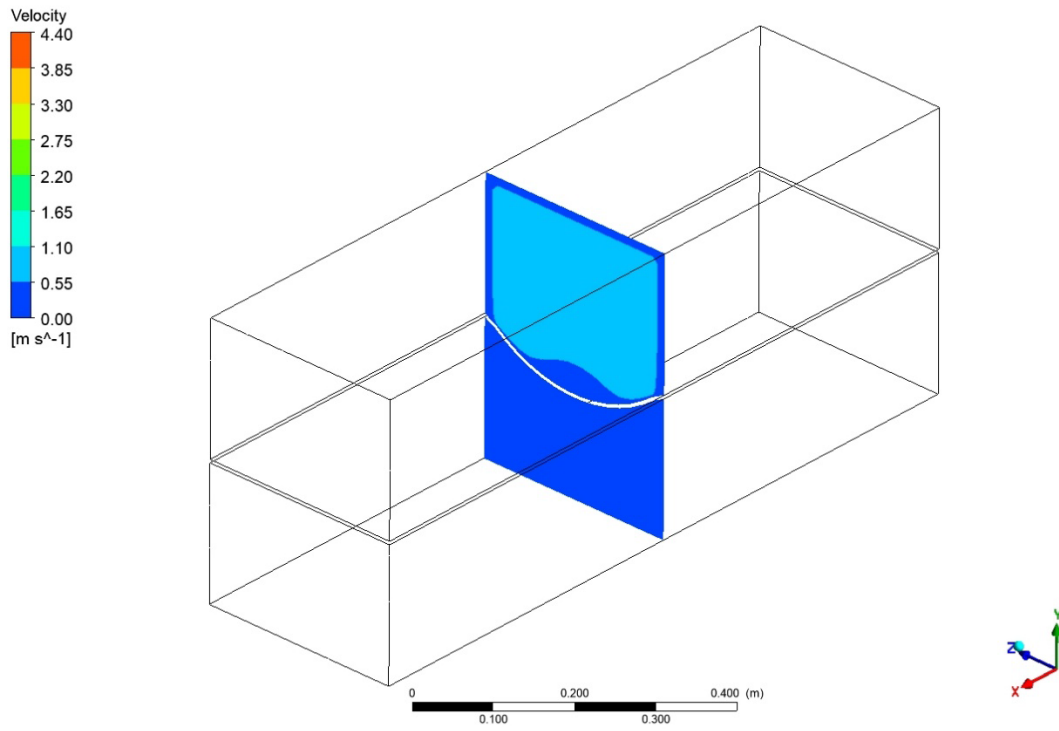
Figure 82: Water velocity [m/s] in the YZ plane at *t*=10s for test 2

X
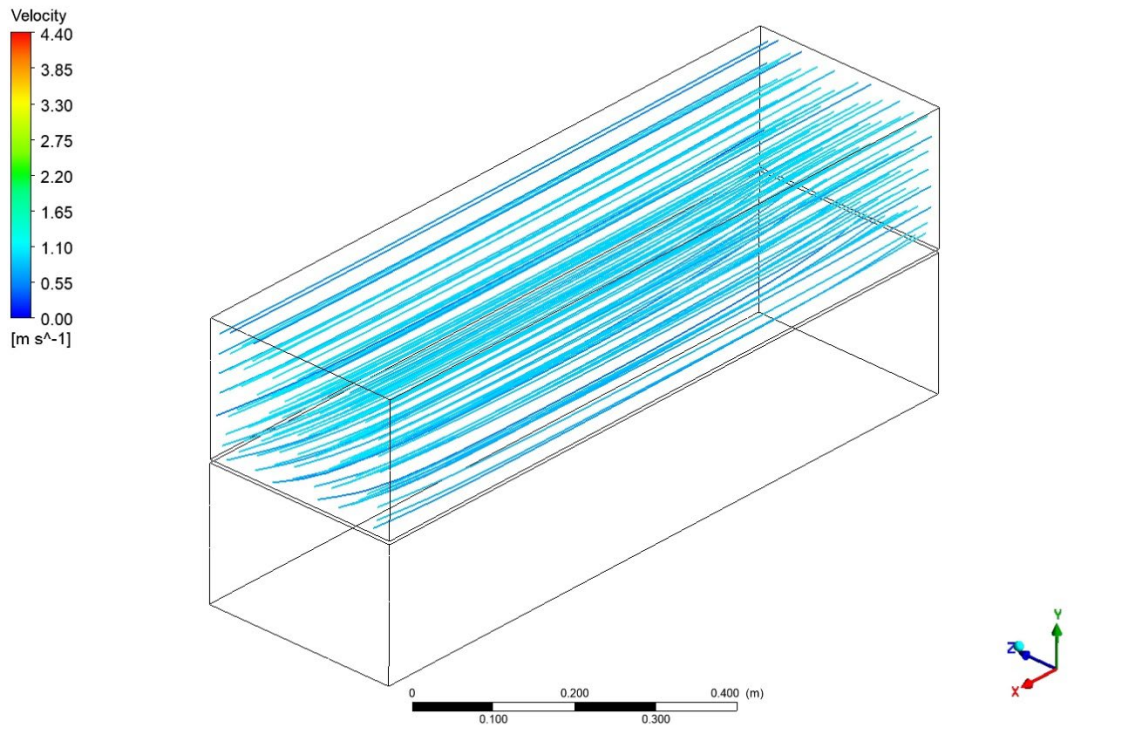
Figure 83: Streamlines [m/s] at *t*=10s for test 2
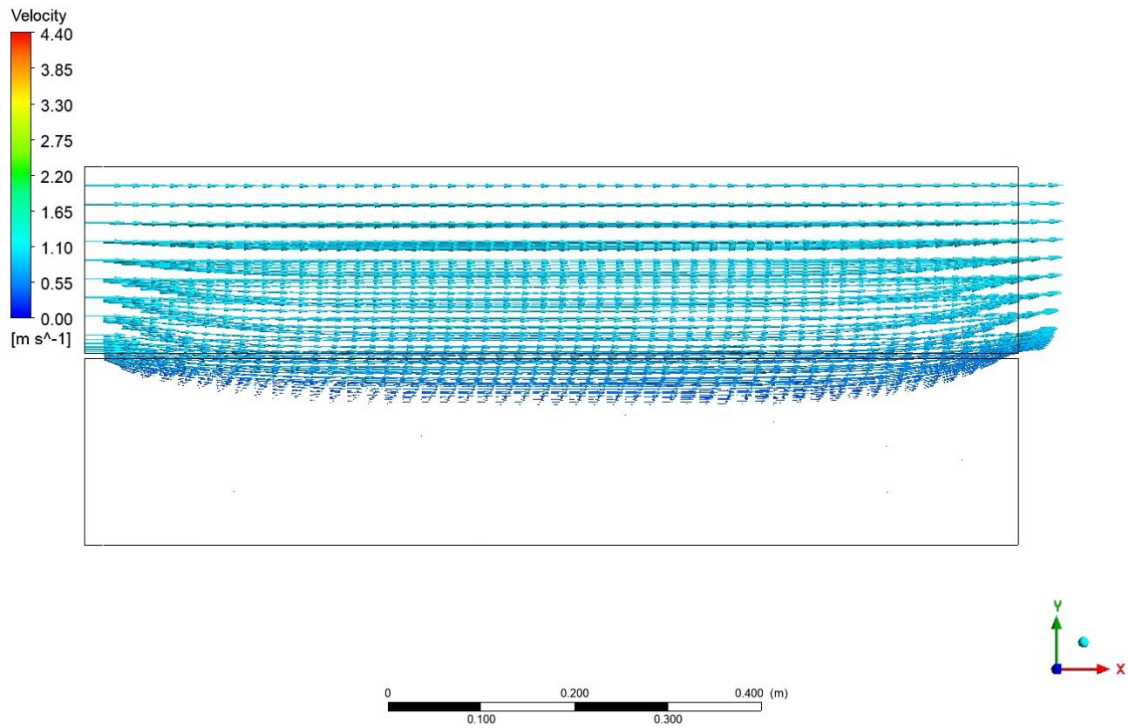
Figure 84: Velocity vectors [m/s] in the XY plane at *t*=10s for test 2

Structural results

C: Transient Structural
Total Deformation
Type: Total Deformation
Unit: mm
Time: 10, s
Max: 56,787
Min: 0
Deformation Scale Factor: 2,

72	
64	
56	
48	
40	
32	
24	
16	
8	
0	

0,00   200,00   400,00 (mm)
100,00   300,00
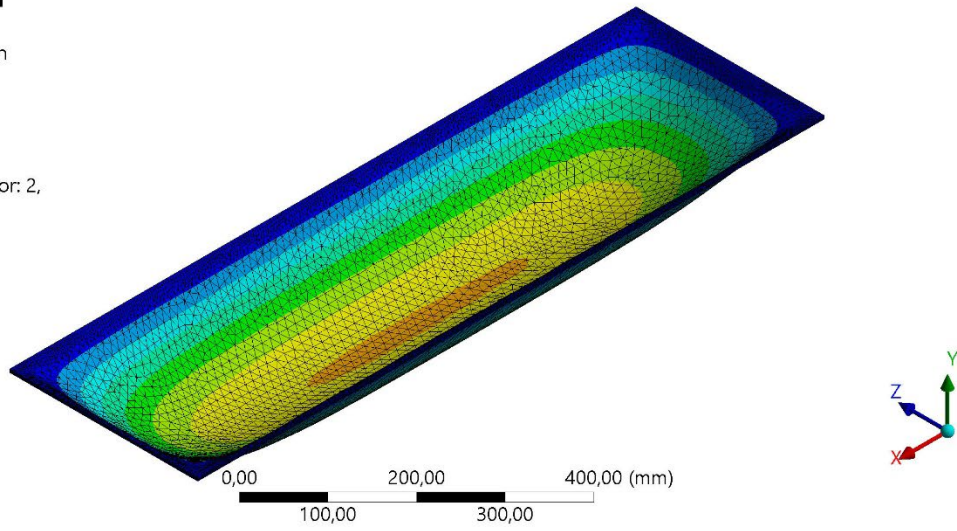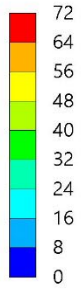
Figure 85: Geomembrane out-of-plane deformations [mm] at *t*=10s with a deformation scale factor of 2 for test 2

C: Transient Structural
Total Deformation
Type: Total Deformation
Unit: mm
Time: 10, s
Max: 56,787
Min: 0
Deformation Scale Factor: 0.0 (Undeformed)

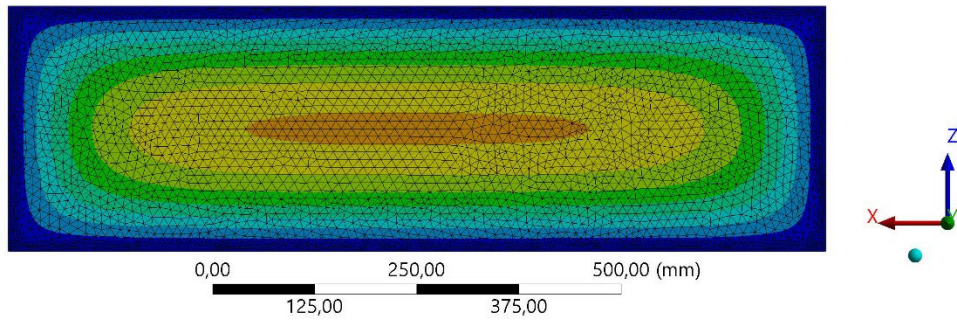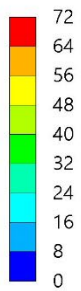|	
72	
64	
56	
48	
40	
32	
24	
16	
8	
0	

0,00   250,00   500,00 (mm)
125,00   375,00
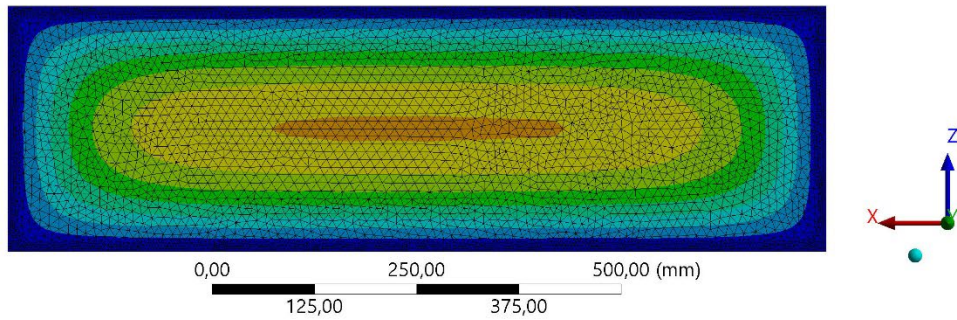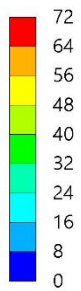
Figure 86: Plan view of geomembrane out-of-plane deformations at *t*=10s in the undeformed state for test 2

C: Transient Structural
Equivalent Stress
Type: Equivalent (von-Mises) Stress
Unit: MPa
Time: 10, s
Max: 22,411
Min: 0,27052
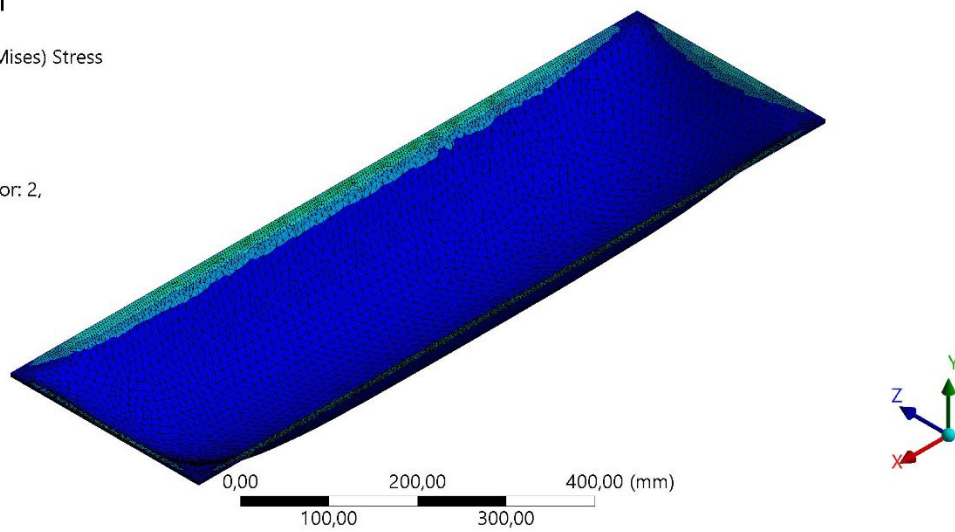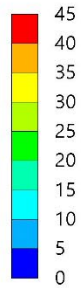Deformation Scale Factor: 2,

45
40
35
30
25
20
15
10
5
0
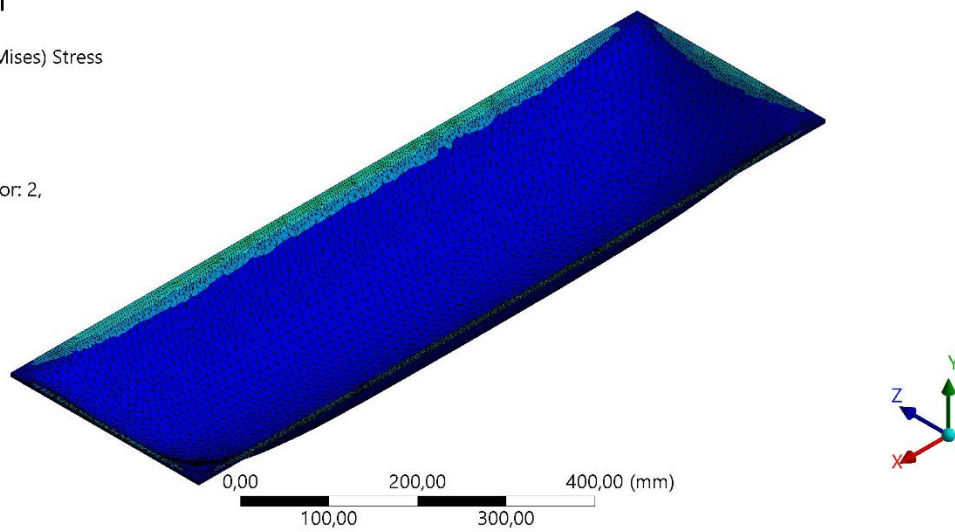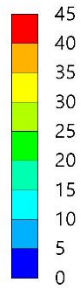
Figure 87: Geomembrane stresses [MPa] at t=10s with a deformation scale factor of 2 for test 2

C: Transient Structural
Equivalent Elastic Strain
Type: Equivalent Elastic Strain
Unit: mm/mm
Time: 10, s
Max: 0,25337
Min: 0,010779
Deformation Scale Factor: 2,

0,36
0,32
0,28
0,24
0,2
0,16
0,12
0,08
0,04
0
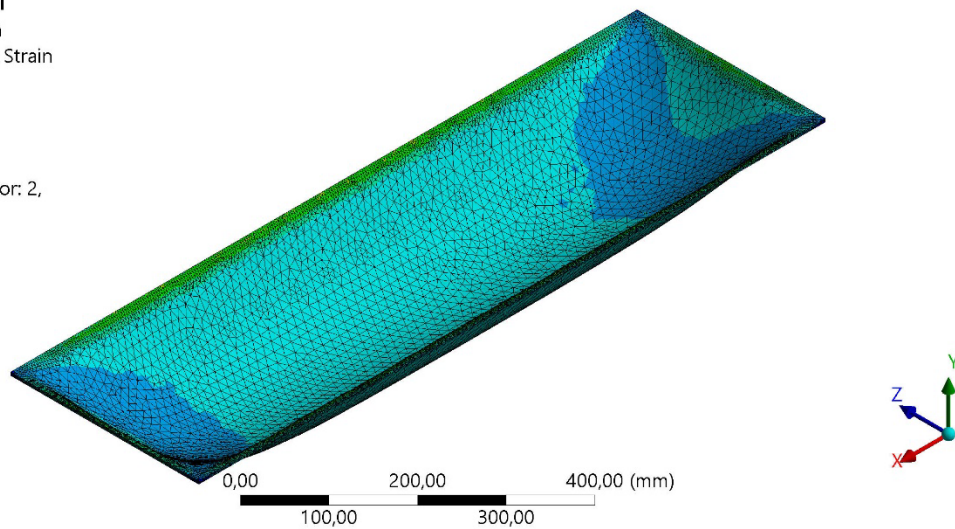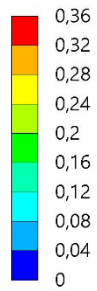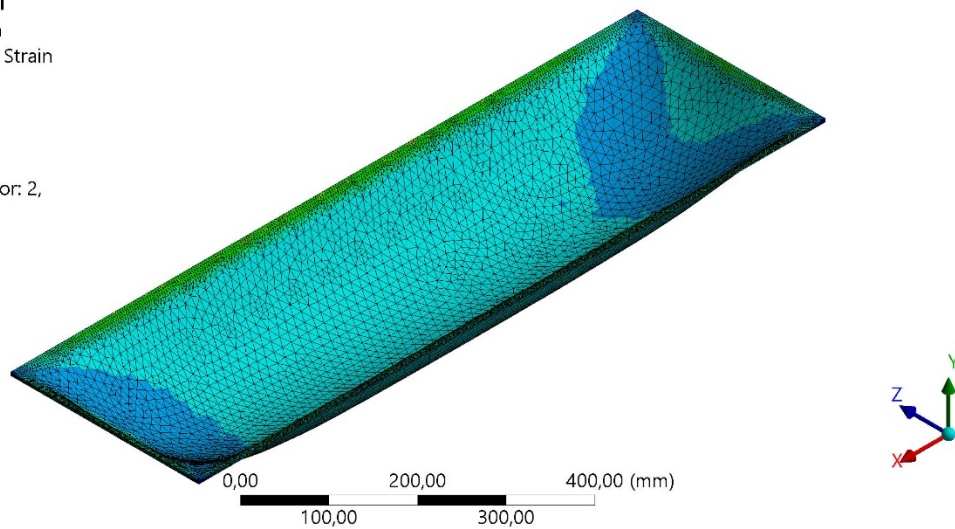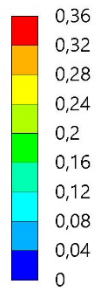
Figure 88: Geomembrane strains [-] at t=10s with a deformation scale factor of 2 for test 2

C: Transient Structural
Strain Energy
Type: Strain Energy
Unit: mJ
Time: 10, s
Max: 35,777
Min: 0,0030536
Deformation Scale Factor: 2,

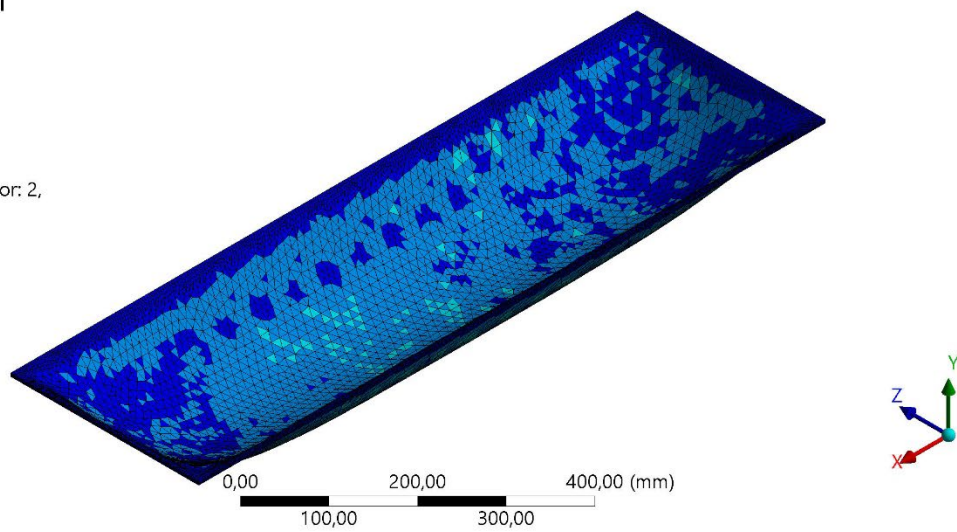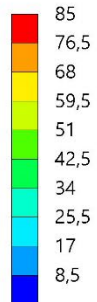85
76,5
68
59,5
51
42,5
34
25,5
17
8,5
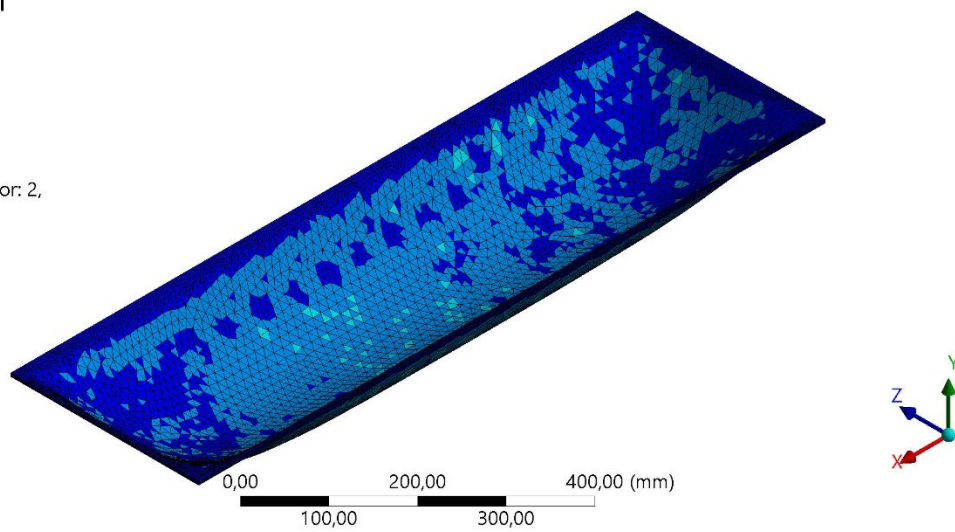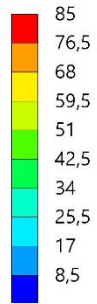
Figure 89: Geomembrane strain energy [mJ] at *t*=10s with a deformation scale factor of 2 for test 2
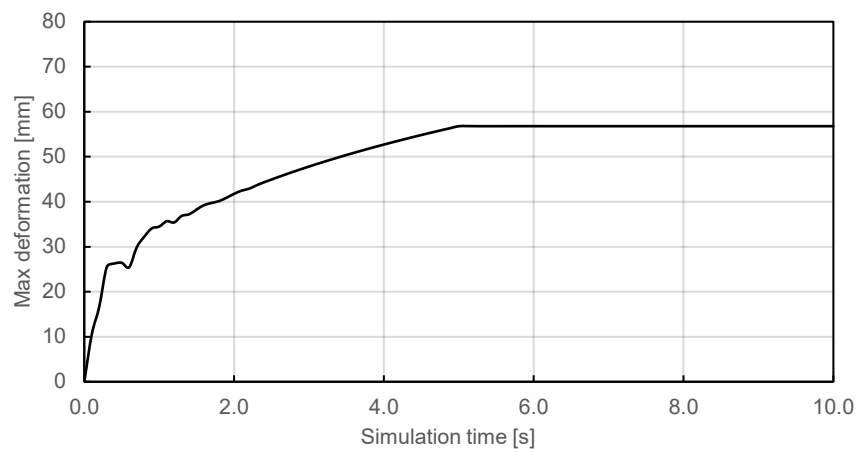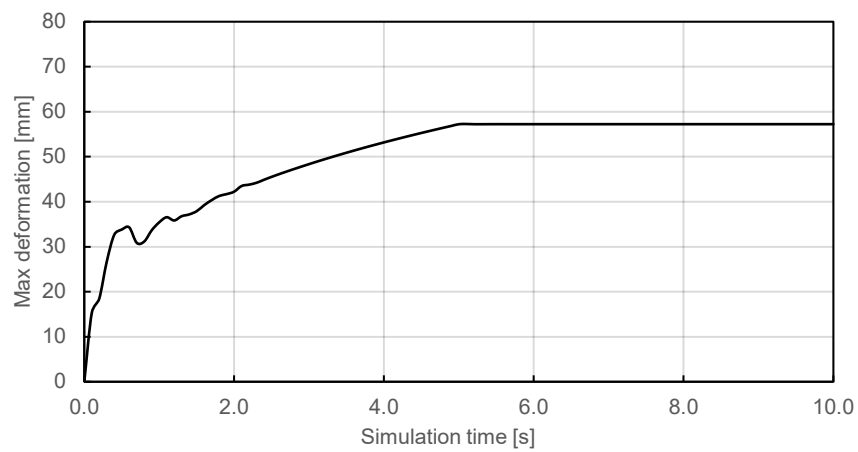
Figure 90: Evolution of the maximum out-of-plane deformation of the geomembrane over time for test 2
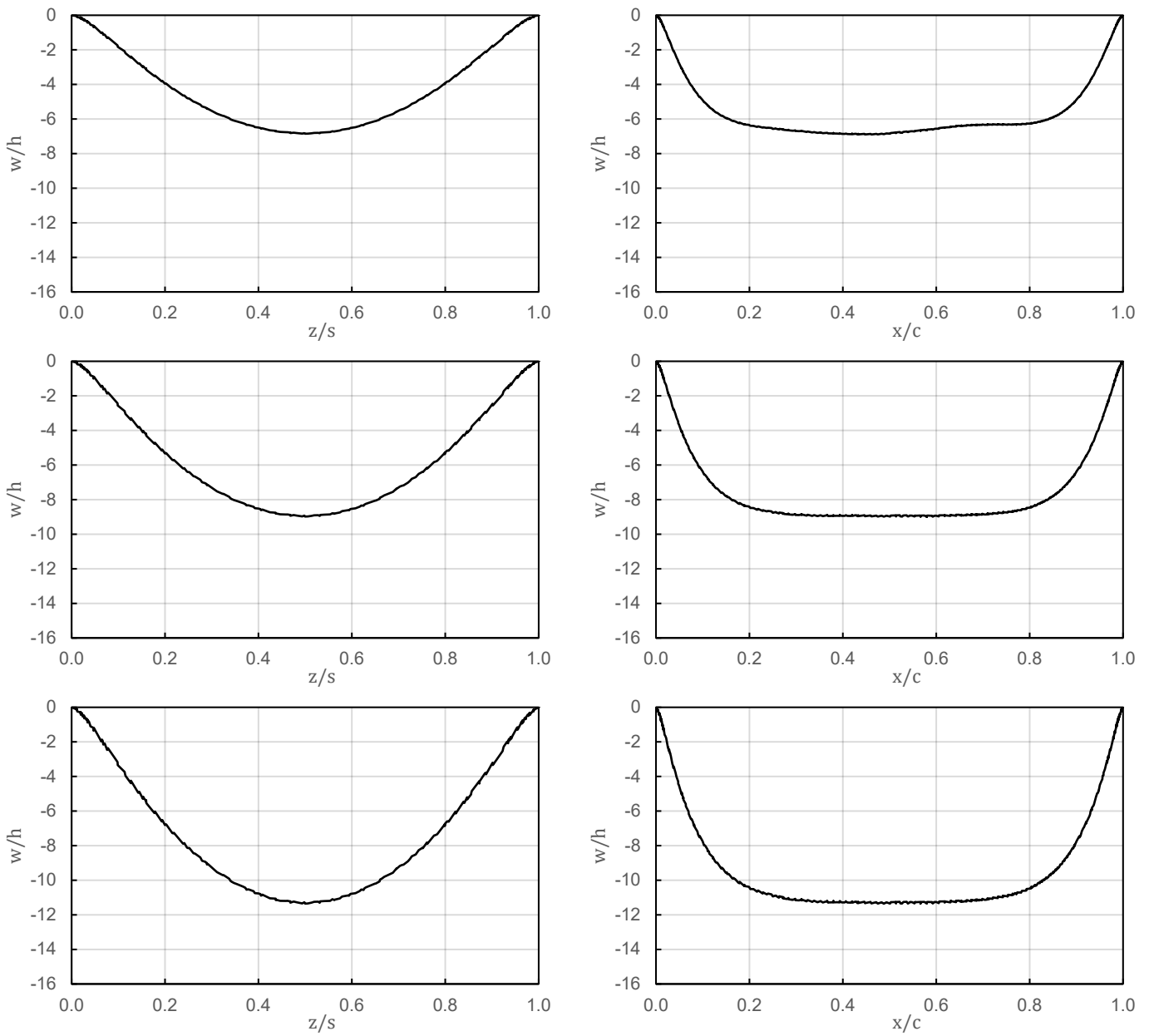
Figure 91: Cross-sections of geomembrane out-of-plane deformation in YZ plane (section cut) for the left column and XY plane (longitudinal cut) for the right column at times t=1s for the first row, t=2.5s for the second row and t=10s for the third row for test 2

XV

Results for test 3

Hydraulic results

Figure 92: Hydrodynamic pressure [Pa] in the XY plane at *t*=10s for test 3
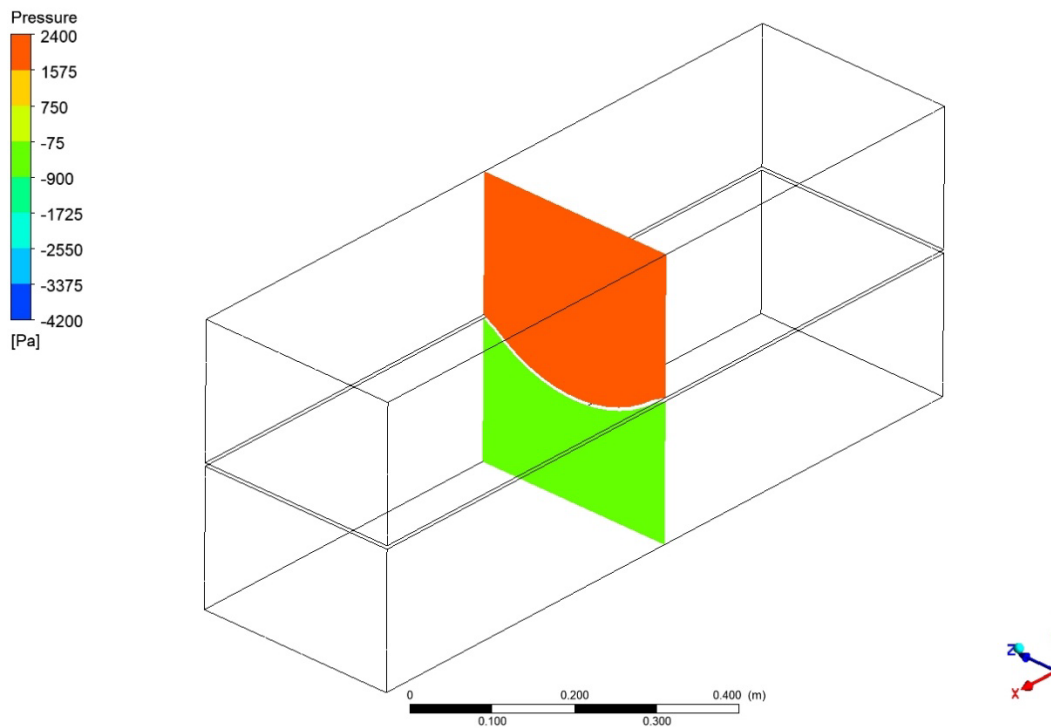
Figure 93: Hydrodynamic pressure [Pa] in the YZ plane at *t*=10s for test 3
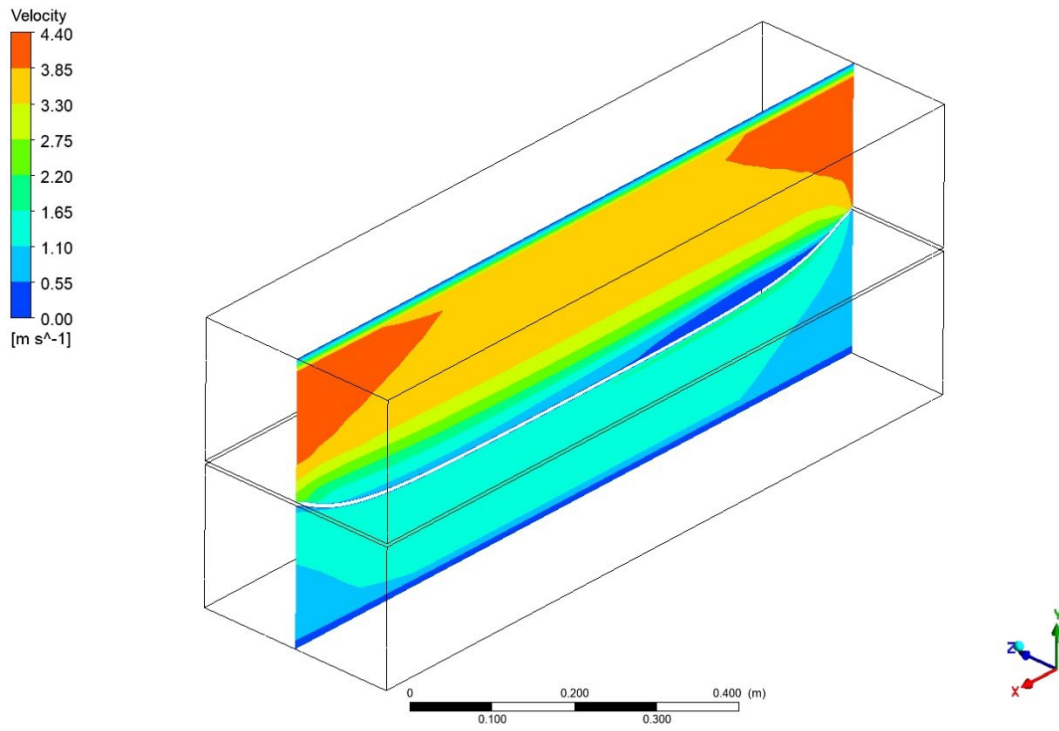
Figure 94: Water velocity [m/s] in the XY plane at *t*=10s for test 3
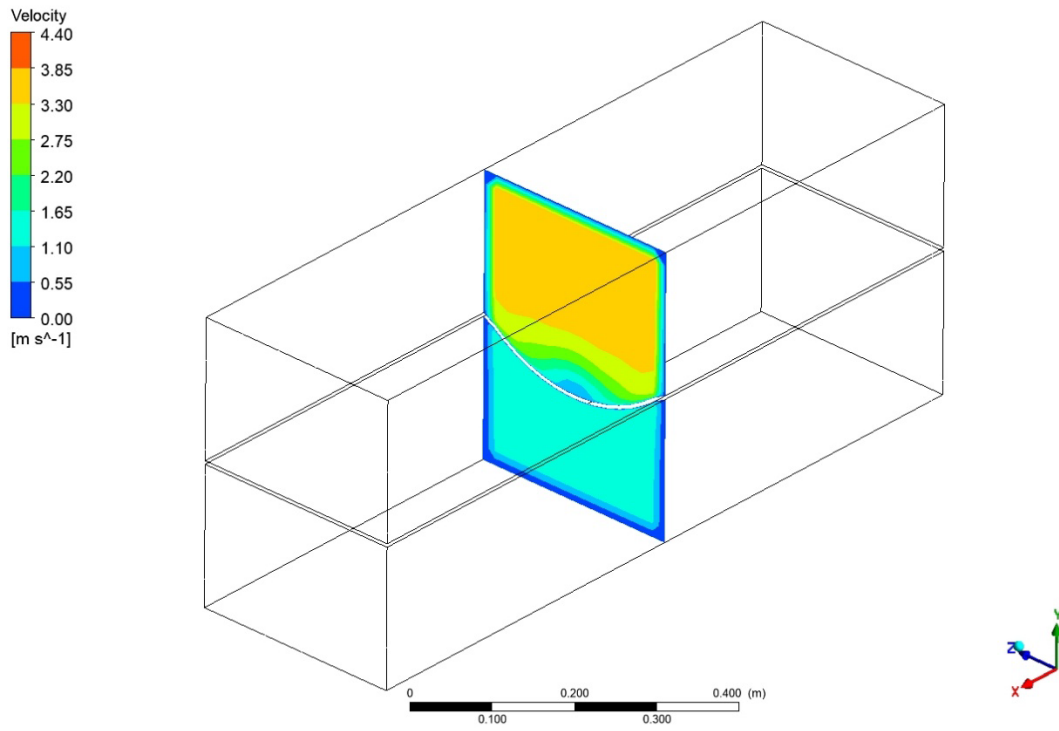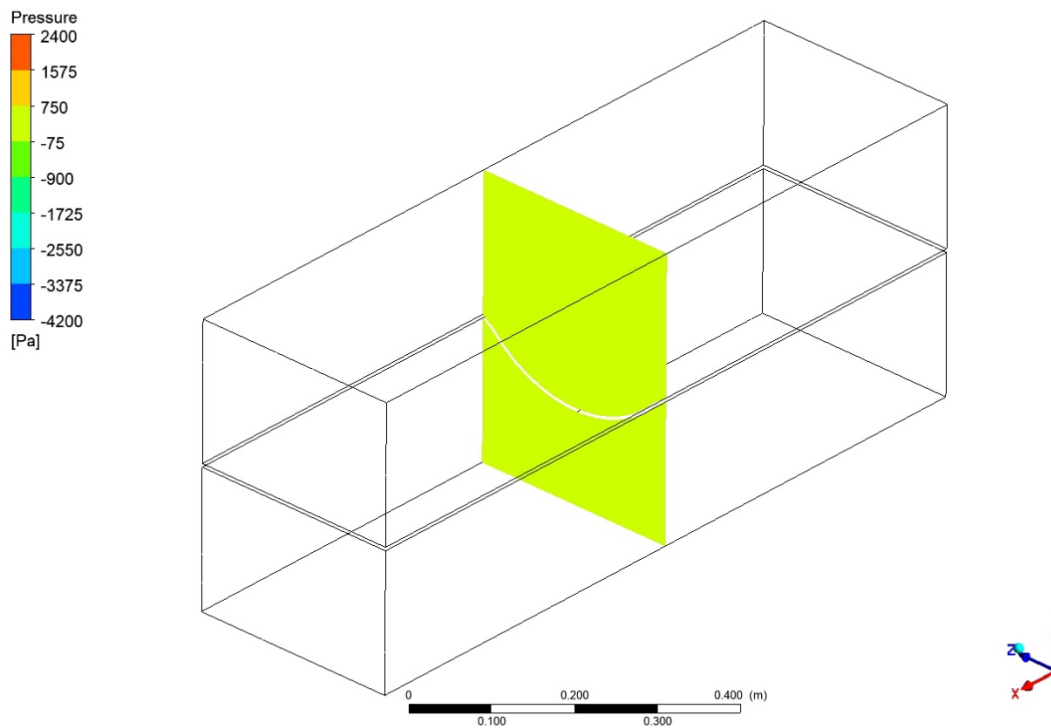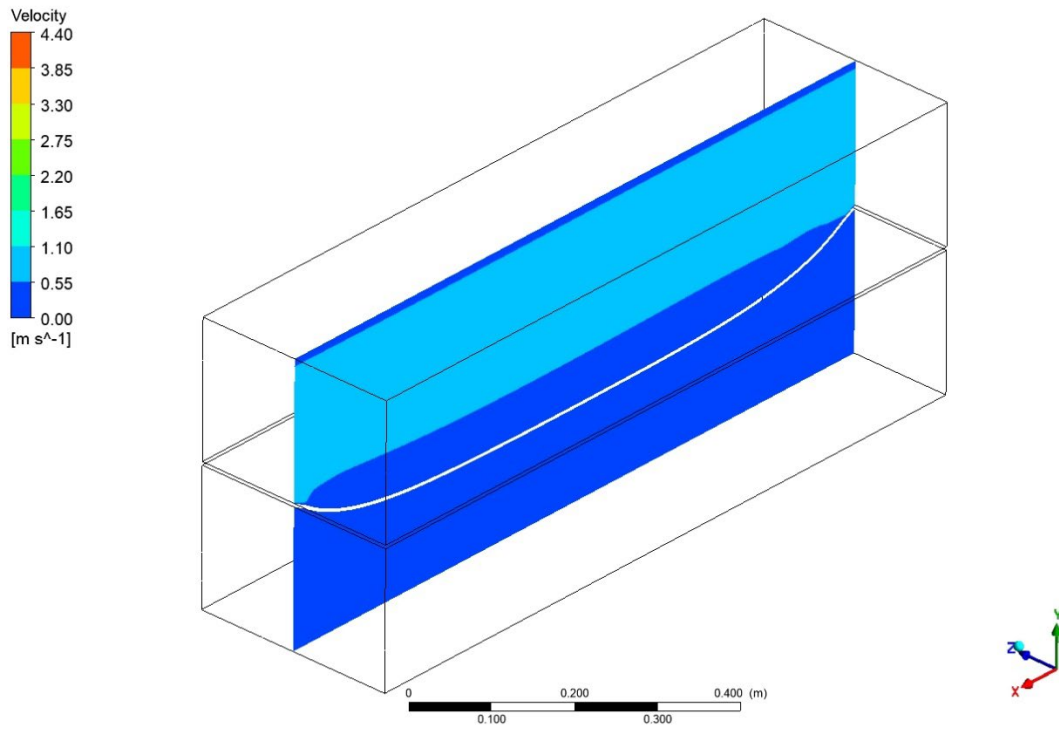

Figure 95: Water velocity [m/s] in the YZ plane at *t*=10s for test 3
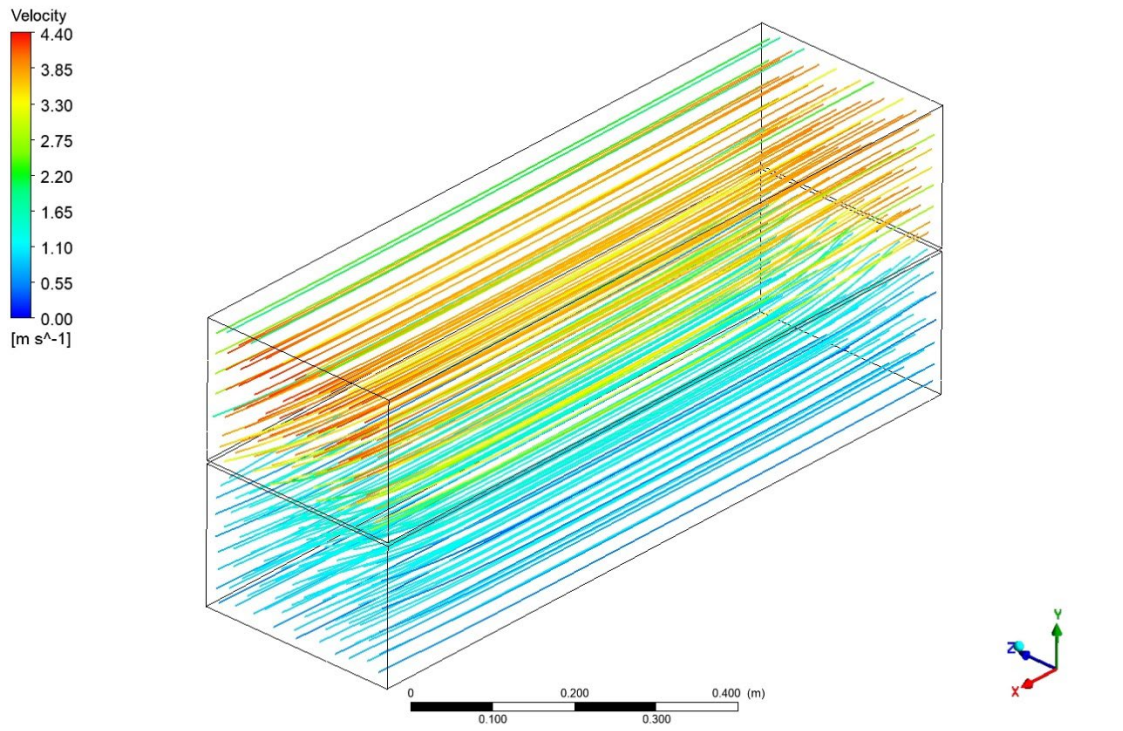
Figure 96: Streamlines [m/s] at *t*=10s for test 3
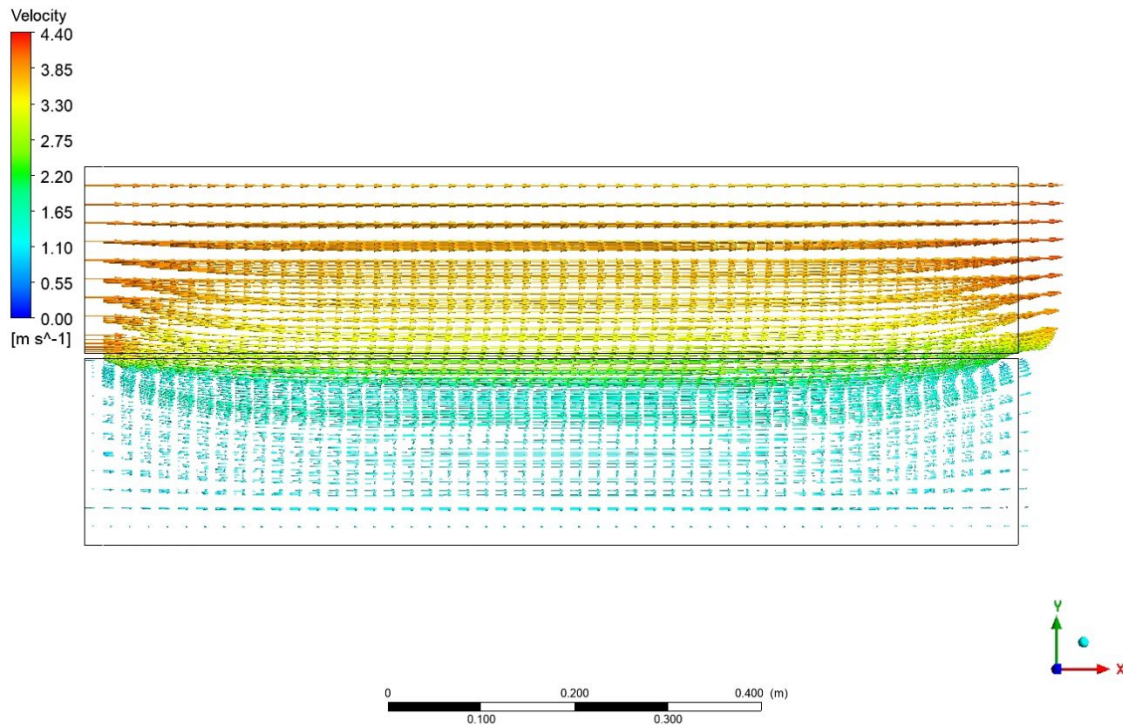
Figure 97: Velocity vectors [m/s] in the XY plane at *t*=10s for test 3

Structural results

C: Transient Structural
Total Deformation
Type: Total Deformation
Unit: mm
Time: 10, s
Max: 57,229
Min: 0
Deformation Scale Factor: 2,

72
64
56
48
40
32
24
16
8
0

0,00   200,00   400,00 (mm)
    100,00   300,00
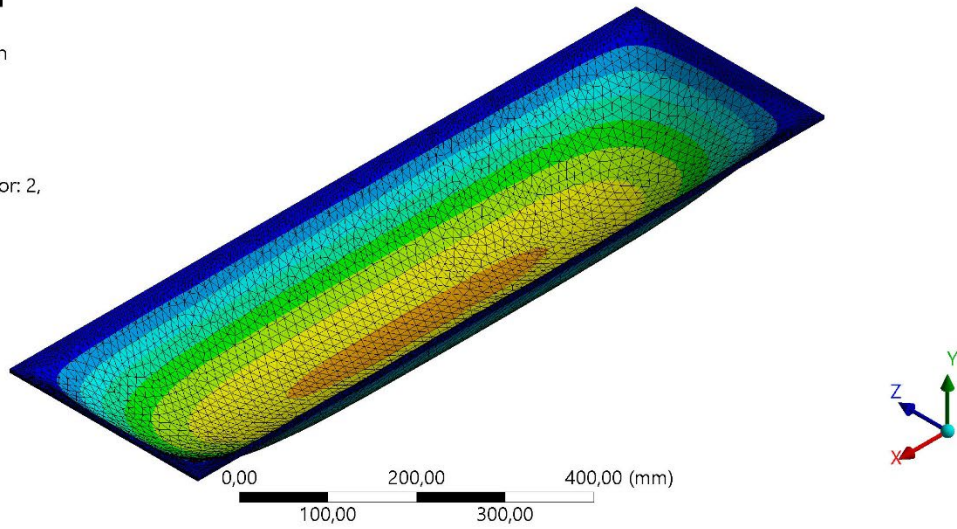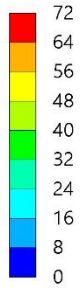
Figure 98: Geomembrane out-of-plane deformations [mm] at *t*=10s with a deformation scale factor of 2 for test 3

C: Transient Structural
Total Deformation
Type: Total Deformation
Unit: mm
Time: 10, s
Max: 57,229
Min: 0
Deformation Scale Factor: 0.0 (Undeformed)

72
64
56
48
40
32
24
16
8
0

0,00   250,00   500,00 (mm)
    125,00   375,00

Figure 99: Plan view of geomembrane out-of-plane deformations at *t*=10s in the undeformed state for test 3

C: Transient Structural
Equivalent Stress
Type: Equivalent (von-Mises) Stress
Unit: MPa
Time: 10, s
Max: 22,839
Min: 0,27894
Deformation Scale Factor: 2,

45
40
35
30
25
20
15
10
5
0

0,00   200,00   400,00 (mm)
    100,00   300,00

Figure 100: Geomembrane stresses [MPa] at *t*=10s with a deformation scale factor of 2 for test 3

C: Transient Structural
Equivalent Elastic Strain
Type: Equivalent Elastic Strain
Unit: mm/mm
Time: 10, s
Max: 0,24608
Min: 0,011179
Deformation Scale Factor: 2,

0,36
0,32
0,28
0,24
0,2
0,16
0,12
0,08
0,04
0

0,00   200,00   400,00 (mm)
    100,00   300,00

Figure 101: Geomembrane strains [-] at *t*=10s with a deformation scale factor of 2 for test 3

C: Transient Structural
Strain Energy
Type: Strain Energy
Unit: mJ
Time: 10, s
Max: 36,759
Min: 0,0032395
Deformation Scale Factor: 2,

85
76,5
68
59,5
51
42,5
34
25,5
17
8,5

0,00   200,00   400,00 (mm)
100,00   300,00

Figure 102: Geomembrane strain energy [mJ] at t=10s with a deformation scale factor of 2 for test 3

Figure 103: Evolution of the maximum out-of-plane deformation of the geomembrane over time for test 3
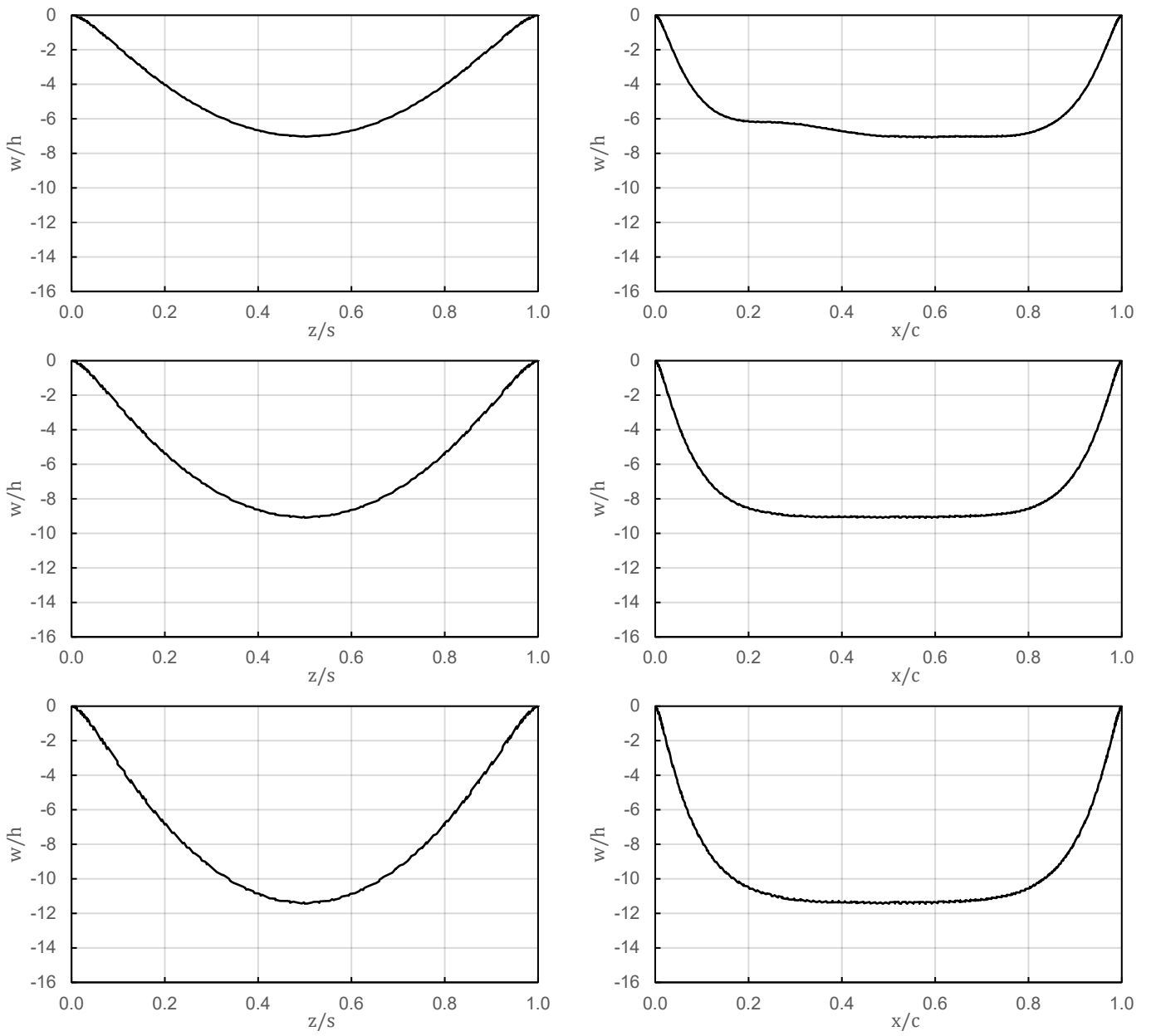
Figure 104: Cross-sections of geomembrane out-of-plane deformation in YZ plane (section cut) for the left column and XY plane (longitudinal cut) for the right column at times *t*=1s for the first row, *t*=2.5s for the second row and *t*=10s for the third row for test 3

Results for test 4

Hydraulic results
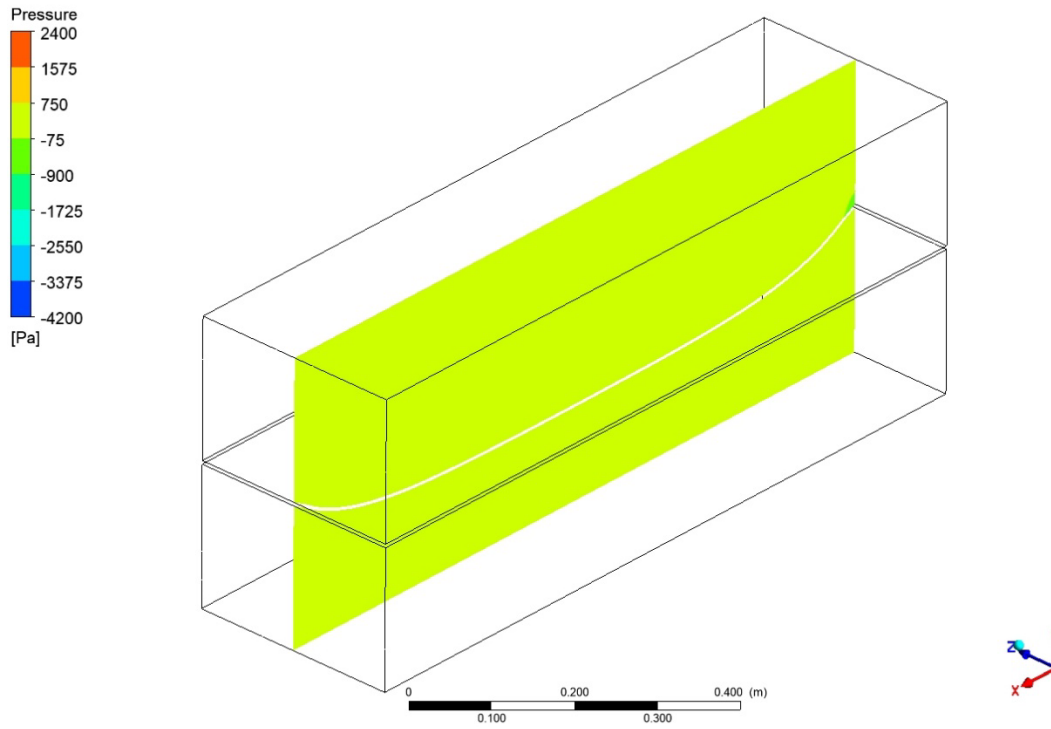
Figure 105: Hydrodynamic pressure [Pa] in the XY plane at *t*=10s for test 4

Figure 106: Hydrodynamic pressure [Pa] in the YZ plane at *t*=10s for test 4

Figure 107: Water velocity [m/s] in the XY plane at *t*=10s for test 4
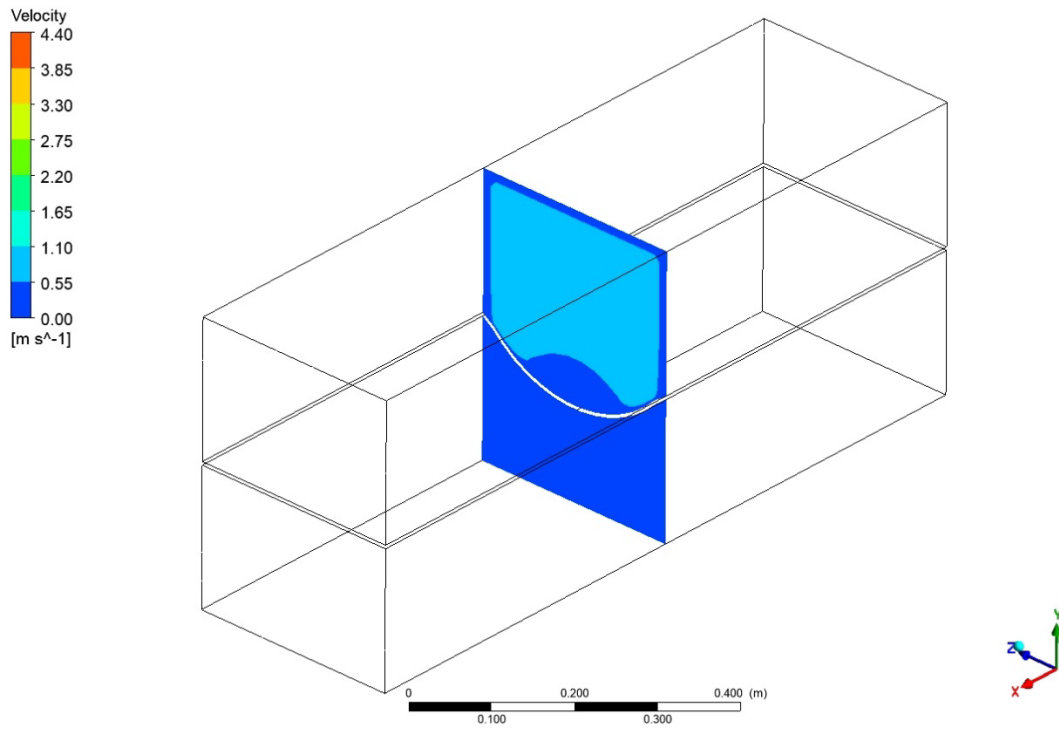
Figure 108: Water velocity [m/s] in the YZ plane at *t*=10s for test 4
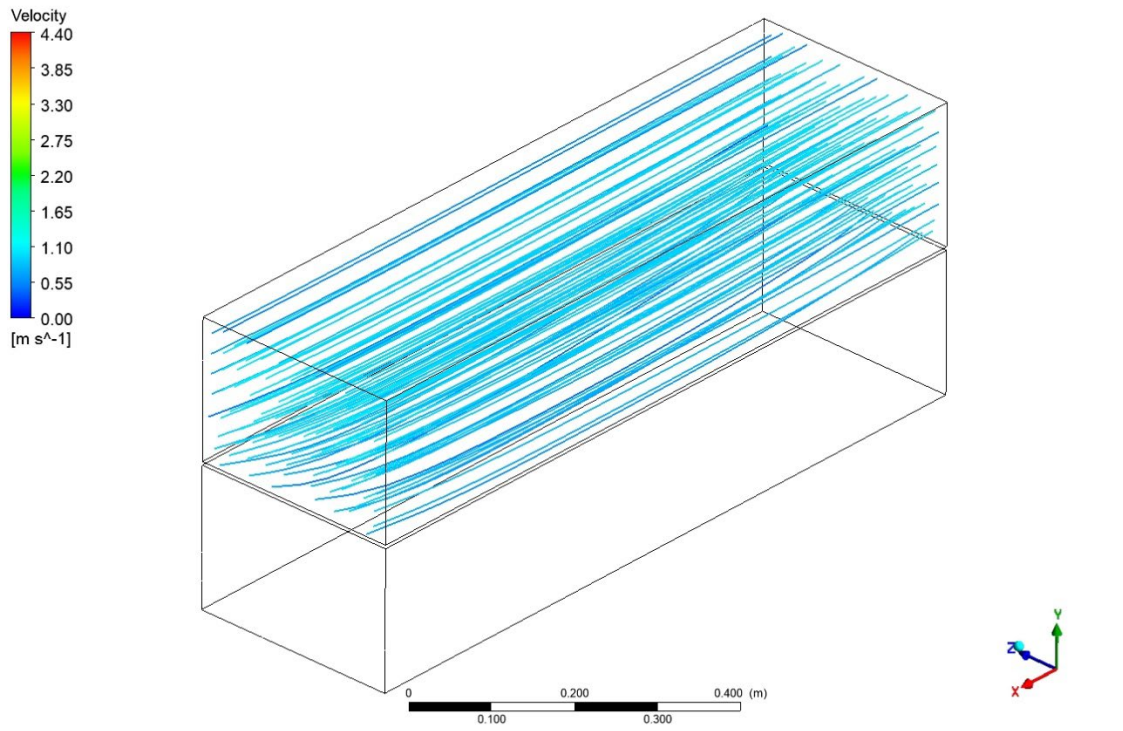
Figure 109: Streamlines [m/s] at *t*=10s for test 4
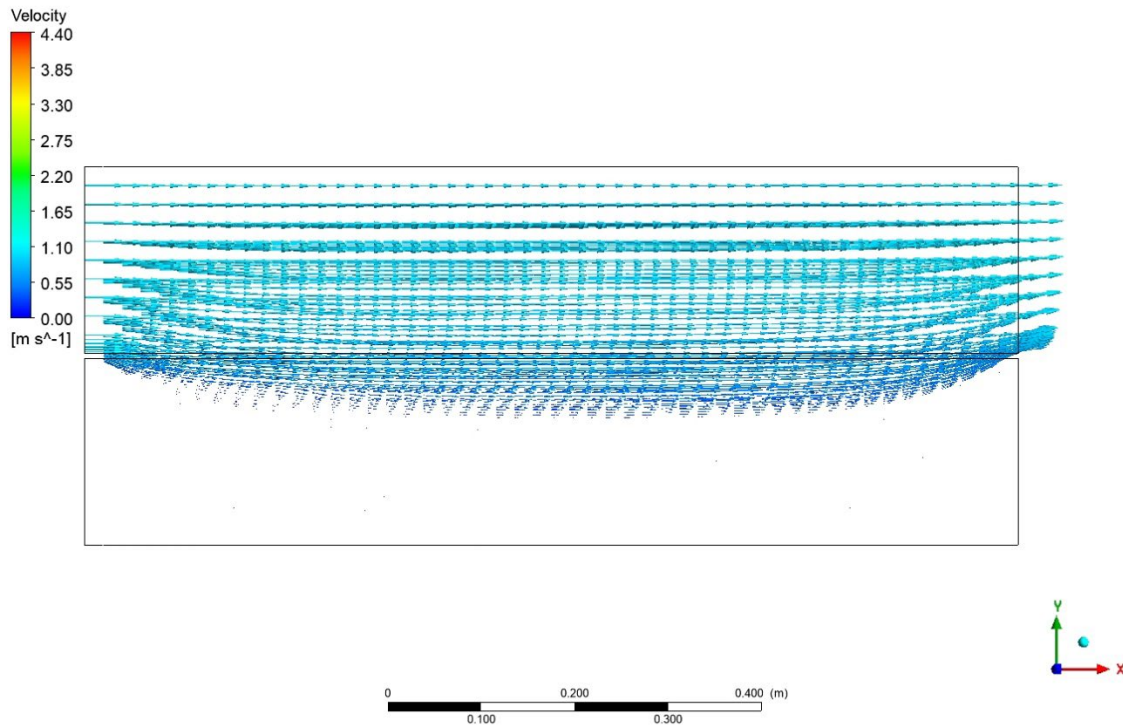
Figure 110: Velocity vectors [m/s] in the XY plane at *t*=10s for test 4

Structural results

C: Transient Structural
Total Deformation
Type: Total Deformation
Unit: mm
Time: 10, s
Max: 71,101
Min: 0
Deformation Scale Factor: 2,

72
64
56
48
40
32
24
16
8
0
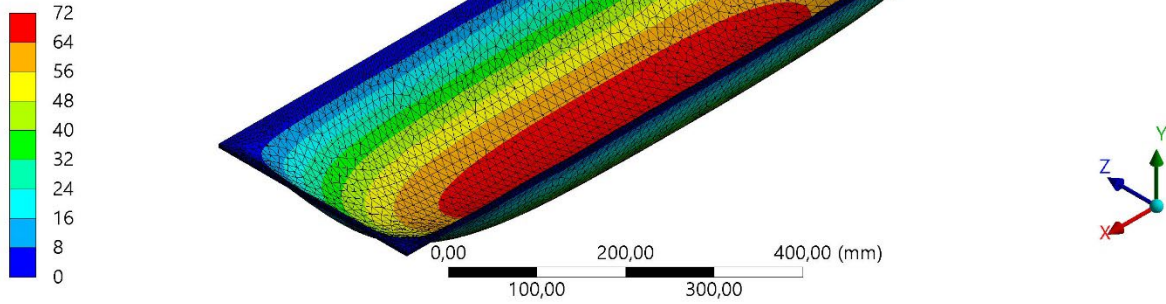
Figure 111: Geomembrane out-of-plane deformations [mm] at *t*=10s with a deformation scale factor of 2 for test 4

C: Transient Structural
Total Deformation
Type: Total Deformation
Unit: mm
Time: 10, s
Max: 71,101
Min: 0
Deformation Scale Factor: 0.0 (Undeformed)

72
64
56
48
40
32
24
16
8
0
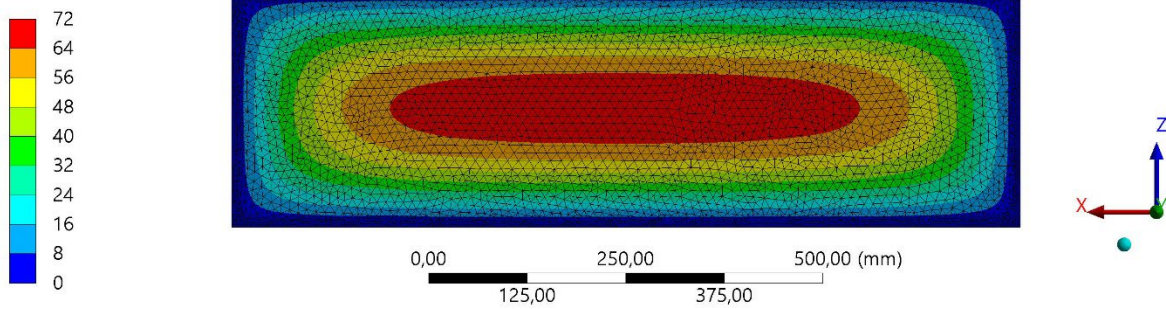
Figure 112: Plan view of geomembrane out-of-plane deformations at *t*=10s in the undeformed state for test 4

C: Transient Structural
Equivalent Stress
Type: Equivalent (von-Mises) Stress
Unit: MPa
Time: 10, s
Max: 44,954
Min: 0,66685
Deformation Scale Factor: 2,

45
40
35
30
25
20
15
10
5
0
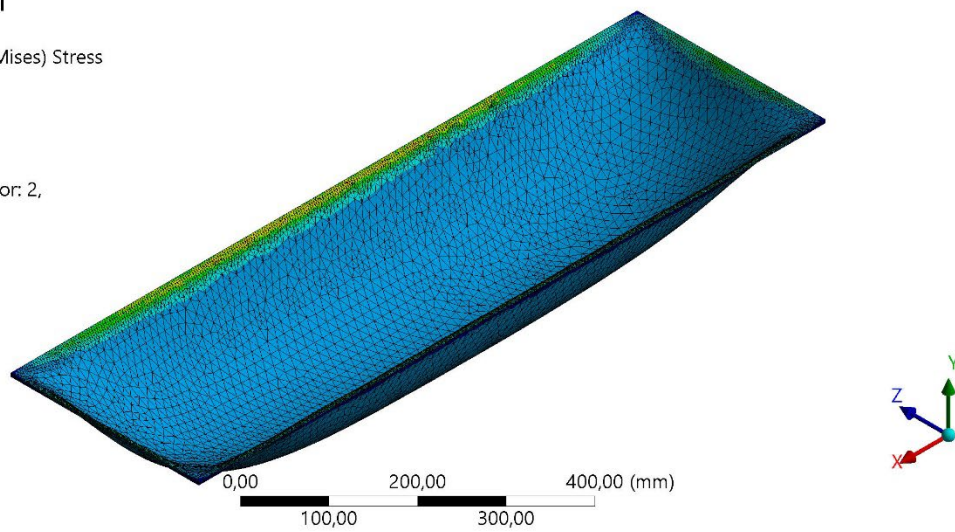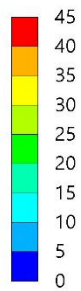
Figure 113: Geomembrane stresses [MPa] at *t*=10s with a deformation scale factor of 2 for test 4

C: Transient Structural
Equivalent Elastic Strain
Type: Equivalent Elastic Strain
Unit: mm/mm
Time: 10, s
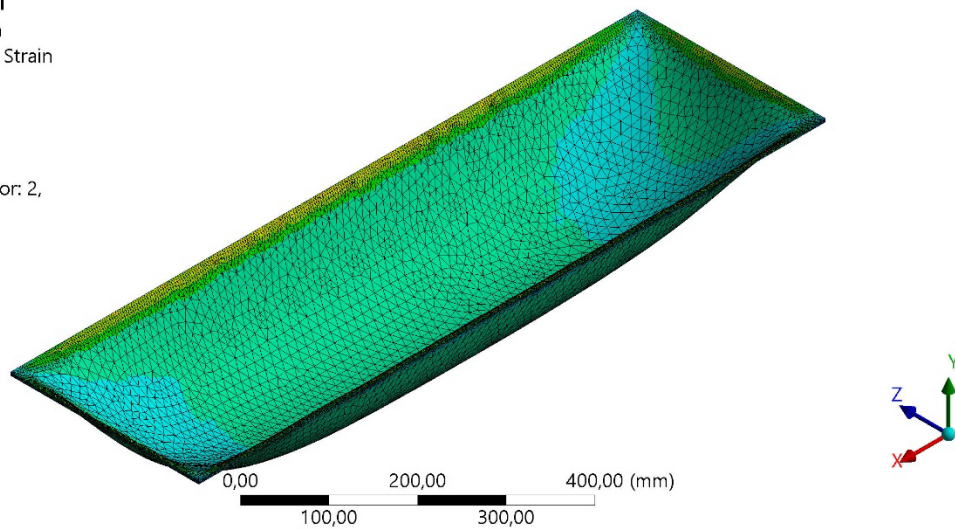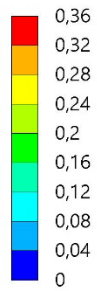Max: 0,3228
Min: 0,022848
Deformation Scale Factor: 2,

0,36
0,32
0,28
0,24
0,2
0,16
0,12
0,08
0,04
0

Figure 114: Geomembrane strains [-] at *t*=10s with a deformation scale factor of 2 for test 4

C: Transient Structural
Strain Energy
Type: Strain Energy
Unit: mJ
Time: 10, s
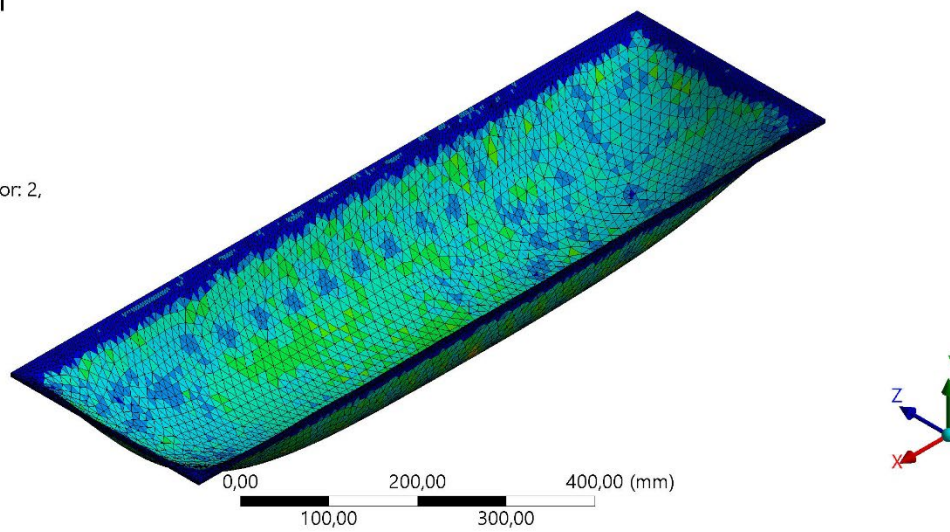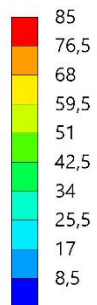Max: 81,809
Min: 0,016077
Deformation Scale Factor: 2,

85
76,5
68
59,5
51
42,5
34
25,5
17
8,5

0,00   200,00   400,00 (mm)
100,00   300,00

Figure 115: Geomembrane strain energy [mJ] at *t*=10s with a deformation scale factor of 2 for test 4
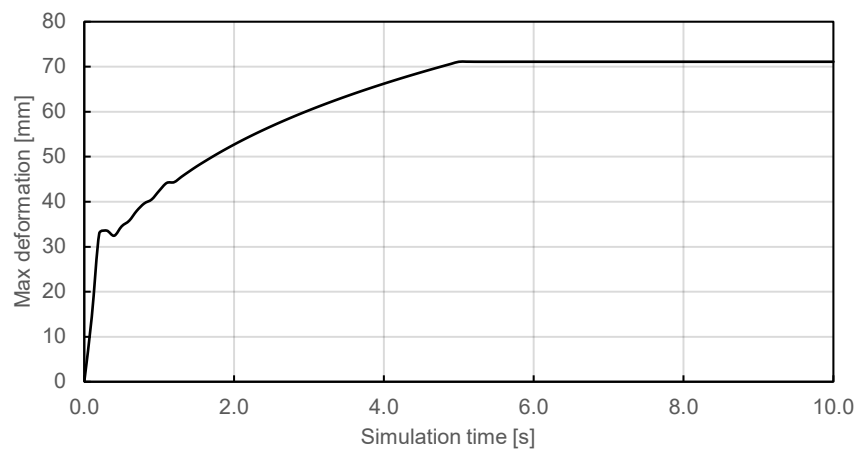

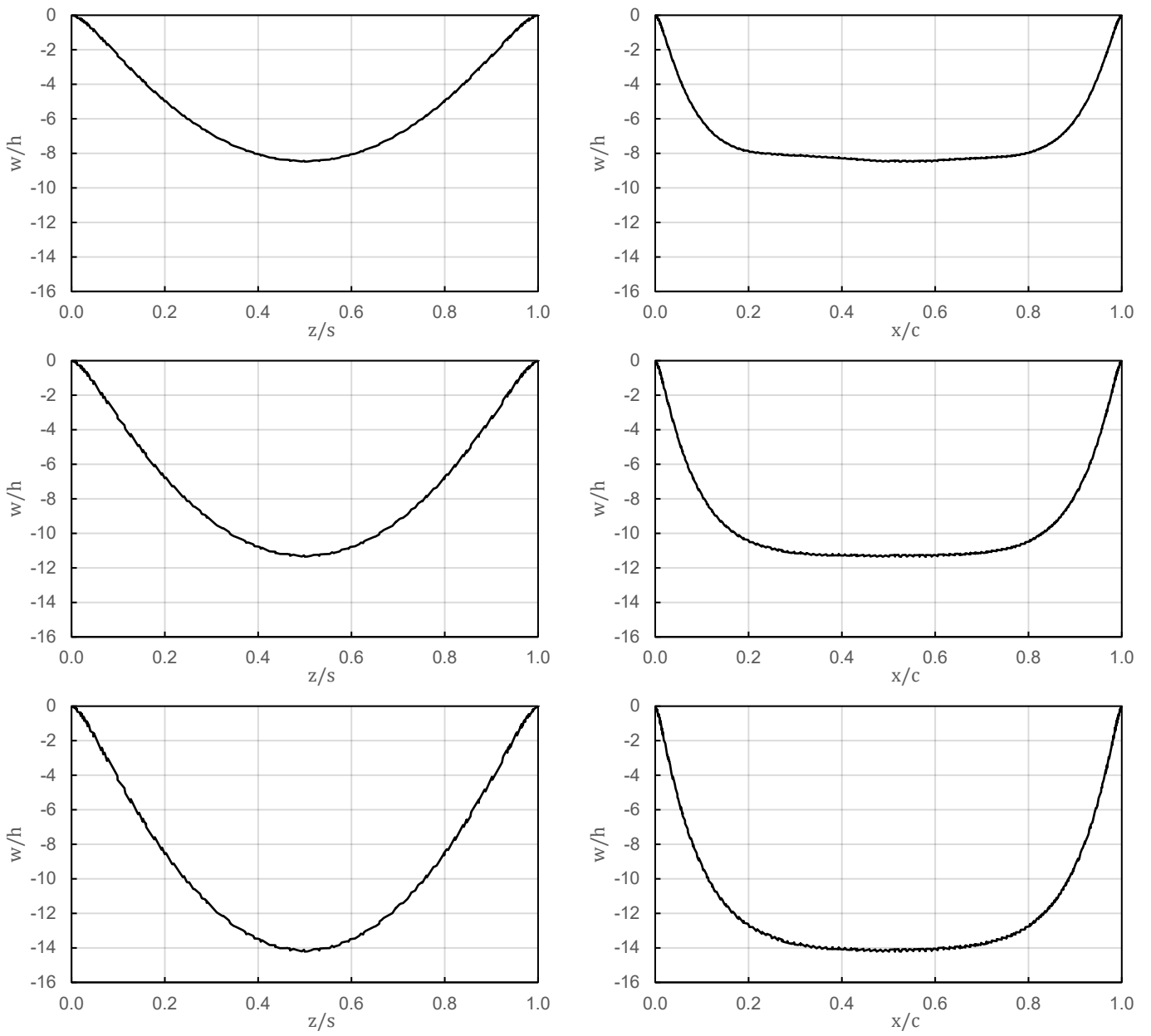Figure 116: Evolution of the maximum out-of-plane deformation of the geomembrane over time for test 4

Figure 117: Cross-sections of geomembrane out-of-plane deformation in YZ plane (section cut) for the left column and XY plane (longitudinal cut) for the right column at times t=1s for the first row, t=2.5s for the second row and t=10s for the third row for test 4